Numerical Simulation of an Ice Age Paleoclimate

By

Fred N. Alyea

Department of Atmospheric Science
Colorado State University
Fort Collins, Colorado

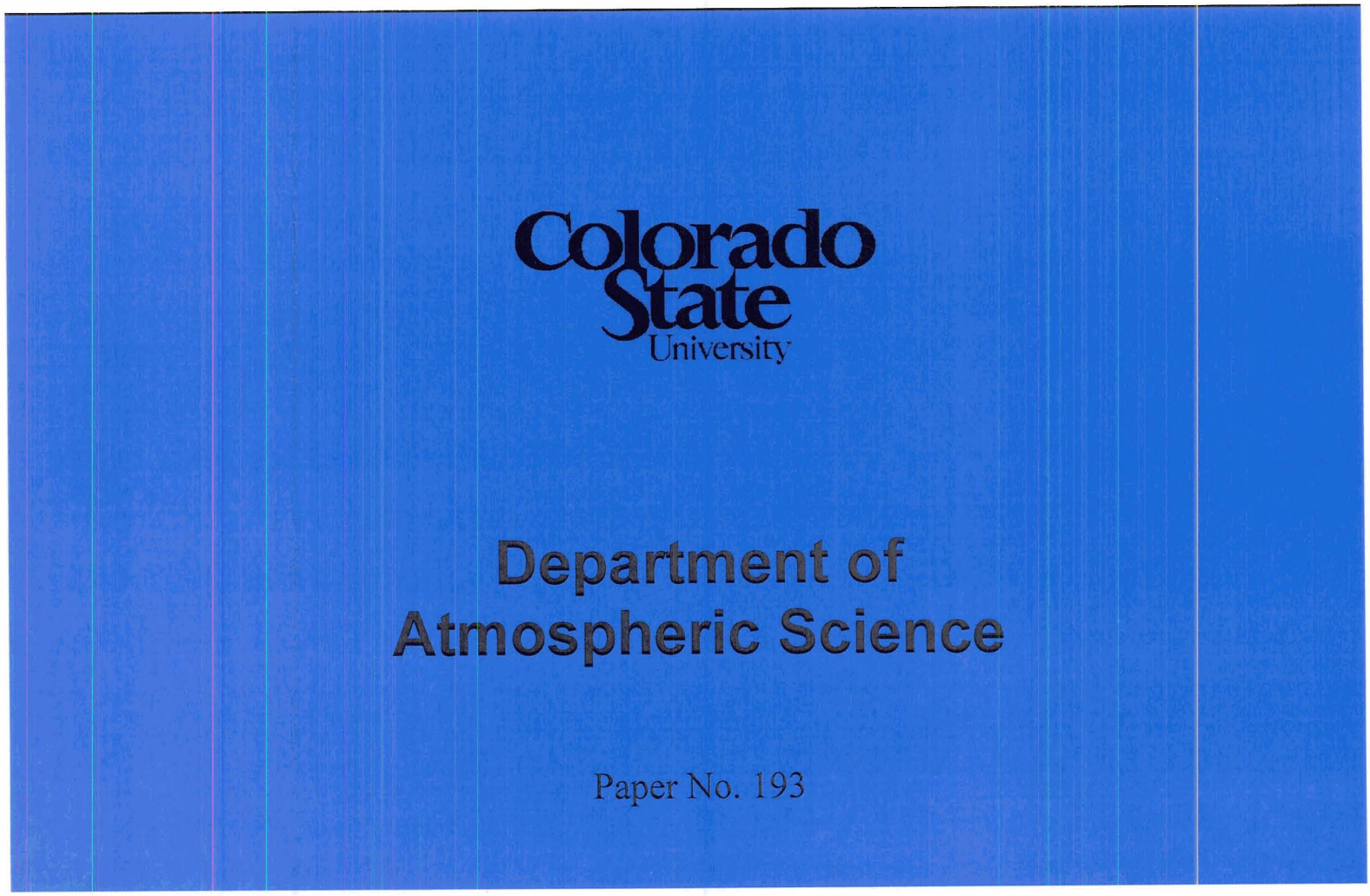

NUMERICAL SIMULATION OF AN ICE AGE PALEOCLIMATE

by

Fred N. Alyea

This study has been supported by the
National Science Foundation under
NSF Grant GA-11637.

Atmospheric Science Paper No. 193

Department of Atmospheric Science
Colorado State University
Fort Collins, Colorado

August 1972

ABSTRACT

NUMERICAL SIMULATION OF AN ICE AGE PALEOCLIMATE

In order to simulate the climate of an ice age, a two-level, quasi-goestrophic, spectral general circulation model for the northern hemisphere is developed. Horizontal diffusion and vertical shearing stresses are incorporated along with a diabatic heating function, including the effects of radiation, horizontal and vertical heat transfer and condensation heating. Orographic influences as well as land-sea-ice distributions of heating are represented at the lower boundary.

The model was integrated forward in time for sixty days under two separate experimental conditions; one representing a present day mean July climate which is used as a bench mark for comparison and the other aimed at simulation of a summer ice age climate with particular emphasis on the last great ice age maximum of the Quaternary period some 18,000 years ago. Forcing and surface boundary conditions for the Quaternary integration were established from a variety of paleogeologic sources.

Results of the statistical climate evaluations of the two model solutions show that the dynamic activity present in the Quaternary calculation was substantially greater than that observed in the corresponding present day integration, although this difference was essentially limited to eddy motions. The climatological manifestations of this observation are presented on a series of isobaric height contour charts which show that over North America during the Quaternary calculation an orographically induced high pressure ridge developed in the area of maximum glaciation centered on Hudson Bay. The center of the circumpolar vortex, therefore, was forced to a position just south of Greenland.

Strong height gradients developed along the edges of the North Atlantic pack ice and, in Europe, a sharp low pressure trough appeared south of the Scandinavian glacier maximum in connection with a blocking high to the east. These features were not present in the climatological results of the present day mean July simulation.

While the Quaternary ice age climatology presented cannot be considered conclusive, some verification of the model results as compared with paleoclimatic observational studies is presented.

Fred N. Alyea
Department of Atmospheric Science
Colorado State University
Fort Collins, Colorado 80521
August, 1972

ACKNOWLEDGEMENTS

This research has been supported by the Atmospheric Sciences Section, National Science Foundation, under Grant GA-11637 to Colorado State University. Some fifty hours of CDC-6600 computer time has been donated by the National Center for Atmospheric Research (NCAR), Boulder, Colorado. The National Center for Atmospheric Research is sponsored by the National Science Foundation.

The author is particularly indebted to Dr. Ferdinand Baer for his patience and guidance throughout the course of this study. Special thanks are extended to Messrs. R. Jenne and D. Joseph of the NCAR staff for providing some of the climatological data used in this study. In addition, the author has benefited greatly from the expertise of his colleagues, Dr. T. J. Simons and Mr. W. R. Burrows.

The expert typing of the manuscript by Mrs. Paula Brant is much appreciated. Messrs. L. Kovacic and J. Gailiun helped with the preparation of the figures.

Finally, a special note of appreciation is extended to my wife, Charlotte, who suffered through the long months involved in the completion of this study.

TABLE OF CONTENTS

LIST OF TABLES

LIST OF FIGURES

List of Figures Continued

List of Figures Continued

I. INTRODUCTION

A. Historical background

Geological evidence of continental glaciation was first discovered more than two hundred years ago. Since that time a great deal of knowledge concerning the physical nature of such glaciations and the multiple recurrences of ice ages has been accumulated. In addition, a multiplicity of theories on the possible causes of the onsets of these ice ages have been introduced although none of these appear to satisfy all of the requirements of an ideal theory. However, little consideration has been given to climatological manifestations of the general circulation of the atmosphere due to the presence of an ice age. This report, therefore, is an attempt to simulate the effects of an ice age and to deduce the resulting climatological atmospheric circulation over the northern hemisphere.

Most previous attempts at establishing paleoclimates have relied heavily upon direct geological observations to deduce surface conditions which imply certain atmospheric features. At best, however, these observations are fragmentary and apply over very limited areas of the globe. One such example is presented by Schwarzbach (1963) in which high and low pressure areas in central Europe during the later part of the Würm Ice Age are reconstructed (Poser, 1948) from the bedding of sand dunes. A far more powerful tool, however, lies in the establishing of surface temperatures from such geological evidence as the past distributions of tundra areas, the limits of tree lines, and the presence of various types of vegetation. Some paleotemperatures for ocean areas

have been obtained using a technique first formulated by Urey (1947) involving the relative abundance of certain oxygen isotopes in the carbonate skeleton deposits of aquatic animals (for a lucid description of this process see Emiliani, 1958 or in more detail Emiliani, 1955). These temperatures are then extrapolated vertically through correlations with similar conditions observed today and thus a thermal wind field is obtained. One of the most comprehensive studies of this type was undertaken by Lamb and Woodroffe (1970) for the last glacial maximum (Wisconsin or Würm III) of about 18,000 years ago.

A more direct paleoclimatic series of calculations using a two dimensional (latitude and the vertical) prediction model for the purpose of testing various ice age theories was presented by MacCracken (1968). Although the main thrust of this study involves the onset of glaciation and hence full glacial surface boundary conditions are not present, a number of climatological trends are observable in the time integrations as they developed over the year and a half prediction periods. The model is limited for the establishment of a general climatology, however, due to its two dimensional nature which omits longitudinal land-sea-ice distributions of heating and topography and gives only cursory treatment to the effects of Rossby-type wave action. The indication is that a three dimensional general circulation model would be more practical for the present study.

The modern era of numerical simulation of the general circulation was initiated by Phillips (1956) in which the gross features of atmospheric flow were developed from an initial state of rest. One of the more important results of this experiment was the demonstration of the computer as an important tool for the solution of large hydrodynamic flow problems. With this development, a few more refined

and detailed models of the general circulation began to appear, notably, those of Smagorinsky (1963), Mintz (1964), and Leith (1965), until today there are a number of very sophisticated calculations currently being run. The main thrust at the present time seems to be directed toward detailed short period weather predictions with a high degree of reliability. This goal, of course, is not the aim of the present study as we seek to establish climatological solutions over long time periods of integration.

Perhaps the most promising method of deducing a climate is the approach formulized by Lorenz (1964) in which the time-dependent equations of atmospheric motion, subject to variable lower boundary surface conditions and solar forcing, are integrated for extended periods of time and then statistical results are compiled from the solutions. With this method, starting with arbitrary initial conditions, transient quantities withing the scales resolvable by the model are free to develop naturally due to the physical instabilities of the system. Thus the important large scale nonlinear interactions and transport effects are included in the climatological solutions. For a particular situation under investigation, then, a climate is allowed to develop according to the surface boundary and solar forcing conditions present along with internal adjustments inherent in the physical equations. While the question of complete climate determinism remains open (Lorenz, 1968), confidence in this procedure for obtaining large scale climatic solutions has increased greatly over the years as more realistic models have been presented (cf., Smagorinsky et al., 1965; Mintz, 1968; Kikuchi, 1969; and Washington and Kasahara, 1970).

B. Outline of the climatological experiments

Because the state of the general circulation during past geologic eras is not well defined, a direct comparison of model results with paleoclimatic flow patterns is not possible. Therefore, the model must first be tested under known conditions using current data to obtain a bench mark for comparison. This means that two separate time integrations will be performed: one under present conditions and the other for the ice age situation chosen. While it is not expected that the model will reproduce more than some of the gross features associated with a particular climate, major emphasis will be placed upon the difference between the two climatic solutions rather than upon their absolute values. This approach has the advantage of neutralizing, at least in part, some of the physical limitations and uncertainties associated with the model under the assumption that these conditions will induce similar (but not necessarily the same) effects upon both solutions.

We have chosen to simulate mean summer (July) climates for both experimental calculations using fixed solar forcing and surface boundary values associated with the time periods in question. A detailed discussion concerning the generation of the particular boundary conditions used in the model experiments is contained in Chapter III. Summer situations were selected because this is the time of the year when the greatest contrast between ice age and present day climates is expected. For the ice age experiment we will confine ourselves to the last great glacial maximum (Wisconsin/Würm) in the Pleistocene stage of the Quaternary period which occurred

about 18,000 years ago. Selection of this time period was based upon the relative abundance of geological data available for the construction of the glacial geography and pelagic temperatures. Further, the orography of nonglaciated land areas during the Quaternary period was much the same as today.

Because of the long time periods involved in the integration of a general circulation model, control over the initial state of the atmosphere is gradually taken over by the forcing and boundary conditions. While it is not certain that the climatology derived from steady state solutions of such a model is completely independent of its initial configuration, we will assume, as is customarily done, that an arbitrary initial state is permissible. One popular approach is to begin with an atmosphere in a state of rest (for example see Mintz, 1968 or Kikuchi, 1969) and continue the calculation until a climatological steady state is obtained. However, in an attempt to shorten the calculation required to reach such a steady state but still preserve a known initial configuration as a basis for observing and comparing diverging tendencies of the solutions as they develop, we have elected to begin our calculations using current mean July data. Thus, the nonlinear exchange properties of the model are immediately active along with a representative mean flow field and temperature distribution and the model can attain a quasi steady state in a relatively short period of time (within fifteen days for the present calculations).

A final note should be taken concerning the duration of the time integrations. Because the model forcing is fixed to strong summer conditions without allowing for seasonal changes it cannot be expected that climatic results obtained from very long time period solutions

would necessarily be representative of actual conditions. Indeed, the possibility exists that a general circulation model (and even the real planetary atmosphere) under the influence of some 60 days of July forcing would eventually attain climatic states somewhat different from the ones under investigation here. While the detection of such a feature, which we will characterize by the term "degenerate solution", must be approached subjectively we will seek to determine its existence by taking note of the behavior of the level of total kinetic energy during the integration periods for the two model runs. The experiments will be terminated at a point where the temporal kinetic energy profiles appear to show unnatural features. An alternate but computationally more difficult and expensive approach would be to allow for seasonal variations in the solar forcing and surface boundary values and integrate through several years. A statistical climate for each season can then be established by combining the results for the same months over the years contained in the calculation, exactly as is done with current observationally derived climate evaluations. However, such a procedure is well beyond the scope of the present study and we have limited our calculations to sixty days keeping in mind that some of the derived data near the end of this time period may not be useful.

II. THE MODEL

A. Introduction

We seek to establish a general circulation model applicable over a wide range of planetary and atmospheric condtions. A number of models which might be suitable for this purpose have been developed in recent years (cf, Smagorinsky et.al., 1965; Kasahara and Washington, 1967; Mintz, 1968) which show that climate simulation using fairly well known atmospheric and boundary conditions from current data can be attained with good reliability. However, it is felt here that many of these models exhibit a degree of sophistication which cannot be wholly justified for our purposes when we consider the dearth of geophysical data available for climate simulation of past geologic ages. Consequently, we have developed a model represented in the "spectral" domain which, while eliminating many of the physical complexities from the general atmospheric equations, still retains the basic large-scale physical processes governing planetary climates.

B. The basic equations

In order to establish an energetically consistent general circulation model we have reduced the differentiated form of the primitive equation system following Lorenz (1960) through utilization of the quasi-geostrophic assumption and reduction of the equation of balance to a form of the geostrophic equation. Hydrostatics are assumed throughout In addition, the model incorporates horizontal diffusion and vertical shearing stresses along with a non-adiabatic heating function including

the effects of radiation, horizontal and vertical heat transfer and condensation heating. At the lower boundary we represent orographic effects as well as a land-sea-ice distribution of heating.

The horizontal wind field ($\mathbb{V}$) is represented in terms of a stream function (ψ) and a velocity potential (χ) such that

$$\mathbb{V} = \mathbb{k} \times \nabla\psi + \nabla\chi \tag{1}$$

where $\mathbb{k}$ is the unit vector in the direction of increasing geopotential (Φ). (Throughout this paper we will assume all horizontal linear differential operators to be in terms of spherical coordinates). In pressure (p) coordinates the vorticity equation is written in the form

$$\frac{\partial \nabla^2\psi}{\partial t} = -J(\psi,\nabla^2\psi + f) - \nabla \cdot f\nabla\chi + F \tag{2}$$

and the divergence equation is simplified to the geostrophic relationship

$$\nabla^2\Phi = \nabla \cdot f\nabla\psi \quad . \tag{3}$$

In (2), F represents the vertical component of the curl of stress and diffusion (to be discussed in more detail later) and J is the Jacobian operator in spherical coordinates (cf, Baer and Alyea, 1971).

The thermal properties of the model are treated through use of the thermodynamic energy equation. In terms of potential temperature (θ) we have

$$\frac{\partial\theta}{\partial t} = -J(\psi, \theta) - \nabla\chi \cdot \nabla\theta - \omega\frac{\partial\theta}{\partial p} + \frac{1}{C_p}\dot{Q}. \tag{4}$$

The term $\frac{1}{C_p}\dot{Q}$ represents the rate of potential temperature change due to all forms of nonadiabatic heating which will be treated with some detail below. ω is the individual pressure change.

In order to insure mass balance in the model and to simplify the prediction equations we introduce the continuity equation in the form

$$\nabla^2 \chi = -\frac{\partial \omega}{\partial p} \quad . \tag{5}$$

It is convenient to define a new variable X (Lorenz, 1960) such that

$$X = -\int_o^p \chi \, dp \tag{6}$$

whereby

$$\chi = -\frac{\partial X}{\partial p} \quad . \tag{7}$$

Introduction of (7) into (5) allows a simplification of mass continuity to

$$\omega = \nabla^2 X \quad . \tag{8}$$

A further reduction of the model equations occurs through application of the operator $\partial/\partial p^\kappa$ to (3) whereby

$$\frac{p}{\kappa p^\kappa} \nabla^2 \frac{\partial \Phi}{\partial p} = \nabla \cdot f \nabla \frac{\partial \psi}{\partial p^\kappa} \quad . \tag{9}$$

The quantity κ is defined as the ratio of the gas constant (R) to the specific heat at constant pressure of dry air, (C_p), given approximately as 0.2857. Introducing hydrostatics

$$\frac{\partial \Phi}{\partial p} = -\frac{1}{\rho} = -\frac{\kappa C_p}{p} \left(\frac{p}{p_{1000}}\right)^\kappa \theta \tag{10}$$

where we have made use of the equation of state

$$p = \rho \kappa C_p T \tag{11}$$

and the definition of potential temperature

$$\theta = \left(\frac{p_{1000}}{p} \right)^{\kappa} T \quad , \tag{12}$$

we can transform (9) into the thermal wind relationship

$$\frac{C_p}{p_{1000}^{\kappa}} \nabla^2 \theta = - \nabla \cdot f \nabla \frac{\partial \psi}{\partial p^{\kappa}} \quad . \tag{13}$$

Further, application of (7) and (8) allows us to eliminate ω and χ and write the prediction equations (2) and (4) in the form

$$\frac{\partial \nabla^2 \psi}{\partial t} = -J(\psi, \nabla^2 \psi + f) + \nabla \cdot f \nabla \frac{\partial X}{\partial p} + F \tag{14}$$

and

$$\frac{\partial \theta}{\partial t} = -J(\psi, \theta) + \nabla \cdot \theta \nabla \frac{\partial X}{\partial p} - \frac{\partial (\theta \nabla^2 X)}{\partial p} + \frac{1}{C_p} \dot{Q}. \tag{15}$$

We note that the system (13) - (15) represents a closed set of equations in variables ψ , X , and θ provided, of course, that the dissipative and nonadiabatic heating functions are completely specified in terms of the model variables and known constants.

C. Vertical structure of the model atmosphere

The model atmosphere is divided into two layers with subscript level designations as shown in Fig. 1. We see that the vorticity and thermodynamic energy equations are applied at levels 1 and 3 while X must be evaluated at levels 0, 2, and 4. In addition, as we shall see later, we must also determine ψ and θ at the lower boundary surface, 4. Applying finite differentiation to all vertical derivatives in (14) and (15), the four prognostic equations can now be written

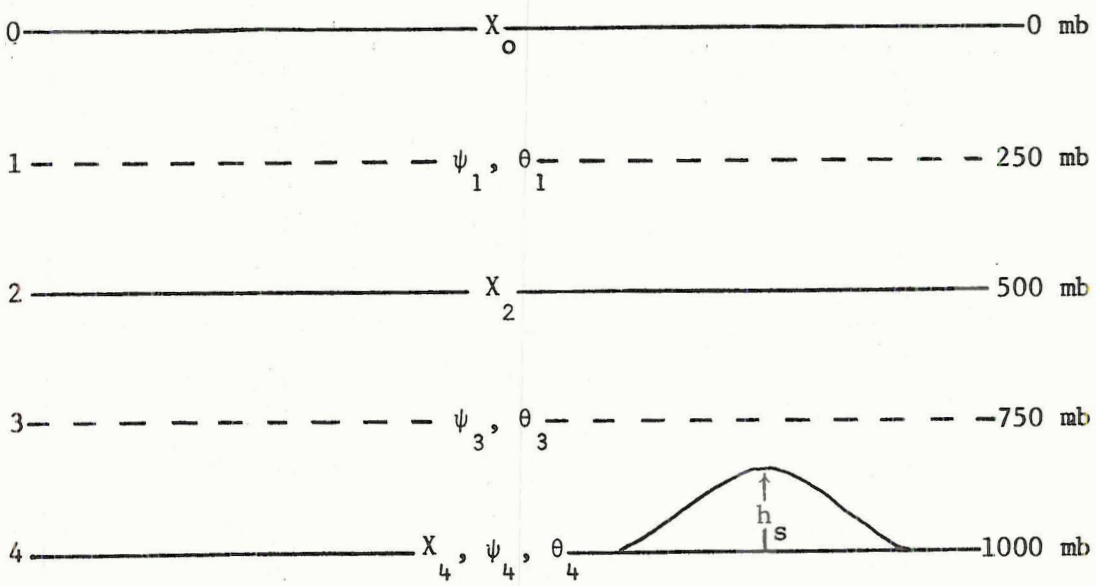

FIGURE 1. Vertical structure of the model atmosphere.

$$\left.\begin{aligned}
\frac{\partial \nabla^2\psi_1}{\partial t} &= -J(\psi_1, \nabla^2\psi_1 + f) - \frac{1}{p_2}\nabla\cdot f\nabla(X_0 - X_2) + F_1 \\
\frac{\partial \nabla^2\psi_3}{\partial t} &= -J(\psi_3, \nabla^2\psi_3 + f) - \frac{1}{p_2}\nabla\cdot f\nabla(X_2 - X_4) + F_3 \\
\frac{\partial \theta_1}{\partial t} &= -J(\psi_1, \theta_1) - \frac{1}{p_2}\nabla\cdot\theta_1\nabla(X_0 - X_2) + \frac{1}{p_2}(\theta_0\nabla^2 X_0 - \\
&\quad - \theta_2\nabla^2 X_2) + \frac{1}{C_p}\dot{Q}_1 \\
\frac{\partial \theta_3}{\partial t} &= -J(\psi_3, \theta_3) - \frac{1}{p_2}\nabla\cdot\theta_3\nabla(X_2 - X_4) + \frac{1}{p_2}(\theta_2\nabla^2 X_2 - \\
&\quad - \theta_4\nabla^2 X_4) + \frac{1}{C_p}\dot{Q}_3
\end{aligned}\right\} . \qquad (16)$$

Similarly, the diagnostic thermal wind relationship (13) becomes

$$C_p B\nabla^2\theta_2 = -\nabla\cdot f\nabla(\psi_1 - \psi_3) \qquad (17)$$

where we define

$$B \equiv \left(\frac{p_1}{p_4}\right)^{\kappa} - \left(\frac{p_3}{p_4}\right)^{\kappa} \quad . \qquad (18)$$

D. Boundary conditions

Because of the necessity to conserve the total mass of the model atmosphere we take as the upper boundary condition

$$X_0 = 0 \quad . \qquad (19)$$

At the lower boundary (1000 mb pressure surface) we will use the approximation

$$\nabla^2 X_4 = \omega_4 \tilde{=} -Ag\rho_s J(\psi_3, h_s) \qquad (20)$$

where we have assumed the surface streamfunction is proportional to ψ_3 such that

$$\psi_4 = A\psi_3 \tag{21}$$

with A being constant (A = 2/3 for our calculations). ρ_s is a constant standard surface density and h_s represents the height of the topography above sea level. For the surface term $\frac{1}{p_2}\theta_4\nabla^2 X_4$ in the fourth equation of (16) we use with the aid of (20)

$$\frac{1}{p_2}\theta_4\nabla^2 X_4 \tilde{=} -A\frac{gp_4}{Rp_2} J(\psi_3, h_s) \tag{22}$$

where we have made use of the equation of state (11) at the 1000 mb level through (12) in the form

$$\theta_4 = T_4 = \frac{p_4}{R\rho_s} \quad . \tag{23}$$

Inserting (19) and (22) in (16) we get the prognostic set

$$\left.\begin{aligned}
\frac{\partial\nabla^2\psi_1}{\partial t} &= -J(\psi_1, \nabla^2\psi_1 + f) + \frac{1}{p_2}\nabla\cdot f\nabla X_2 + F_1 \\
\frac{\partial\nabla^2\psi_3}{\partial t} &= -J(\psi_3, \nabla^2\psi_3 + f) - \frac{1}{p_2}\nabla\cdot f\nabla X_2 + \frac{1}{p_2}\nabla\cdot f\nabla X_4 + F_3 \\
\frac{\partial\theta_1}{\partial t} &= -J(\psi_1, \theta_1) + \frac{1}{p_2}\nabla\cdot\theta_1\nabla X_2 - \frac{1}{p_2}\theta_2\nabla^2 X_2 + \frac{1}{C_p}\dot{Q}_1 \\
\frac{\partial\theta_3}{\partial t} &= -J(\psi_3, \theta_3) - \frac{1}{p_2}\nabla\cdot\theta_3\nabla X_2 + \frac{1}{p_2}\nabla\cdot\theta_3 X_4 + \\
&\quad + \frac{1}{p_2}\theta_2\nabla^2 X_2 + A\frac{gp_4}{Rp_2} J(\psi_3, h_s) + \frac{1}{C_p}\dot{Q}_3
\end{aligned}\right\} \tag{24}$$

E. Vorticity change due to diffusion and stress

We now turn to specification of the forms of the diffusion and stress terms F_1 and F_3. Let us define for any arbitrary level

$$F = \mathbb{k} \cdot \nabla \times [A_{MH} \nabla^2 \mathbb{V} - g \frac{\partial \tau}{\partial p}] \tag{25}$$

where τ represents the shearing stress and A_{MH} is the coefficient of horizontal momentum diffusion. Following the development in spherical coordinates similar to that presented by Baer and Alyea (1971) we find that the horizontal diffusion can be represented by

$$\mathbb{k} \cdot \nabla \times A_{MH} \nabla^2 \mathbb{V} = A_{MH} [\nabla^4 \psi + \frac{2\nabla^2 \psi}{a^2} - \frac{4g\rho}{a} \frac{\partial \nabla^2 \psi}{\partial p} + g^2 \rho^2 \frac{\partial^2 \nabla^2 \psi}{\partial p^2}] \tag{26}$$

where a is the mean radius of the earth. We choose to ignore the last two terms on the right-hand side of (26) since they will be dominated by the shearing stresses.

Turning to consideration of the shearing stresses we shall follow in general the representations as outlined by Phillips (1956) and Charney (1959). We assume that the stress vanishes at the top of the model atmosphere ($\tau_0 = 0$) such that

$$\left.\frac{\partial \tau}{\partial p}\right)_1 = \frac{\tau_2}{p_2} \quad , \quad \left.\frac{\partial \tau}{\partial p}\right)_3 = \frac{\tau_4 - \tau_2}{p_2} \quad . \tag{27}$$

Thus we must evaluate the stress vector (τ) at the mid-level and at the surface. In the free atmosphere the stress is taken proportional to the wind shear whereas the surface stress is represented for simplicity by a linearized form of the square of the wind. These assumptions allow us to write

$$\left.\begin{aligned} \pi_2 &= -\frac{p_2^2}{g} A_{MV} \frac{\partial V}{\partial p}\Big)_2 = \frac{p_2}{g} A_{MV}(V_1 - V_3) \\ \pi_4 &= \frac{p_2}{g} A_{MVS} V_4 = \frac{p_2}{g} A\, A_{MVS} V_3 \end{aligned}\right\} \tag{28}$$

where A_{MV} and A_{MVS} represent coefficients of vertical momentum diffusion in the free atmosphere and at the surface respectively. Values used for A_{MH}, A_{MV}, A_{MVS} along with constant parameters to be described later are tabulated in Appendix A. It should be noted that the coefficient A_{MVS} includes the effect of the mean surface wind speed assumed to be about 10 m s^{-1} at anemometer level. For the surface stress we have also made use of the boundary condition (21) in order to represent the surface wind in terms of the wind field at level 3. Application of conditions (28) to (27) and utilizing (1) which defines the relationship between the wind field and its nondivergent and irrotational components, we find for the contribution to vorticity change due to stress at levels 1 and 3

$$\left.\begin{aligned} -g\mathbf{k} \cdot \nabla \times \frac{\partial \pi}{\partial p}\Big)_1 &= -A_{MV}(\nabla^2\psi_1 - \nabla^2\psi_3) \\ -g\mathbf{k} \cdot \nabla \times \frac{\partial \pi}{\partial p}\Big)_3 &= A_{MV}(\nabla^2\psi_1 - \nabla^2\psi_3) - AA_{MVS}\nabla^2\psi_3 \end{aligned}\right\}. \tag{29}$$

Upon evaluation of the reduced form of (26) at levels 1 and 3 in combination with (29) the final forms of vorticity change due to diffusion and stress can now be written as

$$\left.\begin{aligned} F_1 &= A_{MH}(\nabla^4\psi_1 + \frac{2\nabla^2\psi_1}{a^2}) - A_{MV}(\nabla^2\psi_1 - \nabla^2\psi_3) \\ F_3 &= A_{MH}(\nabla^4\psi_3 + \frac{2\nabla^2\psi_3}{a^2}) + A_{MV}(\nabla^2\psi_1 - \nabla^2\psi_3) - AA_{MVS}\nabla^2\psi_3 \end{aligned}\right\}. \tag{30}$$

F. Diabatic heating of the model atmosphere

For the thermodynamic equations of the prognostic set (24) we will separate the rate of diabatic heating ($\dot{Q}$) into four parts such that

$$\dot{Q} = \dot{Q}^{SW} + \dot{Q}^{LW} + \dot{Q}^{SH} + \dot{Q}^{C} \tag{31}$$

where $\dot{Q}^{SW}$ and $\dot{Q}^{LW}$ represent the rates of heating due to short-wave and long-wave radiation absorption, $\dot{Q}^{SH}$ denotes the heating rate due to sensible heat transferred to the atmosphere from the earth's surface and between atmospheric layers, and $\dot{Q}^{C}$ is that heating rate which can be attributed to condensation processes within the model atmosphere. In the formulation of the various terms in (31) we have attempted to include as wide a range of variability as seems consistent with the climatological situations which might have occurred during the more recent geologic eras. Furthermore, care has been taken to construct the heating functions as far as possible in terms of known model variables rather than relying upon current climatological values which would tend to bias the results toward present day conditions. Thus, for example, the large scale distribution of water vapor, in the absence of a prediction equation for this quantity, is determined diagnostically as a function of the zonal surface termperature distribution and pressure. This is especially important to the long-wave absorption and condensation heating terms which can thus adjust internally the model forcing to allow for a range of climatic possibilities.

Let us first turn to specification of the rate of diabatic heating due to absorption of solar energy, ($\dot{Q}^{SW}$). Over the greater part of the earth we will concern ourselves only with SW absorption in the model

layers centered at levels 1 and 3. However, since we intend to specify surface temperatures over land and ice through an energy flux balance (pelagic temperatures are assumed constant with time and will be completely determined by their initial values) we must also evaluate the solar energy flux absorbed by these surfaces. Because no reliable estimations of atmospheric solar absorption over past geologic ages are available and also because reasonable deviations from currently available data will not materially alter the general climatology of our model over seasonal time periods of integration, we will construct the SW absorption functions from recent estimations.

In general SW radiation data of London (1957) will be used with some adjustments based upon more recent satellite observations. Of prime importance to our calculations is the apparent overestimation by London and other pre-satellite investigators of the earth's planetary albedo, especially in the tropics. A comparison between the planetary albedo for the northern hemisphere in summer (JJA) obtained by Vonder Haar (1968) from all satellites for years 1962 to 1966 and that taken from data by London (1957) is shown in Table 1. Vonder Haar and Hanson (1969) suggest that the fairly large discrepancy between the two sets of values (especially in the tropics) can be attributed to an overestimation by London of the reflectivity of clouds. Accordingly, we have adjusted downward the London data for solar radiation reflected and scattered to space to compensate for the albedo difference. Since it appears that London's estimation of the SW energy absorbed by the atmosphere is approximately correct (Vonder Haar and Hanson, 1969), the excess energy obtained by lowering the cloud albedo will serve to increase the solar energy arriving at the surface. These values are

TABLE 1. Summer (JJA) values used for SW radiation terms. Numbers in parentheses represent extrapolated values.

Degrees North Latitude		0-10	10-20	20-30	30-40	40-50	50-60	60-70	70-80	80-90
Planetary Albedo	London	.35	.34	.31	.31	.37	.41	.44	.53	.54
	Vonder Haar	.23	.23	.24	.25	.30	.35	.39	.46	.50
$\dot{Q}_4^{SW}$ (ly/day)	London	428	469	518	534	458	401	334	284	334
	Adjusted	536	574	588	590	522	465	381	329	368
$\dot{Q}_1^{SW}/\dot{Q}_{TOTAL}^{SW}$	(Davis)	(.260)	(.260)	.256	.250	.247	.255	.267	(.280)	(.295)
$\dot{Q}_3^{SW}/\dot{Q}_{TOTAL}^{SW}$	(Davis)	(.740)	(.740)	.744	.750	.753	.745	.733	(.720)	(.705)
$\dot{Q}_{TOTAL}^{SW}$ (ly/day)	London	163	177	180	179	177	174	187	208	210
$\dot{Q}_1^{SW}$ (ly/day)		42	46	46	45	44	44	50	58	62
$\dot{Q}_3^{SW}$ (ly/day)		121	131	134	134	133	130	137	150	148

shown in Table 1. (It should be noted here that London and Sasamori, 1971, have recently revised the earlier work by London which results in a global planetary albedo somewhat lower than given in the previous study).

In order to estimate the division between the two model layers of the total solar radiative energy absorbed by the atmosphere we will make use of some results of Davis (1963) and apply the computed ratios to London's data. As is shown in Table 1 about twenty five percent of the total absorbed SW energy can be applied to the upper half of the atmosphere. Ratios from Davis's values have been extrapolated to the polar and equatorial regions.

Because we want to determine surface temperatures over land and ice from an energy flux balance at the surface we must specify the SW energy absorbed by these surfaces. For land we will use the relationship

$$F_A^{SW}\Big\}_{land} = (1 - \alpha_s)\, \dot{Q}_4^{SW} \tag{32}$$

where F_A^{SW} represents the SW energy flux absorbed by the underlying surface, $\dot{Q}_4^{SW}$ is the solar energy arriving at the surface and α_s denotes the surface albedo. Data used for the albedos of land and ice can be found in Appendix A. For ice a slight adjustment in the surface absorptivity factor $(1 - \alpha_s)$ is made to account for heat lost at the surface due to evaporation (sublimation). Fletcher (1965) compiled data collected at various Russian and American polar ice drifting stations which indicates that during the summer months about twelve percent of the absorbed SW radiation is lost through evaporation. Accordingly, for ice we let

$$F_A^{SW}\Big]_{ice} = .88(1 - \alpha_s)\, \dot{Q}_4^{SW} \quad . \tag{33}$$

The rate of diabatic heating due to long-wave (LW) radiation and absorption at any level can be given by

$$\dot{Q}^{LW} = g \frac{\partial F_N}{\partial p} \tag{34}$$

where F_N is the net LW flux passing through a level and is defined as the difference between the upward ($F\uparrow$) and downward ($F\downarrow$) directed LW components. That is

$$F_N(p) = F\uparrow(p) - F\downarrow(p) \quad . \tag{35}$$

We have chosen to adopt the method of Sasamori (1968) in which the downward and upward fluxes at level p are given by

$$\left.\begin{aligned} F\downarrow(p) &= \int_o^{T(p)} R\{u(T') - u[T(p)],\, T'\}\, dT' \\ F\uparrow(p) &= \sigma T^4(p_4) + \int_{T(p_4)}^{T(p)} R\{u[T(p)] - u(T'),\, T'\}\, dT' \end{aligned}\right\} \tag{36}$$

where σ is Stefan's constant, R represents a mean absorptivity and u is the effective amount of absorbing gas in a vertical air column of unit cross section. If we let q denote the mixing ratio of the absorbing gas, the effective path length can be written as

$$u = \frac{1}{g} \int_p^{p_4} q \left(\frac{p'}{p_4}\right) dp' \quad . \tag{37}$$

For the purposes of our paleoclimatological model we will consider only two absorbing gasses, carbon dioxide and water vapor. As an approximation the mixing ratio of carbon dioxide (q_c) in the atmosphere will be assumed constant and given by the relation

$$q_c = .480 \text{ (cm)} \frac{g}{p_4} \tag{38}$$

and thus the effective path length for carbon dioxide (u_c) from (37) becomes

$$u_c(p) = .240\left[1 - \left(\frac{p}{p_4}\right)^2\right] \quad . \tag{39}$$

In order to evaluate the effective path length for water (u_w) we will assume that for clear skies the mixing ratio of water vapor is vertically distributed according to

$$q_v(p) = q_4 \left(\frac{p}{p_4}\right)^3 \tag{40}$$

where q_4 represents the mixing ratio at the surface. Using a modification of the integrated Clausius-Clapeyron equation we have devised a climatological relationship for the surface mixing ratio in terms of the zonal mean surface temperature (T_{4Z}) and known constants. That is

$$q_4(T_{4Z}) = .622\, e_o \exp\left[\frac{L_{\ell v}}{R_v}\left(\frac{1}{T_s} - \frac{1}{T_{4Z}}\right)\right] \quad . \tag{41}$$

In (41), e_o is the saturation vapor pressure at the freezing point (6.11 mb), $L_{\ell v}$ and R_v are the latent heat of vaporization (2500 joules g^{-1}) and the gas constant for water vapor (.461 joules g^{-1} K^{-1}) respectively. T_s is an empirical constant equal to 277.31 K. A comparison between surface mixing ratios obtained from (41) and values given by London (1957) for all seasons and latitude belts is shown in Fig. 2a. Fig. 2b depicts some representative values of the vertical distribution of the water vapor mixing ratio computed from (40).

Of course the total LW absorption path length due to water constituents in the atmosphere is additionally effected by the liquid water content in clouds. We will assume that clouds can be accounted

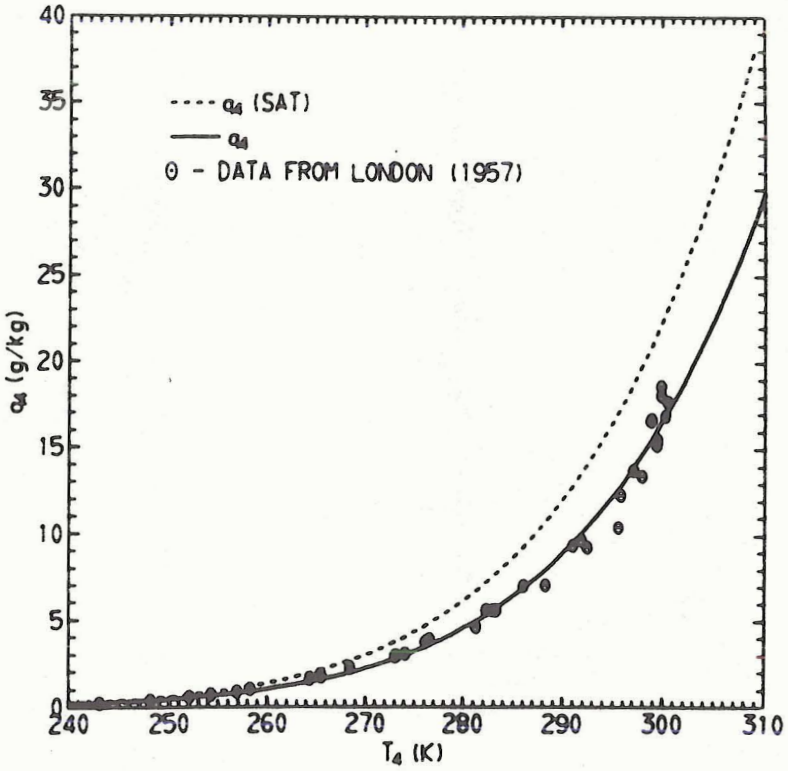

FIGURE 2a. Empirically derived 1000 mb specific humidity as a function of the zonal mean surface temperature. Circles denote values given by London (1957) for all latitude belts and seasons. Saturation values are represented by the dashed curve.

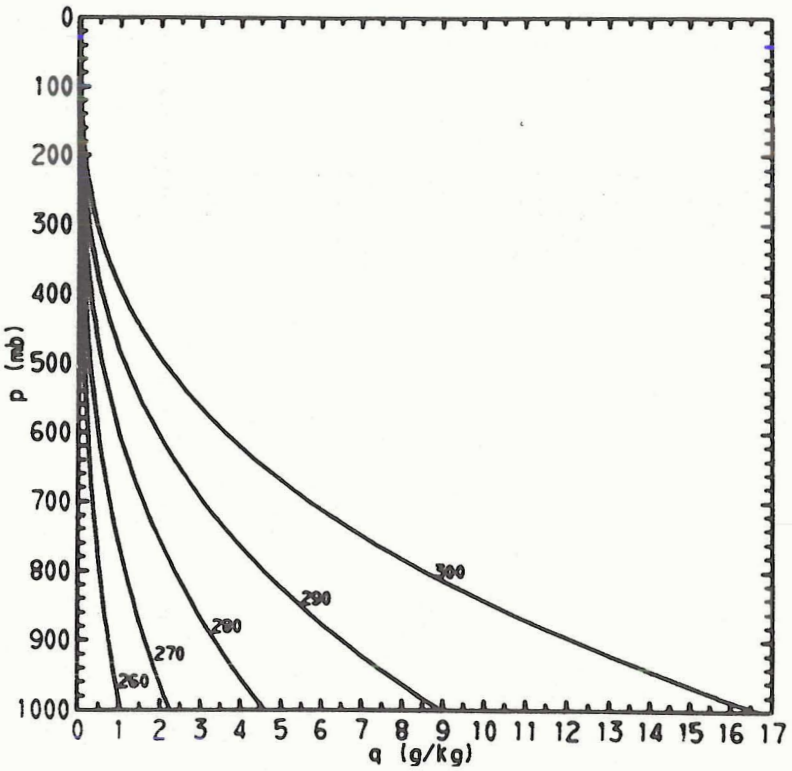

FIGURE 2b. Vertical distributions of specific humidity assumed for a selection of zonal mean surface temperatures (K).

for in a climatological sense by augmenting the water vapor content of the atmosphere. That is, if we let $q_{c\ell}$ represent the mixing ratio of liquid water under conditions of mean cloudiness, we will assert that

$$q_{c\ell}(p) = .2\left(1 - \frac{p}{p_4}\right) q_v(p) \quad . \tag{42}$$

We see that the form of (42) allows for the equivalent cloud distribution in terms of water vapor to be zero at the top and bottom of the atmosphere but attains a maximum value in the lower layer at the 750 mb level. Furthermore, the total water content for clouds in a vertical column of unit cross section is four percent of the total water vapor in the column as given by the vertical integration of (40). At first this would appear to be an accessively large value until we consider that clouds appear essentially as black bodies to LW radiative fluxes. As such, the equivalent water vapor representation for mean cloudiness in (42) is probably on the conservative side. *

Combining (40) and (42) the total mixing ratio due to water constituents (q_w) becomes

$$q_w(p) = q_v(p) + q_{c\ell}(p) = \left(1.2 - .2\,\frac{p}{p_4}\right) q_4 \left(\frac{p}{p_4}\right)^3 \tag{43}$$

and thus from (37)

$$u_w(p) = \frac{q_4 p_4}{30\ g}\left\{6.2 + \left[1 - 7.2\left(\frac{p}{p_4}\right)\right]\left(\frac{p}{p_4}\right)^5\right\} \quad . \tag{44}$$

We can now utilize (39) and (44) to estimate the net downward and upward LW fluxes given by (36) and required by (34) and (35).

* Subsequent analysis of (42) shows that this parameterization of the cloudiness exhibits a negligible effect upon the LW flux fields, contrary to observations.

Applying finite differentiation to (34) at levels 1 and 3 we have for the rates of diabatic heating due to LW radiation and absorption

$$\left.\begin{aligned} \dot{Q}_1^{LW} &= \frac{g}{p_2}\,[F_N(p_2) - F_N(p_0)] \\ \dot{Q}_3^{LW} &= \frac{g}{p_2}\,[F_N(p_4) - F_N(p_2)] \end{aligned}\right\} \tag{45}$$

where we see that we must evaluate net fluxes at levels 0, 2, and 4. The details of these computations can be found in Appendix B where it is shown that in terms of potential temperature

$$\left.\begin{aligned} \dot{Q}_1^{LW} &= A_0^{LW} + A_1^{LW}\theta_1 + A_3^{LW}\theta_3 + A_4^{LW}\theta_4 \\ \dot{Q}_3^{LW} &= B_0^{LW} + B_1^{LW}\theta_1 + B_3^{LW}\theta_3 + B_4^{LW}\theta_4 \end{aligned}\right\} \tag{46}$$

Furthermore, since we will need surface LW radiation flux values for our computation of surface temperatures over land and ice we can write

$$F_N^{LW}(p_4) = F_0^{LW} + F_1^{LW}\theta_1 + F_3^{LW}\theta_3 + (F_4^{LWC} + F_4^{LWW})\theta_4. \tag{47}$$
(land and ice)

All quantities in (46) and (47) are defined in Appendix B.

Let us now consider the rate of diabatic heating due to sensible heat transfer ($\dot{Q}^{SH}$) both vertically and in the horizontal. Using pressure as the vertical coordinate we can write

$$\dot{Q}^{SH} = g\frac{\partial h}{\partial p} + C_p A_{TH}\nabla^2\theta \tag{48}$$

where h is the vertical flux of sensible heat and A_{TH} is the coefficient of horizontal eddy heat diffusion (we assume here that $A_{TH} = A_{MH}$). At the top of our model atmosphere we take

$$h_o = 0 \tag{49}$$

while in the free atmosphere the vertical sensible heat flux becomes

$$h = c_p \left(\frac{\Delta p}{g}\right) A_{TV} \left[\Delta p \left(\frac{\partial \theta}{\partial p}\right) + \Gamma_{CG}\theta\right] \quad . \tag{50}$$

Here the vertical heat diffusion coefficient (A_{TV}) is given the same value as the equivalent momentum diffusion coefficient, A_{MV} . The second term in the brackets of (50) represents a counter-gradient flux which allows for the effect of small scale convective heat transfer under neutral or slightly stable conditions (see Deardorf, 1966). The quantity Γ_{CG} is given by

$$\Gamma_{CG} = \frac{R p_2}{g p} \left(\frac{p}{p_4}\right)^{\kappa} \gamma_{CG} \tag{51}$$

where we will adopt the experimental values for the countergradient γ_{CG} as determined by Washington and Kasahara (1970). They show that a value of 10^{-5} K cm^{-1} in the free atmosphere yields reasonable results while 5×10^{-5} K cm^{-1} is indicated at the surface (γ_{CGS}).

As we shall see below we need evaluate (50) only at the mid-level of our model atmosphere and thus, using finite differentiation in the vertical, we get

$$h_2 = C_p \left(\frac{p_2}{g}\right) A_{TV} \left[\theta_3 - \theta_1 + \Gamma_{CG} \left(\frac{\theta_1 + \theta_3}{2}\right)\right] \tag{52}$$

where we assume (as we will throughout this paper) the potential temperature at level 2 can be given by

$$\theta_2 = \frac{1}{2}\left(\theta_1 + \theta_3\right) \quad . \tag{53}$$

We will estimate the sensible heat flux from the surface by applying (50) in finite difference form through the 750 to 1000 mb layer with the additional constraint that the 750 mb potential temperature for this calculation only is to be reduced to its 1000 mb equivalent (Kasahara and Washington, 1971) using a lapse rate of Γ_{CGS} given by

$$\Gamma_{CGS} = \frac{R}{2g}\,\gamma_{CGS} \quad . \tag{54}$$

Replacing A_{TV} in (50) with the surface vertical heat diffusion coefficient (A_{TVS}) which will be given the same value as A_{MVS} we have at the surface

$$h_4 = C_p\left(\frac{p_2}{2g}\right) A_{TVS}[(1 + \Gamma_{CGS})\theta_4 - (1 - \Gamma_{CGS})\theta_3]. \tag{55}$$

Finally, applying (48) at levels 1 and 3 and utilizing (49), (52) and (55), the diabatic heating terms due to sensible heat transfer become

$$\left.\begin{aligned} \dot{Q}_1^{SH} &= A_1^{SHV}\theta_1 + A_3^{SHV}\theta_3 + A_1^{SHH}\nabla^2\theta_1 \\ \dot{Q}_3^{SH} &= B_1^{SHV}\theta_1 + B_3^{SHV}\theta_3 + B_4^{SHV}\theta_4 + B_3^{SHH}\nabla^2\theta_3 \end{aligned}\right\} \tag{56}$$

where then

$$\left.\begin{aligned} A_1^{SHV} &= C_p A_{TV}\left(\frac{\Gamma_{CG}}{2} - 1\right) \\ A_3^{SHV} &= C_p A_{TV}\left(\frac{\Gamma_{CG}}{2} + 1\right) \\ B_1^{SHV} &= -C_p A_{TV}\left(\frac{\Gamma_{CG}}{2} - 1\right) \\ B_3^{SHV} &= C_p\left[\frac{1}{2}A_{TVS}(\Gamma_{CGS} - 1) - A_{TV}\left(\frac{\Gamma_{CG}}{2} + 1\right)\right] \\ B_4^{SHV} &= \frac{C_p}{2} A_{TVS}\,(\Gamma_{CGS} + 1) \\ A_1^{SHH} &= B_3^{SHH} = C_p A_{TH} \end{aligned}\right\} . \tag{57}$$

For the computation of surface temperatures over land and ice (to be treated below) we will include an estimation of the heat flux due to evaporative cooling by defining a Bowen ratio (B_r) where

$$B_r = \frac{\text{flux of sensible heat}}{\text{latent heat flux}} \quad . \tag{57}$$

Since the Bowen ratio has not been well established on a global scale we will adopt a value of 1 using data presented by Sellers (1965) as a planetary average for land. Thus, taking fluxes as positive toward the surface we have

$$F_S^{SH} = -h_4 \left(1 + \frac{1}{B_r}\right) = F_3^{SH}\theta_3 + F_4^{SH}\theta_4 \tag{59}$$

where then

$$\left.\begin{aligned} F_3^{SH} &= -\left(1 + \frac{1}{B_r}\right) C_p \left(\frac{p_2}{2g}\right) A_{TVS} \left(\Gamma_{CGS} - 1\right) \\ F_4^{SH} &= -\left(1 + \frac{1}{B_r}\right) C_p \left(\frac{p_2}{2g}\right) A_{TVS} \left(\Gamma_{CGS} + 1\right) \end{aligned}\right\} . \tag{60}$$

We turn now to specification of the diabatic heating in the atmosphere through the release of latent heat of condensation ($\dot{Q}^C$). For this purpose we will assume that over climate time scales the atmosphere tends to preserve its moisture distribution. Thus, using the specific humidity as given by (40) and (41) we let

$$\dot{Q}^C = -\varepsilon L_{\ell v} f(\omega) \frac{\partial q_v}{\partial p} \tag{61}$$

where ε is an efficiency factor which we will define as the ratio of specific humidity divided by the saturation value. Thus,

$$\varepsilon = \frac{q_v}{q_{v(SAT)}} = \exp\left[\frac{L_{\ell v}}{R_v}\left(\frac{1}{T_s} - \frac{1}{T_o}\right)\right] \tag{62}$$

where $T_o = 273.16$ K . The function $f(\omega)$ in (61) is chosen so that $\dot{Q}^C$ is zero in areas of sinking motion. That is

$$f(\omega) = \left\{ \begin{array}{l} \omega \text{ for } \omega < 0 \\ \\ 0 \text{ for } \omega \geq 0 \end{array} \right\} \quad . \tag{63}$$

Application of $\partial/\partial p$ to (40) and evaluating (61) at levels 1 and 3 gives

$$\left. \begin{aligned} \dot{Q}_1^C &= -\frac{3}{2} \varepsilon L_{\ell v} q_4 \left(\frac{p_1}{p_4}\right)^2 f(\omega_2) \\ \dot{Q}_3^C &= -\frac{3}{2} \varepsilon L_{\ell v} q_4 \left(\frac{p_3}{p_4}\right)^2 f(\omega_4 + \omega_2) \end{aligned} \right\} \tag{64}$$

where as an approximation we have assumed

$$\left. \begin{aligned} \omega_1 &= \tfrac{1}{2}(\omega_2 + \omega_0) = \tfrac{1}{3}\omega_2 \\ \omega_3 &= \tfrac{1}{2}(\omega_4 + \omega_2) \end{aligned} \right\} \quad . \tag{65}$$

We can now assemble the various components of the total diabatic heating of the model atmosphere. Inserting (46), (56), and (64) into (31) at levels 1 and 3 yields

$$\left. \begin{aligned} \dot{Q}_1 &= L_3\theta_1 + M_3\theta_3 + N_3(\theta_4, X_2) \\ \dot{Q}_3 &= L_4\theta_3 + M_4\theta_1 + N_4(\theta_4, X_2, X_4) \end{aligned} \right\} \tag{66}$$

where we have defined the linear operators and inhomogeneous terms in (66) as

$$\left. \begin{aligned} L_3 &= A_1^{LW} + A_1^{SHV} + A_1^{SHH}\nabla^2 \\ L_4 &= B_3^{LW} + B_3^{SHV} + B_3^{SHH}\nabla^2 \\ M_3 &= A_3^{LW} + A_3^{SHV} \\ M_4 &= B_1^{LW} + B_1^{SHV} \end{aligned} \right\} \quad . \tag{67}$$

$$N_3(\theta_4, X_2) = \dot{Q}_1^{SW} + A_0^{LW} + A_4^{LW}\theta_4 - \frac{3}{2}\varepsilon L_{\ell v} q_4 \left(\frac{p_1}{p_4}\right)^2 f(\nabla^2 X_2)$$

$$N_4(\theta_4, X_2, X_4) = \dot{Q}_3^{SW} + B_0^{LW} + (B_4^{LW} + B_4^{SHV})\theta_4 - \frac{3}{2}\varepsilon L_{\ell v} q_4 \left(\frac{p_3}{p_4}\right)^2 f(\nabla^2 X_4 + \nabla^2 X_2) \qquad (67 \text{ cont.})$$

In definitions (67) we have made use of mass continuity (8) wherever individual pressure velocities are indicated. The functional forms for $f(\nabla^2 X)$ are contained in (63).

G. Convective adjustment

It can be shown that the diabatic heating terms as formulated above can lead to widespread convective instabilities in our model atmosphere. On the time scales of the climatic integrations which we wish to perform such instabilities can indeed reach crippling proportions. Moreover, these conditions are not found in available climatological data and thus it becomes obvious that the atmosphere makes internal adjustments through smaller scale moist and dry convective processes. Unfortunately, the physical mechanisms through which the atmosphere carries out these adjustments (both dynamically and thermodynamically) are not yet clearly understood although vertical heat and momentum transports in protected cores of large cumulonimbi certainly play a major role, especially in the tropics (cf, Riehl and Malkus, 1958 and Gray, 1968). Therefore, we have chosen to use a simple convective adjustment of temperature to simulate the large scale climatological manifestations of these atmospheric adjustments. Similar convective adjustments have been described by Smagorinsky et.al. (1965), Manabe et.al. (1965), Washington and Kasahara (1970) and others.

During the implementation of the convective adjustment process we will constrain the system such that the total internal energy in a vertical column through the atmosphere remains constant. That is

$$C_v \int_{p_4}^{o} T \, dp = \text{constant} \quad . \tag{68}$$

Then, if the the temperature lapse rate exceeds either the dry or moist adiabatic lapse rates we set

$$\left.\begin{aligned} \frac{\partial \theta}{\partial p} &= 0 \text{ for } \omega \geq 0 \\ \text{or} & \\ \frac{\partial \theta_E}{\partial p} &= 0 \text{ for } \omega < 0 \end{aligned}\right\} \tag{69}$$

where θ_E is the equivalent potential temperature given approximately by

$$\theta_E \tilde{=} \theta \exp\left[\frac{L_{\ell v}\, q_{SAT}}{C_p\, T}\right] \quad . \tag{70}$$

This type of adjustment does not alter the total diabatic heating as outlined in the previous section but merely serves to vertically redistribute the heating where large scale convective instability is indicated.

H. Surface temperatures

We assume that oceans exhibit an infinite heat capacity and therefore pelagic surface temperatures are fixed for all time integrations to their initial values. For land and ice, however, the heat capacity is assumed to be negligibly small allowing the surface temperature distribution to be determined through a heat flux balance. This can be given as

$$F_A^{SW} - F_N^{LW}(p_4) + F_S^{SH} = 0 \tag{71}$$

where all fluxes are taken as positive when directed toward the surface from the atmosphere. Inserting results from (47) and (59) into (71) and rearranging we get for the surface flux balance on land and ice

$$\left.\begin{aligned} &(F_4^{SH} - F_4^{LWC} - F_4^{LWW})\theta_4 = F_0^{LW} - F_A^{SW} + F_1^{LW}\theta_1 + (F_3^{LW} - F_3^{SH})\theta_3 \\ &\text{(land and ice)} \\ &\text{and} \\ &\theta_4 = \text{constant} \quad \text{(over oceans)} \end{aligned}\right\} \tag{72}$$

I. Final form of the model equations

In order to remove the coriolis force (f) from the nonlinear Jacobians in (24) we will make use of the form $f = 2\Omega\mu$ with μ being the sine of latitude and Ω the earth's rotation rate. Letting λ represent longitude and a the earth's mean radius we then have, for example

$$J(\psi, f) = \frac{2\Omega}{a^2} \frac{\partial \psi}{\partial \lambda} \tag{73}$$

which is seen to be linear in ψ. Application of (73) to (24) at levels 1 and 3 together with (30) and (66) provides us with the detailed form of our model equations. In addition, if we nondimensionalize all quantities in the equations (for details of the nondimensionalization procedure see Appendix C) we arrive at the nondimensional prediction equations

$$
\left.
\begin{aligned}
&\frac{\partial \nabla^2 \psi_1}{\partial t} - L_1\psi_1 - M_1\psi_3 = -J(\psi_1, \nabla^2\psi_1) + 2\nabla \cdot \mu\nabla X_2 \\
&\frac{\partial \nabla^2 \psi_3}{\partial t} - L_2\psi_3 - M_2\psi_1 = -J(\psi_3, \nabla^2\psi_3) - 2\nabla \cdot \mu\nabla X_2 + \\
&\qquad\qquad + 2\nabla \cdot \mu\nabla X_4 \\
&\frac{\partial \theta_1}{\partial t} - L_3\theta_1 - M_3\theta_3 = -J(\psi_1, \theta_1) + \nabla \cdot \theta_1\nabla X_2 - \\
&\qquad\qquad - \theta_2\nabla^2 X_2 + N_3(\theta_4, X_4) \\
&\frac{\partial \theta_3}{\partial t} - L_4\theta_3 - M_4\theta_1 = -J(\psi_3, \theta_3) - \nabla \cdot \theta_3\nabla X_2 + \nabla \cdot \theta_3\nabla X_4 + \\
&\qquad\qquad + \theta_2\nabla^2 X_2 + A_s J(\psi_3, h_s) + N_4(\theta_4, X_2, X_4)
\end{aligned}
\right\} \quad (74)
$$

in which for clarity we assume all quantities are now nondimensional. This applies equally to all further relationships below. In (74) we have defined the linear operators L_1, L_2, M_1 and M_2 as the nondimensional forms

$$
\left.
\begin{aligned}
L_1 &= -2\frac{\partial}{\partial\lambda} + A_{MH}\left(\nabla^4 + \frac{2}{a^2}\nabla^2\right) - A_{MV}\nabla^2 \\
L_2 &= -2\frac{\partial}{\partial\lambda} + A_{MH}\left(\nabla^4 + \frac{2}{a^2}\nabla^2\right) - A_{MV}\nabla^2 - A\,A_{MVS}\nabla^2 \\
M_1 &= M_2 = A_{MV}\nabla^2
\end{aligned}
\right\} \quad .(75)
$$

All other quantities in (74) have been previously defined. Thus (74) along with the nondimensional forms of (17), (20) and (72) represent the closed system for solution. For completeness we will reproduce these diagnostic relationships in nondimensional form as

$$
\left.
\begin{aligned}
& B\nabla^2\theta_2 = -2\nabla \cdot \mu\nabla(\psi_1 - \psi_3) \\
& \nabla^2 X_4 = -B_s J(\psi_3, h_s) \\
& (F_4^{SH} - F_4^{LWC} - F_4^{LWW})\theta_4 = F_0^{LW} - F_A^{SW} + F_1^{LW}\theta_1 + (F_3^{LW} - F_3^{SH})\theta_3 \\
& \text{(land and ice)} \\
& \theta_4 = \text{constant (oceans)}
\end{aligned}
\right\} \quad (76)
$$

The nondimensional factor B_s is defined in Appendix C.

J. Spectral form of the equations

The literature is now replete with examples of solutions of meteorological problems in the spectral domain too numerous to cite here. We have selected this mathematical technique primarily because of the increased accuracy of solution expected for a given number of horizontal degrees of freedom (Orszag, 1970) and because of the ease with which undesirable high frequency components can be filtered through truncation of the system (Baer and Alyea, 1971). In addition the spectral equations have been shown to conserve integral properties in truncated, non-forced systems and elimate aliasing effects (for examples, see Baer, 1964; Robert, 1966; or Merilees, 1968).

For the expansion of the model equations in spectral form we will follow the development as discussed, for example, by Platzman (1960). Since it is not the purpose of this paper to enter into a lengthy discussion on the application of the spectral technique, the reader is referred to Platzman's work for details.

We define the model variables in terms of a series of spherical harmonics with time dependent coefficients as

$$
\left.
\begin{aligned}
\psi_1 &= \sum_\gamma \psi_\gamma(t) Y_\gamma(\lambda, \mu) \\
\psi_3 &= \sum_\gamma \Psi_\gamma(t) Y_\gamma(\lambda, \mu) \\
\theta_1 &= \sum_\gamma \theta_\gamma(t) Y_\gamma(\lambda, \mu) \\
\theta_2 &= \frac{1}{2}(\theta_1 + \theta_3) = \sum_\gamma \overline{\theta}_\gamma(t) Y_\gamma(\lambda, \mu) \\
\theta_3 &= \sum_\gamma \Theta_\gamma(t) Y_\gamma(\lambda, \mu) \\
\theta_4 &= \sum_\gamma T_\gamma(t) Y_\gamma(\lambda, \mu) \\
X_2 &= \sum_\gamma X_\gamma(t) Y_\gamma(\lambda, \mu) \\
X_4 &= \sum_\gamma \chi_\gamma(t) Y_\gamma(\lambda, \mu) \\
h_s &= \sum_\gamma h_\gamma Y_\gamma(\lambda, \mu)
\end{aligned}
\right\} \quad (77)
$$

where $\gamma = n_r + i\ell_r$ represents a wave vector index of the spherical harmonic

$$Y_\gamma(\lambda, \mu) = \exp(i\ell_\gamma \lambda)\, P_\gamma(\mu)$$

with $P_\gamma(\mu)$ being the Legendre polynomial of rank and degree given by γ . The orthogonal spherical harmonics are normalized such that integration over the unit spherical surface (s) yields the orthogonal property

$$\frac{1}{4\pi} \int_s Y_\alpha Y_\beta^* \, ds = \delta_{\alpha,\beta} \quad . \qquad (78)$$

Complex conjugate values are denoted by an asterisk. Another useful property of the set of spherical harmonics is that they satisfy the differential equation

$$\nabla^2 Y_\gamma = -c_\gamma Y_\gamma, \quad c_\gamma = n_\gamma(n_\gamma + 1) \quad . \tag{79}$$

In order to reduce the model equation to spectral form we introduce solutions (77), multiply each equation by a conjugate polynomial (Y^*_γ) and integrate over the unit sphere. This procedure, through use of the orthogonality condition (78), allows us to write each term in the model equations in the form of a single expansion coefficient.

The details of the spectral transformation of the model equations are contained in Appendix D with the result that we can now write the prediction set (74) in the spectral form

$$\left.\begin{aligned}
&\frac{d\psi_\gamma}{dt} - L^{(1)}_\gamma{}_{\psi_\gamma} - M^{(1)}_\gamma{}_{\psi_\gamma} = A^{(1)}_\gamma - D_\gamma X_{\gamma-1} + E_\gamma X_{\gamma+1} \\
&\frac{d\Psi_\gamma}{dt} - L^{(2)}_\gamma{}_{\psi_\gamma} - M^{(2)}_\gamma{}_{\psi_\gamma} = A^{(2)}_\gamma + D_\gamma X_{\gamma-1} - E_\gamma X_{\gamma+1} - \\
&\qquad\qquad - D_\gamma X_{\gamma-1} + E_\gamma X_{\gamma+1} \\
&\frac{d\theta_\gamma}{dt} - L^{(3)}_\gamma{}_{\theta_\gamma} - M^{(3)}_\gamma{}_{\Theta_\gamma} = A^{(3)}_\gamma + A^{(5)}_\gamma - A^{(9)}_\gamma + N^{(3)}_\gamma \\
&\frac{d\Theta_\gamma}{dt} - L^{(4)}_\gamma{}_{\Theta_\gamma} - M^{(4)}_\gamma{}_{\theta_\gamma} = A^{(4)}_\gamma + A^{(6)}_\gamma + A^{(7)}_\gamma + A^{(8)}_\gamma + \\
&\qquad\qquad + A^{(9)}_\gamma + N^{(4)}_\gamma
\end{aligned}\right\} \tag{80}$$

Similarly, the surface boundary relationships in (76) become

$$\left\{\begin{aligned}
&\chi_\gamma = \frac{B_s}{A_s}\, c_\gamma A^{(8)}_\gamma \\
&(F^{SH}_4 - F^{LWC}_4)T_\gamma - W^{(1)}_\gamma(\theta_4) = (F^{LW}_o)_\gamma - (F^{SW}_A)_\gamma + W^{(2)}_\gamma + \\
&\qquad\qquad + W^{(3)}_\gamma - F^{SH}_3{}_{\Theta_\gamma} \text{ (for land and ice)} \\
&T_\gamma = \text{constant (over oceans)}
\end{aligned}\right\} \tag{81}$$

while the diagnostic thermal wind relationship reduces to

$$B\overline{\theta}_{\gamma} = D_{\gamma}(\psi_{\gamma-1} - \Psi_{\gamma-1}) - E_{\gamma}(\psi_{\gamma+1} - \Psi_{\gamma+1}) \quad . \tag{82}$$

The spectral set (80) - (82) is complete but we note that it does not contain an explicit relationship which defines the set $\{X_{\gamma}\}$ as required by (80). Such a relationship can be obtained by applying the substantial time derivative operator to the thermal wind (82) and substituting from (80) to eliminate time dependency and arrive at a diagnostic set of spectral equations in $\{X_{\gamma}\}$. For convenience we choose to defer the details of this development to the next section.

K. Space truncation and finite difference form of the equations

We will truncate the spectral equations using the rhomboidal scheme as applied by Elsaesser (1966a). This is accomplished through approximation of each infinite series representation in (77) to a finite series including γ_{max} wave vectors γ . Since γ depends upon two quantities ℓ_{γ} and n_{γ} ($\gamma = n_{\gamma} + i\ell_{\gamma}$) which represent the planetary wave number (ℓ_{γ}) and the degree of the polynomial (n_{γ}) both of which must be integers, we see that two separate truncation specifications must be made. The conditions for a rhomboidal truncation require determination of a maximum planetary wave number (ℓ_{max}) and an integer (N) to denote the maximum number of wave vectors for a given ℓ_{γ} . Additional constraints are that $n_{\gamma} \geq |\ell_{\gamma}|$ and, since our model will be limited to a hemispheric integration, each series in (77) can be characterized as either an even or an odd expansion (with respect to the equator). Consequently, every combination of $n_{\gamma} + \ell_{\gamma}$ for a given series must be

odd for stream functions (this has the effect of forcing the zonal wind field to be symmetric with respect to the equator while the meridional wind field is antisymmetric) and even for all other quantities in (77). Thus the rhomboidal truncation used here includes all γ vectors in the set

$$\left.\begin{array}{l} 0 \leq |\ell_\gamma| \leq |\ell_{max}| \\ n_\gamma = |\ell_\gamma| + 2j - k, \text{ for } 1 \leq j \leq N \\ \text{and} \\ \left\{\begin{array}{l} k = 1 \text{ for odd expansions} \\ k = 2 \text{ for even expansions} \end{array}\right. \end{array}\right\} \quad . \quad (83)$$

Baer and Alyea (1971) conducted a number of experiments to establish the dependence of the solutions of general circulation calculations on spectral truncation using a two-level, quasi-geostrophic, fixed stability model with simple heating and diffusion terms. These experiments showed that at least for the model under consideration, in order to arrive at a reasonable description of the general circulation a minimum of at least twelve planetary waves and eight degrees of freedom in latitude should be included. Since the present model is somewhat larger in scope and detail than was used in the experiments by Baer and Alyea we have correspondingly chosen to increase the number of vector components within the truncated system to include all planetary waves through wave number sixteen. Thus, in (83) we set $|\ell_{max}| = 16$ and $N = 8$. An n-ℓ diagram outlining the domain of vector components included in the present experiment is drawn as Fig. 3.

Let us now consider the numerical scheme to be used for the integration of the model equations, (80) - (82). It is convenient to consider

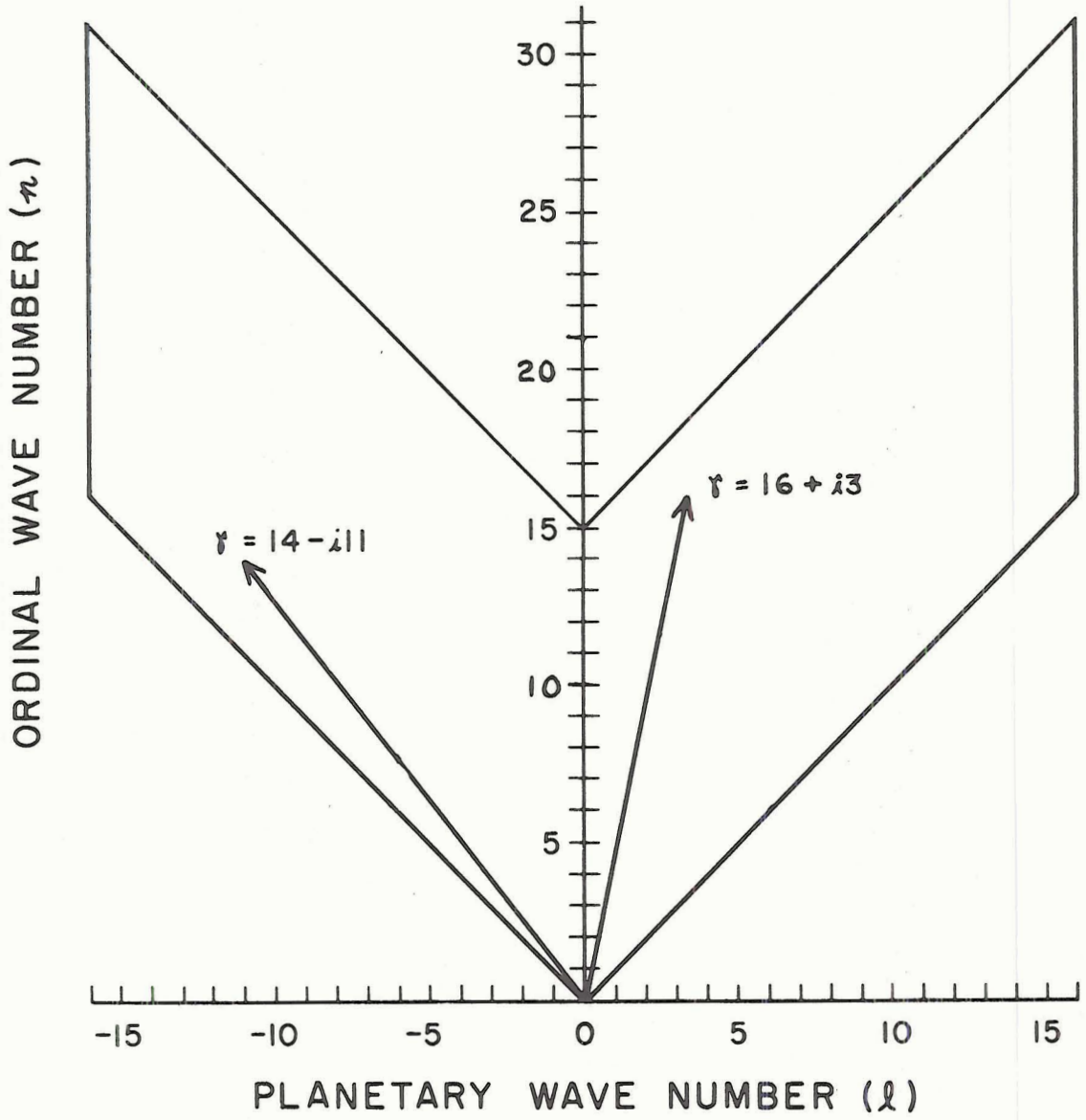

FIGURE 3. Spectral map outlining the truncation limits of the present experiment. Two sample wave vectors are included.

the streamfunction and temperature fields of (80) in terms of their mean and shear components and to this end we define

$$\left.\begin{aligned} \zeta_\gamma &\equiv \tfrac{1}{2}(\psi_\gamma + \Psi_\gamma) \\ \tau_\gamma &\equiv \tfrac{1}{2}(\psi_\gamma - \Psi_\gamma) \\ \overline{\theta}_\gamma &\equiv \tfrac{1}{2}(\theta_\gamma + \Theta_\gamma) \\ \sigma_\gamma &\equiv \tfrac{1}{2}(\theta_\gamma - \Theta_\gamma) \end{aligned}\right\} . \tag{84}$$

We can now evaluate (80) in terms of definitions (84) in the form

$$\left.\begin{aligned} \frac{d\zeta_\gamma}{dt} - P_\gamma^{(M)}\zeta_\gamma &= N_\gamma^{(M)} \\ \frac{d\tau_\gamma}{dt} - P_\gamma^{(S)}\tau_\gamma &= N_\gamma^{(S)} - D_\gamma X_{\gamma-1} + E_\gamma X_{\gamma+1} \\ \frac{d\overline{\theta}_\gamma}{dt} - H_\gamma^{(M)}\overline{\theta}_\gamma &= S_\gamma^{(M)} + G_\gamma(X) \\ \frac{d\sigma_\gamma}{dt} - H_\gamma^{(S)}\sigma_\gamma &= S_\gamma^{(S)} \end{aligned}\right\} \tag{85}$$

where we have defined

$$\left.\begin{aligned} P_\gamma^{(M)} &= \tfrac{1}{2}(L_\gamma^{(1)} + L_\gamma^{(2)} + M_\gamma^{(1)} + M_\gamma^{(2)}) \\ P_\gamma^{(S)} &= \tfrac{1}{2}(L_\gamma^{(1)} + L_\gamma^{(2)} - M_\gamma^{(1)} - M_\gamma^{(2)}) \\ H_\gamma^{(M)} &= \tfrac{1}{2}(L_\gamma^{(3)} + L_\gamma^{(4)} + M_\gamma^{(3)} + M_\gamma^{(4)}) \\ H_\gamma^{(S)} &= \tfrac{1}{2}(L_\gamma^{(3)} + L_\gamma^{(4)} - M_\gamma^{(3)} - M_\gamma^{(4)}) \\ N_\gamma^{(M)} &= \tfrac{1}{2}(A_\gamma^{(1)} + A_\gamma^{(2)}) - \tfrac{1}{2}(D_\gamma X_{\gamma-1} - E_\gamma X_{\gamma+1}) + \\ &\quad \tfrac{1}{2}(L_\gamma^{(1)} - L_\gamma^{(2)} - M_\gamma^{(1)} + M_\gamma^{(2)})\tau_\gamma \end{aligned}\right\} . \tag{86}$$

$$
\begin{aligned}
N_\gamma^{(S)} &= \frac{1}{2}(A_\gamma^{(1)} - A_\gamma^{(2)}) + \frac{1}{2}(D_\gamma \chi_{\gamma-1} - E_\gamma \chi_{\gamma+1}) + \\
&+ \frac{1}{2}(L_\gamma^{(1)} - L_\gamma^{(2)} + M_\gamma^{(1)} - M_\gamma^{(2)})\zeta_\gamma \\
S_\gamma^{(M)} &= \frac{1}{2}(A_\gamma^{(3)} + A_\gamma^{(4)} + A_\gamma^{(7)} + A_\gamma^{(8)} + N_\gamma^{(3)} + N_\gamma^{(4)}) + \\
&+ \frac{1}{2}(L_\gamma^{(3)} - L_\gamma^{(4)} - M_\gamma^{(3)} + M_\gamma^{(4)})\sigma_\gamma \\
S_\gamma^{(S)} &= \frac{1}{2}(A_\gamma^{(3)} - A_\gamma^{(4)} + A_\gamma^{(5)} - A_\gamma^{(6)} - A_\gamma^{(7)} - A_\gamma^{(8)} - \\
&- 2A_\gamma^{(9)} + N_\gamma^{(3)} - N_\gamma^{(4)}) + \frac{1}{2}(L_\gamma^{(3)} - L_\gamma^{(4)} + M_\gamma^{(3)} - \\
&- M_\gamma^{(4)})\bar{\theta}_\gamma \\
G_\gamma(X) &= \frac{1}{2}(A_\gamma^{(5)} + A_\gamma^{(6)})
\end{aligned}
\qquad \text{(86 cont.)}
$$

For the truncation of wave vectors γ outlined above we must solve the system of ordinary, nonlinear differential equations (85) through use of a numerical time integration procedure. Due to its success in previous experiments and ease of application we have chosen a centered difference (leapfrog) scheme for all time extrapolations. To prepare for numerical integration we first introduce an integrating factor in order to treat the linear terms exactly (Baer and Simons, 1970) and thus, for example, we extrapolate numerically the first equation of (85) in the form

$$
\frac{d}{dt}\left(e^{-P_\gamma^{(M)} t}\zeta_\gamma\right) = e^{-P_\gamma^{(M)} t} N_\gamma^{(M)} \quad . \qquad (87)
$$

This procedure has the main advantage of eliminating computational instabilities associated with diffusive terms in the centered difference scheme. Applying this methodology to (85) yields in centered difference form

$$
\left.
\begin{aligned}
\zeta_\gamma(t+\Delta t) &= e^{2P_\gamma^{(M)}\Delta t}\zeta_\gamma(t-\Delta t) + 2\Delta t\, e^{P_\gamma^{(M)}\Delta t} N_\gamma^{(M)} \\
\tau_\gamma(t+\Delta t) &= e^{2P_\gamma^{(S)}\Delta t}\tau_\gamma(t-\Delta t) + 2\Delta t\, e^{P_\gamma^{(S)}\Delta t}(N_\gamma^{(S)} - \\
&\quad - D_\gamma X_{\gamma-1} + E_\gamma X_{\gamma+1}) \\
\bar{\theta}_\gamma(t+\Delta t) &= e^{2H_\gamma^{(M)}\Delta t}\bar{\theta}_\gamma(t-\Delta t) + 2\Delta t e^{H_\gamma^{(M)}\Delta t}[S_\gamma^{(M)} + \\
&\quad + G_\gamma(X)] \\
\sigma_\gamma(t+\Delta t) &= e^{2H_\gamma^{(S)}\Delta t}\sigma_\gamma(t-\Delta t) + 2\Delta t e^{H_\gamma^{(S)}\Delta t} S_\gamma^{(S)}
\end{aligned}
\right\} . \quad (88)
$$

We can now develop the explicit diagnostic relationship defining the set $\{X_\gamma\}$ as discussed in the previous section. Application of the substantial time derivative operator to (82) converts the thermal wind relationship to

$$
B\frac{d\bar{\theta}_\gamma}{dt} = 2\left(D_\gamma \frac{d\tau_{\gamma-1}}{dt} - E_\gamma \frac{d\tau_{\gamma+1}}{dt}\right) \quad (89)
$$

in which we have made use of the definition of the shear streamfunction in (84). Replacing the time derivatives in (89) with their centered difference analogs and substituting from (88) yields a diagnostic relationship for $\{X_\gamma\}$ in the tridiagonal form at time t

$$
f_\gamma^{(1)} X_{\gamma-2} + f_\gamma^{(2)} X_\gamma + f_\gamma^{(3)} X_{\gamma+2} = R_\gamma - g_\gamma(X) \quad . \quad (90)
$$

For details of this development along with definitions of all quantities in (90) and an outline of the method of solution the reader is referred to Appendix E. It can be shown that (90) is merely a special representation in the spectral domain of the general three-dimensional ω equation and as such provides an important physical link between the dynamic and thermodynamic properties of the model atmosphere. This is accomplished

because (90) guarantees that the balancing thermal wind relationship (82) is maintained throughout the entire time integration period.

There remains only the task of outlining the solutions to the diagnostic surface boundary relationships (81). The solutions for χ_γ and T_γ (oceans) are obvious and require no further development here. However, in order to invert the surface temperature equation to obtain T_γ (land and ice) we will write this equation in the form

$$(F_4^{SH} - F_4^{LWC})T_\gamma = W_\gamma \quad \text{(land and ice)} \tag{91}$$

where we have defined

$$W_\gamma(F_0^{LW}, F_1^{LW}, F_3^{LW}, F_4^{LWW}, F_A^{SW}, F_3^{SH}, \theta_1, \theta_3, \theta_4) =$$

$$= (F_0)_\gamma^{LW} - (F_A^{SW})_\gamma + W_\gamma^{(1)}(\theta_4) + W_\gamma^{(2)} + W_\gamma^{(3)} - \tag{92}$$

$$- F_3^{SH}\theta_\gamma \quad .$$

All terms on the right side of (92) have been defined in Appendix B and Chapter II, section F. Their spectral forms are shown in Appendix D (Table D3). As can be seen in (B-14) and (B-19) the LW flux terms on the right side of (92) are functions of the 1000 mb water vapor absorption path length $u_w(1000)$ which from (41) and (44), can be seen to be dependent upon the zonal 1000 mb (surface) temperature, T_{4Z}. Expanding this quantity explicitly in time we can write

$$T_{4Z}(t) = T_{4Z}(t - \Delta t) + \frac{\partial T_{4Z}}{\partial t}\Delta t$$

and, as a first approximation,

$$T_{4Z}(t) \tilde{=} T_{4Z}(t - \Delta t) \quad . \tag{93}$$

This same assumption is applied to the total surface temperature quantity θ_4 in $W_\gamma^{(1)}$. These approximations can be used because the surface temperature varies slowly in time (diurnal variations are ignored throughout our model) and thus the higher order term of such an explicit expansion are small (Δt of $\frac{1}{2}$ hour are used). Application of this procedure to the LW flux terms in (92) for evaluation of W_γ has the effect of uncoupling the vector equation set represented by (91) and thus the surface boundary relationships (81) reduce to the set of uncoupled equations

$$\left.\begin{aligned} \chi_\gamma &= \frac{B_s}{A_s} c_\gamma A_\gamma^{(8)} \\ T_\gamma &= \frac{W_\gamma}{(F_4^{SH} - F_4^{LWC})} \quad \text{(land and ice)} \\ T_\gamma &= T_\gamma(t = 0) \quad \text{(oceans)} \end{aligned}\right\} \tag{94}$$

where all time dependent quantities, except as noted, apply at time t and all indices are truncated according to (83) for $|\ell_{max}| = 16$ and $N = 8$. We see that (88), (90), and (94) form a complete set prepared for numerical integration.

L. The numerical procedure

The time iterations are initiated using the Euler forward scheme for the first time step. Subsequent time steps are performed with the centered difference scheme except that the parasitic $2\Delta t$ modes associated with this scheme are inhibited through use of a restart technique (Kikuchi, 1969) in which the Euler forward scheme is periodically inserted (every 48 time steps) for one iteration. Following this

procedure a time increment of $\Delta t = 1/2$ hour was used and found to be computationally stable.

At a given time t we begin the numerical calculation by evaluating the nonlinear terms $A_\gamma^{(1)} - A_\gamma^{(4)}$, $A_\gamma^{(8)}$ along with all linear and inhomogeneous time dependent quantities of (88) not involving the integrated velocity potentials X_γ and χ_γ and the surface temperatures T_γ. We next evaluate the diagnostic surface conditions (94) to obtain χ_γ and T_γ. The surface temperature coefficients (T_γ) are calculated by applying the equation for land and ice over the entire northern hemisphere (using an albedo of .07 for oceans) and then filtering the resultant field with the spectral representation of a land and ice (1) versus oceans (0) step function. An analysis of the spectral representation for this step function under current summer conditions is shown in Fig. 4. The resulting land and ice surface temperature coefficient field is then added to the constant pelagic field to completely specify the northern hemisphere surface temperatures.

We can now calculate all the terms of (88) involving χ_γ and T_γ including the diabatic heating functions provided that we evaluate $f(\omega_2)$ [see Eqs. (63) and (64)] at time $t - \Delta t$. It should be noted here that in order to eliminate computational instabilities associated with large high frequency components of the upward directed vertical motion fields [$f(\omega_2)$ and $f(\omega_4)$] in the condensation heating computations we filter $f(\omega_2)$ and $f(\omega_4)$ in spectral terms such that $n_\gamma \leq 10$ and $\ell_\gamma \leq 10$ ($\gamma = n_\gamma + i\ell_\gamma$). Thus, the high frequency components of the condensation heating are eliminated and the total diabatic heating quantities can be evaluated. With this, all terms on the right sides of (88) are known with the exception of those involving X_γ.

However, inversion of (90) as outlined in Appendix E provides the set $\{\chi_\gamma\}$ required for the remaining terms and the extrapolation to time $t + \Delta t$ proceeds as outlined above.

III. THE CLIMATOLOGICAL EXPERIMENTS

A. Experimental approach

Starting with an initial atmospheric state corresponding to mean summer (July) conditions for the northern hemisphere taken from current data, two separate versions of the model have been integrated forward in time for sixty days each. We will refer to these two calculations as Model P, designating the simulation experiment for the present summer climate, and Model Q, referring to the corresponding simulation experiment designed to represent the climatology during the last great ice age maximum of the Quaternary period (Wisconsin/Würm), about 18,000 years ago. The principle difference between the models lies in the specification of the surface boundary conditions, especially concerning the location and topography of continental glaciers, the distribution of pack ice, and oceanic surface temperatures. Model P boundary values were obtained from conventional data sources. However, for the ice age simulation (Model Q), these data had to be constructed in approximate fashion from a variety of paleogeologic sources. Details concerning specification of the initial and surface boundary conditions are contained in the next section.

Analysis of the experimental results is to be approached from two directions. Since we intend to stress differences between the two model calculations rather than the absolute values obtained, we will first compare certain time dependent properties of the solutions as they develop such as the total kinetic energy and mean momentum. Such a comparison will give us a general picture of the nature of the integrated solutions as well as an indication of the relative activity of the

fields must be reduced to spectral form. To this end we have utilized the expansion technique of Ellsaesser (1966b) to obtain spectral coefficients. Thus, the potential temperature fields at the two levels can be transformed directly to spectral form. An analysis of these fields (in terms of temperature rather than potential temperature) derived from the spectral coefficients is shown in Fig. 5. It should be noted here that these values have been slightly adjusted so that the thermal wind relationship (82) is satisfied. This is necessary in order to preserve the energy constraints of the unforced equations (Lorenz, 1960) and eliminate spurious solutions which might arise due to an initial thermal imbalance.

Specification of the required initial streamfunction coefficients, however, is not quite so straight forward. These are to be obtained from the geostrophic wind field but in order to simplify the computational problem we will introduce a change of variable following the example of Roberts (1966). Thus, we define in nondimensional form (see Appendix C) with k either 1 or -1

$$\left.\begin{aligned} U &= (1 - \mu^2)^{k/2} u_g \\ V &= (1 - \mu^2)^{k/2} v_g \end{aligned}\right\} \tag{95}$$

where u_g and v_g are respectively the zonal and meridional components of the geostrophic wind and μ is the sine of latitude. We then expand U and V in spectral form using the definitions

$$\left.\begin{aligned} U &= \sum_\gamma U_\gamma Y_\gamma(\lambda, \mu) \\ V &= \sum_\gamma V_\gamma Y_\gamma(\lambda, \mu) \end{aligned}\right\} \tag{96}$$

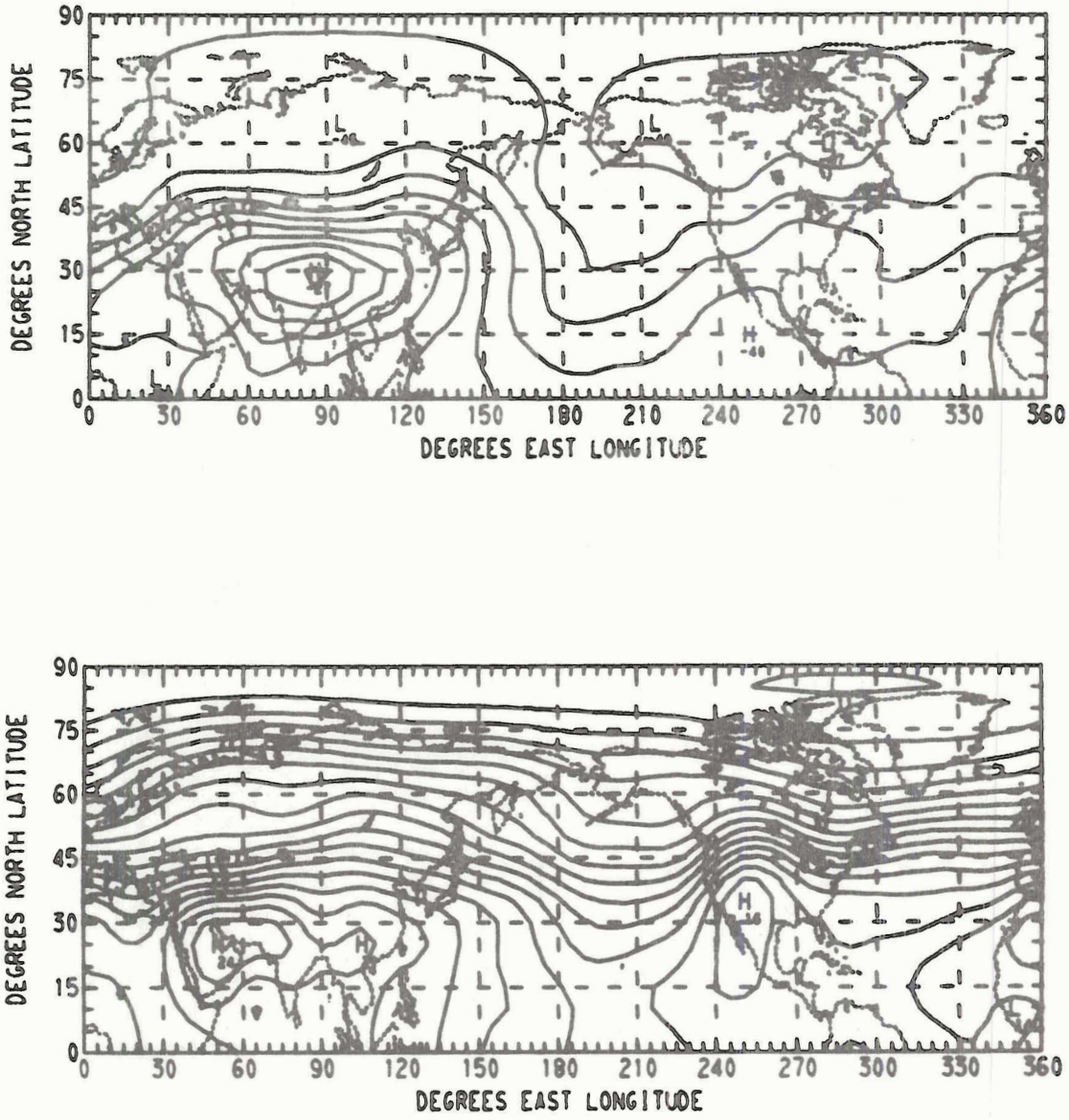

FIGURE 5. Initial 250 mb (above) and 750 mb (below) temperature fields. Data represents observed mean July conditions. Contour intervals are $2^{o}C$.

as was done for the model variables in (77). Using the definition for the vertical component of vorticity ($\nabla^2\psi = \mathbb{k} \cdot \nabla \times \mathbf{V}$) and applying (95) with k set here to -1 we can write in nondimensional form

$$\nabla^2\psi = \frac{1}{(1-\mu^2)^{\frac{1}{2}}}\frac{\partial v_g}{\partial \lambda} - \frac{\partial (1-\mu^2)^{\frac{1}{2}} u_g}{\partial \mu} = \frac{\partial V}{\partial \lambda} - \frac{\partial (1-\mu^2) U}{\partial \mu} \quad . \tag{97}$$

Inserting solutions from (77) and (96) into (97), applying (79), and performing the indicated derivatives yields

$$\begin{aligned} -\sum_{\beta} c_\beta \psi_\beta Y_\beta(\lambda, \mu) \;=\; & i\sum_{\beta} \ell_\beta V_\beta Y_\beta(\lambda, \mu) + \sum_{\beta} U_\beta e^{i\ell_\beta \lambda} \times \\ & \times \left[(1-\mu^2)\frac{dP_\beta}{d\mu} - 2\mu P_\beta\right] \quad . \end{aligned} \tag{98}$$

If we now multiply (98) through with an orthogonal function (say Y^*_γ) and integrate over the unit sphere we can show that (for details of this procedure, see Appendix D)

$$\begin{aligned} \psi_\gamma = & -ic_\gamma^{-1}\ell_\gamma V_\gamma - \frac{1}{n_\gamma}\left[\frac{(n_\gamma + \ell_\gamma)(n_\gamma - \ell_\gamma)}{(2n + 1)(2n - 1)}\right]^{\frac{1}{2}} U_{\gamma-1} + \\ & + \frac{1}{(n_\gamma + 1)}\left[\frac{(n_\gamma + \ell_\gamma + 1)(n_\gamma - \ell_\gamma + 1)}{(2n_\gamma + 3)(2n_\gamma + 1)}\right]^{\frac{1}{2}} U_{\gamma+1} \quad . \end{aligned} \tag{99}$$

Thus, we see that the initial streamfunction coefficients for each of the two required levels can be directly generated from the corresponding expansion coefficients of U and V.

In summary, the computational procedure is as follows: grid point values of U and V at each level are obtained from the geostrophic wind components using (95) and the expansion technique of Ellsaesser, cited above, is then applied to obtain the coefficient sets $\{U_\gamma\}$ and $\{V_\gamma\}$ in (96). It should be mentioned that the singular polar ($\mu = 1$) values generated by (95) do not destroy the convergence of the series in (96) since the expansion procedure does not utilize

polar data. Finally, (99) yields the desired initial streamfunction coefficient set.

This procedure can be reversed to reconstruct the geostrophic wind components from the spectral streamfunction representation. Thus, it can be shown if we now use (95) with k = 1

$$
\begin{aligned}
V_\gamma &= i\ell_\gamma \psi_\gamma \\
U_\gamma &= n_\gamma \left[\frac{(n_\gamma + \ell_\gamma)(n_\gamma - \ell_\gamma)}{(2n_\gamma - 1)(2n_\gamma + 1)}\right]^{\frac{1}{2}} \psi_{\gamma-1} - \\
&\quad - (n_\gamma + 1) \left[\frac{(n_\gamma + \ell_\gamma + 1)(n_\gamma - \ell_\gamma + 1)}{(2n_\gamma + 1)(2n_\gamma + 3)}\right]^{\frac{1}{2}} \psi_{\gamma+1}
\end{aligned}
\tag{100}
$$

where then grid point values for U and V are determined from (96) and the corresponding u_g and v_g fields are constructed by inverting (95).

In order to demonstrate the validity of these spectral data reduction techniques and to prove the correctness of the initial streamfunction coefficients, we have reconstructed the geostrophic wind fields using the derived streamfunction coefficients as outlined above and have compared them with the original grid point geostrophic wind data. Computed analyses of these fields at the 250 mb and 750 mb levels using 5 degree grid intervals are shown in Fig. 6 through Fig. 9 where in each case the upper analysis was obtained from the original mean July data values and the lower analysis from the derived streamfunction coefficients and application of (100), (96) and (95). Inspection of these figures shows good correlation between the original data and the spectrally derived fields. Thus, we can assume that the streamfunction coefficients obtained from (99) adequately represent the desired initial state of the geostrophic flow field. Rather than display the initial

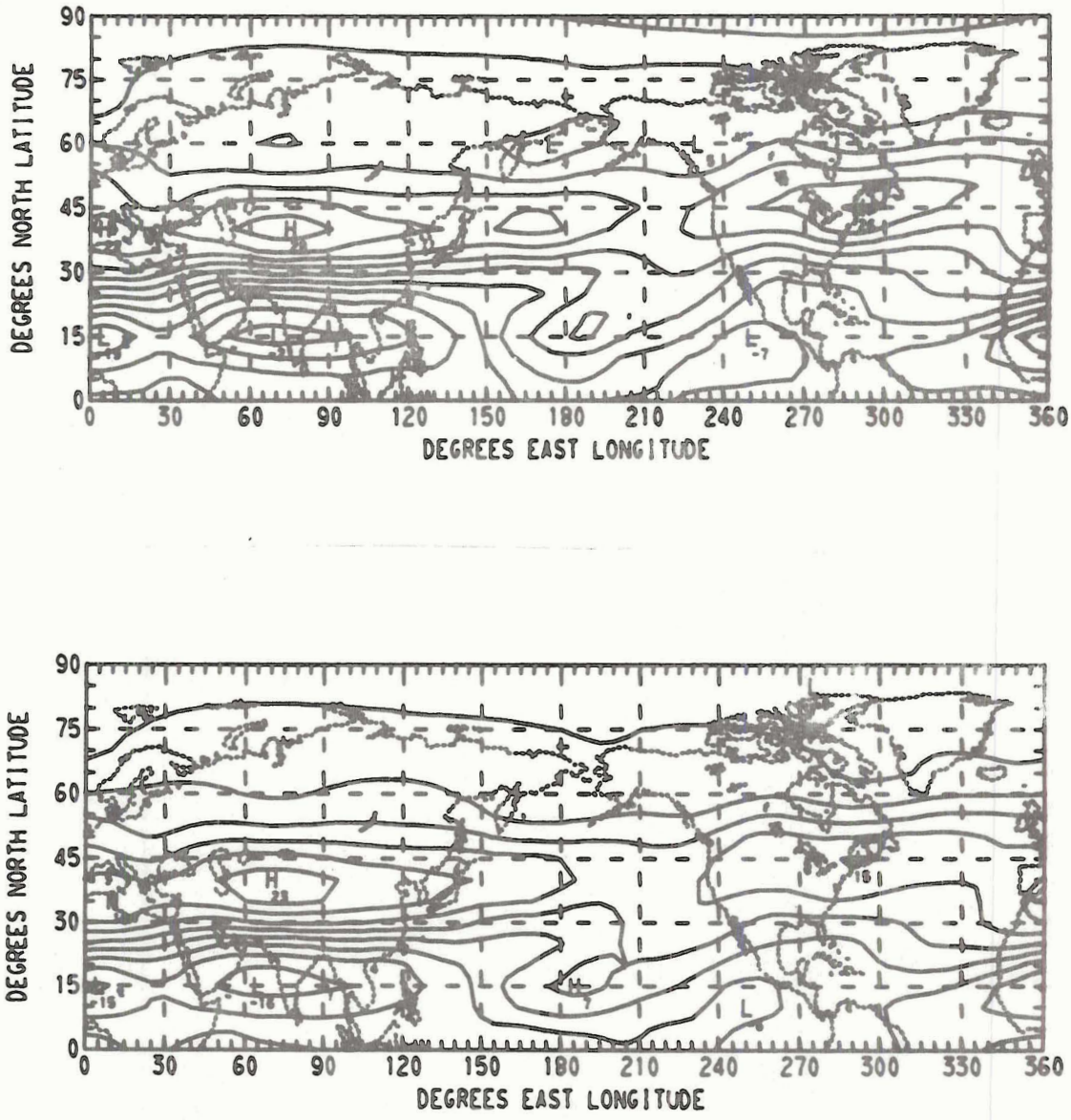

FIGURE 6. Initial 250 mb zonal geostrophic wind fields drawn directly from the initial data (above) and from the spectral representation (below). Contour intervals are 5 m/s.

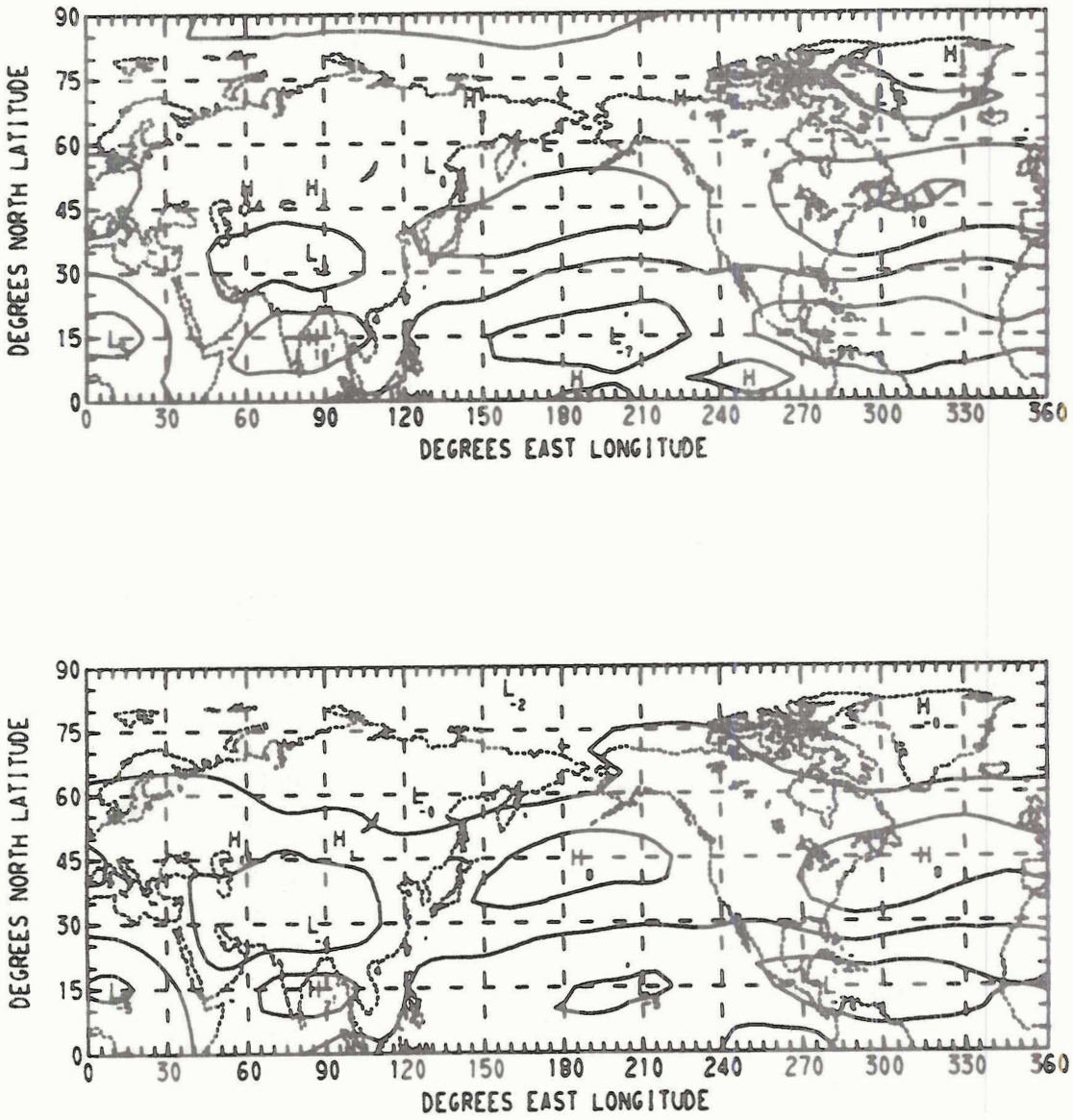

FIGURE 7. Initial 750 mb zonal geostrophic wind fields drawn directly from the initial data (above) and from the spectral representation (below). Contour intervals are 5 m/s.

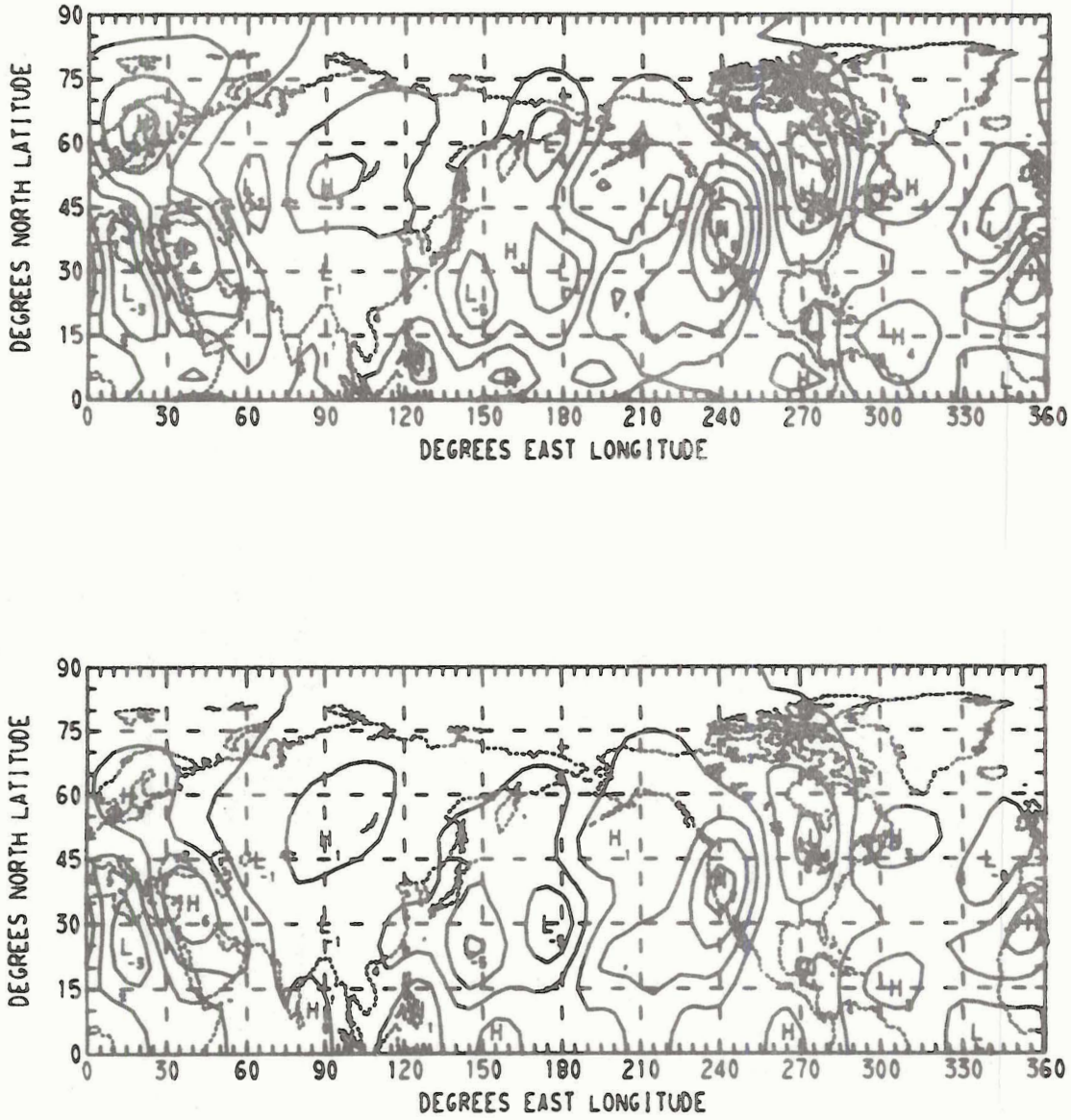

FIGURE 8. Initial 250 mb meridional geostrophic wind fields drawn directly from the initial data (above) and from the spectral representation (below). Contour intervals are 2 m/s.

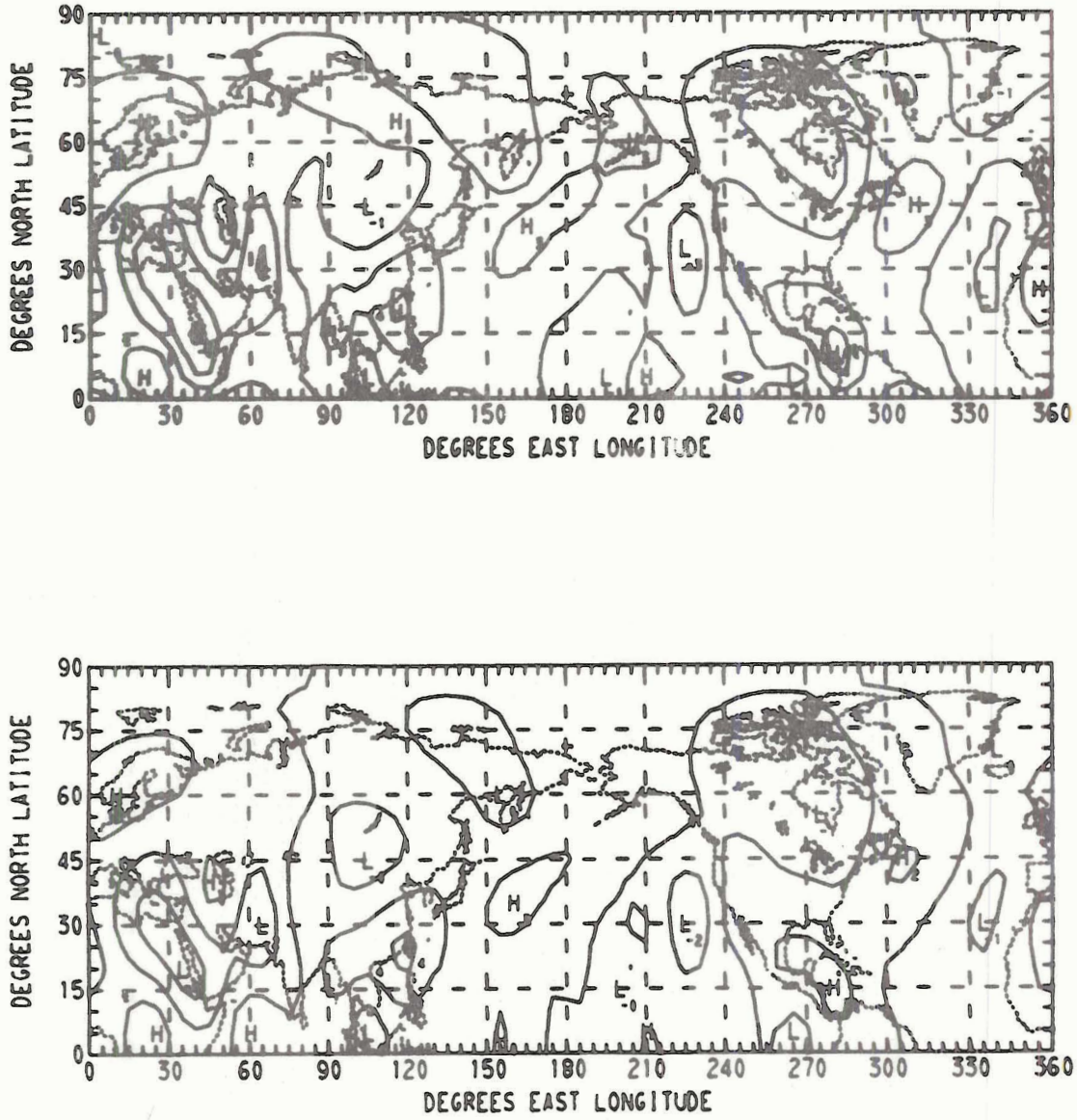

FIGURE 9. Initial 750 mb meridional geostrophic wind fields drawn directly from the initial data (above) and from the spectral representation (below). Contour intervals are 2 m/s.

streamfunction fields directly, we have chosen to represent them in terms of the meteorologically more common height deviations of the two constant pressure surfaces (250 mb and 750 mb). These values are obtained from the spectral form of the linear geostrophic balance condition (3) and have been analysed in Fig. 10.

To complete our analysis of initial values in the free atmosphere a final comment should be made concerning the initial 500 mb vertical pressure velocity ω_2 (or alternatively, X_2). Because the initial climate data is geostrophic, information relating to the irrotational part of the actual wind field (represented by the velocity potential, χ) is not complete since only geostrophic divergence is available. Hence we are unable through (6) to determine an initial representation for X_2 and since the small geostrophic divergence is negligible, we assume that it is zero everywhere. This is accomplished spectrally by setting all of the coefficients of the set $\{X_\gamma\}$ to zero at the beginning of the time integration.

We turn now to specification of the surface boundary conditions for the two models, Model P and Model Q. The requirements are that we must establish geographical limits for the distribution of continental glaciation and oceanic pack ice along with a reasonable estimate of the earth's surface topography (including the contribution from glaciers). In addition, pelagic surface temperatures and an initial 1000 mb temperature field for land and ice areas need to be determined.

We will first attack the problem of the distribution of ice. Under present July conditions (Model P) continental glaciation in the northern hemisphere is limited to Greenland while oceanic pack ice is essentially confined to the Artic Ocean basin (Lamb, 1961). However, for Model Q, representing Quaternary glaciation, both glaciers

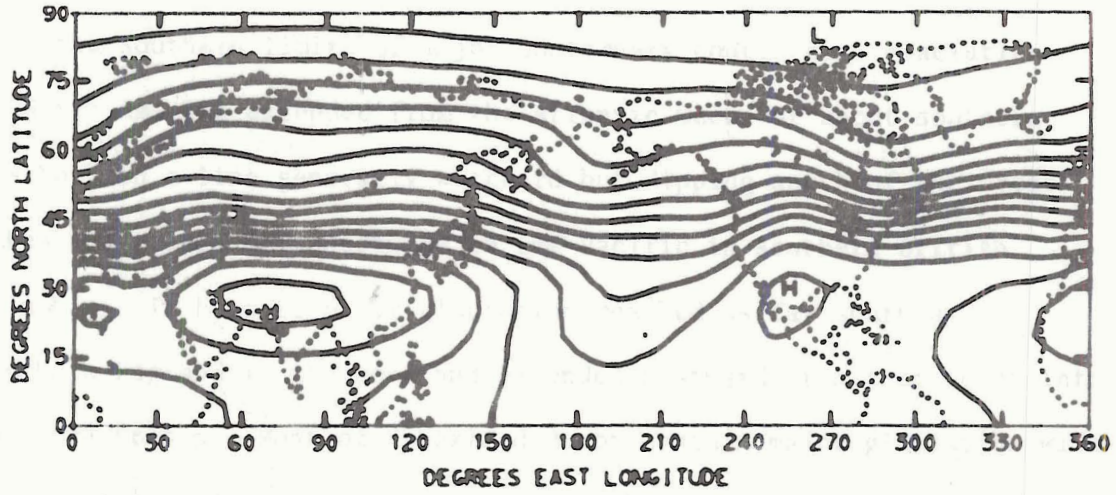

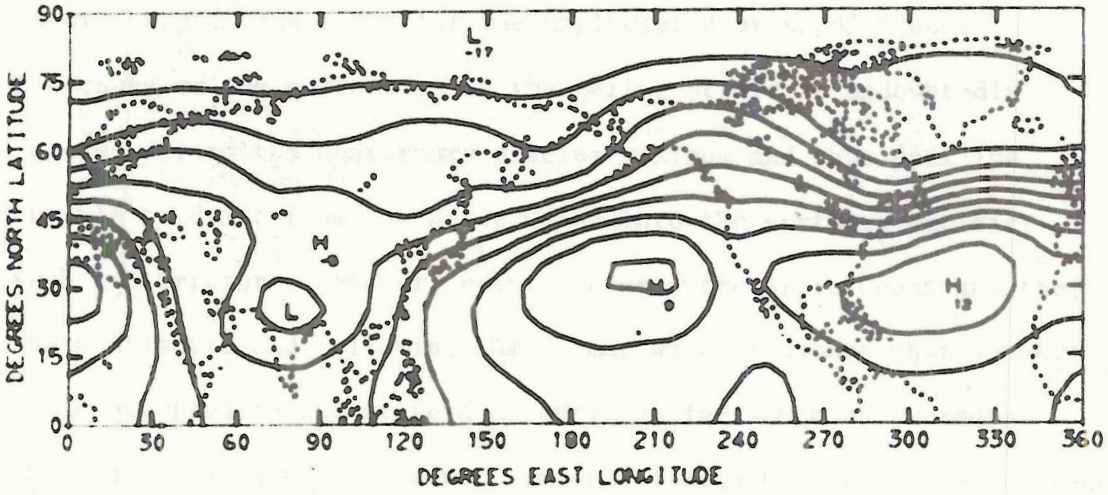

FIGURE 10. Initial height contours representing observed mean July conditions. 250 mb analysis (above) uses 6 dkm contour intervals while the 750 mb analysis (below) is drawn with 3 dkm contour intervals. Values have been obtained from the spectral representation.

this problem and a certain amount of imagination has been applied to obtain reasonable glacier height distributions. However, measurements of postglacial uplift of the earth's crust indicate that Quaternary glacial thickness maximums of about 2.5 km existed in the southern Hudson Bay region of North America and in the northern Baltic between Sweden and Finland in Europe (Gutenberg, 1954 and Flint, 1957). From these central points tentative height values were computed at other points in the ice sheets using a simple theoretical formula for steady state glaciers (Paterson, 1969). That is, letting H represent the maximum height of the glacier at point x_o we obtain the height h at distance x from x_o by applying the relationship

$$\left(\frac{h}{H}\right)^{2.5} + \left(\frac{x}{L}\right)^{1.5} = 1$$

where L is the total distance from x_o to the edge of the ice sheet on a line drawn through point x. These tentative results were then inspected as a group and a subjective smoothing was applied in order to maintain a reasonable horizontal topographic continuity.

Data for the earth's topography as it presently exists was obtained from the Geophysical Fluid Dynamics Laboratory (GFDL), Princeton, New Jersey. This data in spectral expansion form provides the surface topography required for Model P. In addition, because the Quaternary ice age maximum occurred only 18,000 years ago and is thus a relatively recent geologic event, we can assume the earth's orography outside of the glaciated areas has remained essentially unchanged. This means that we can superimpose the glacier heights obtained as described above with the current data to yield a reasonable surface topography for Model Q. The resulting boundary heights for both Model P and Model

Q as analysed from their spectral representations are shown in Fig. 11. Also included in this figure are the assumed ice limits denoted by the heavy solid line marked with X's.

The final boundary values to be treated involve the generation of 1000 mb temperature distributions. The values thus obtained in oceanic areas are to be used throughout the integrations but for land and ice they will serve only as an initial field and subsequent values are to be determined through use of a surface energy flux balance (Chapter II, section H). For both models surface grid point (rather than 1000 mb) land and ice initial temperatures are devised and then reduced according to the orographic height at each grid point to 1000 mb equivalent values. For this purpose a temperature lapse rate given by $\gamma_{CGS} = 5$ C/km is used so that the reduction procedure does not induce any vertical transport of sensible heat not already contained in the data (see Chapter II, section F). Surface temperature data for Model P over the entire northern hemisphere was obtained directly from the NCAR mean July climatological numerical values previously cited. However, determination of surface temperature data to be used in Model Q presents a somewhat more difficult problem.

First we want to make the observation that an exact initial specification of land and ice surface temperatures is not required by the model since this quantity is used only as an initial first guess field and a recalculation of the 1000 mb temperature distribution is immediately performed from a surface energy flux balance (71) in the spectral form (94). Because this flux balance depends largely upon the state of the free atmosphere as well as assumed solar forcing and surface albedoes, the initial 1000 mb temperature field is altered according to

longitude between meridians) northward to the ice edges where a temperature of 4C is assumed. Thus, along each required longitudinal line the depression function is determined from the assumed temperature depression at 30 degrees north latitude (either 3C or 5C as noted above) and the depression observed from present day data versus 4C assumed along the ice margins. Where land masses interfere with this procedure we have taken the liberty of assuming depression values from surrounding data. Addition of the depression temperature values thus obtained to current ocean surface temperatue data yields the pelagic temperatures required for Model Q. Figure 12 contains a complete analysis of the 1000 mb initial temperature fields for Models P and Q drawn from their spectral representations using the data derived as outlined above. As can be seen from this figure, north-south temperature gradients are somewhat similar over the oceans although absolute values are displaced slightly northward in Model Q. However, the major feature to be noted is the strong land-ice temperature gradients in Model Q along the southern edges of the continental glaciers in the mid latitudes. Such features are not observed in the temperature field of Model P.

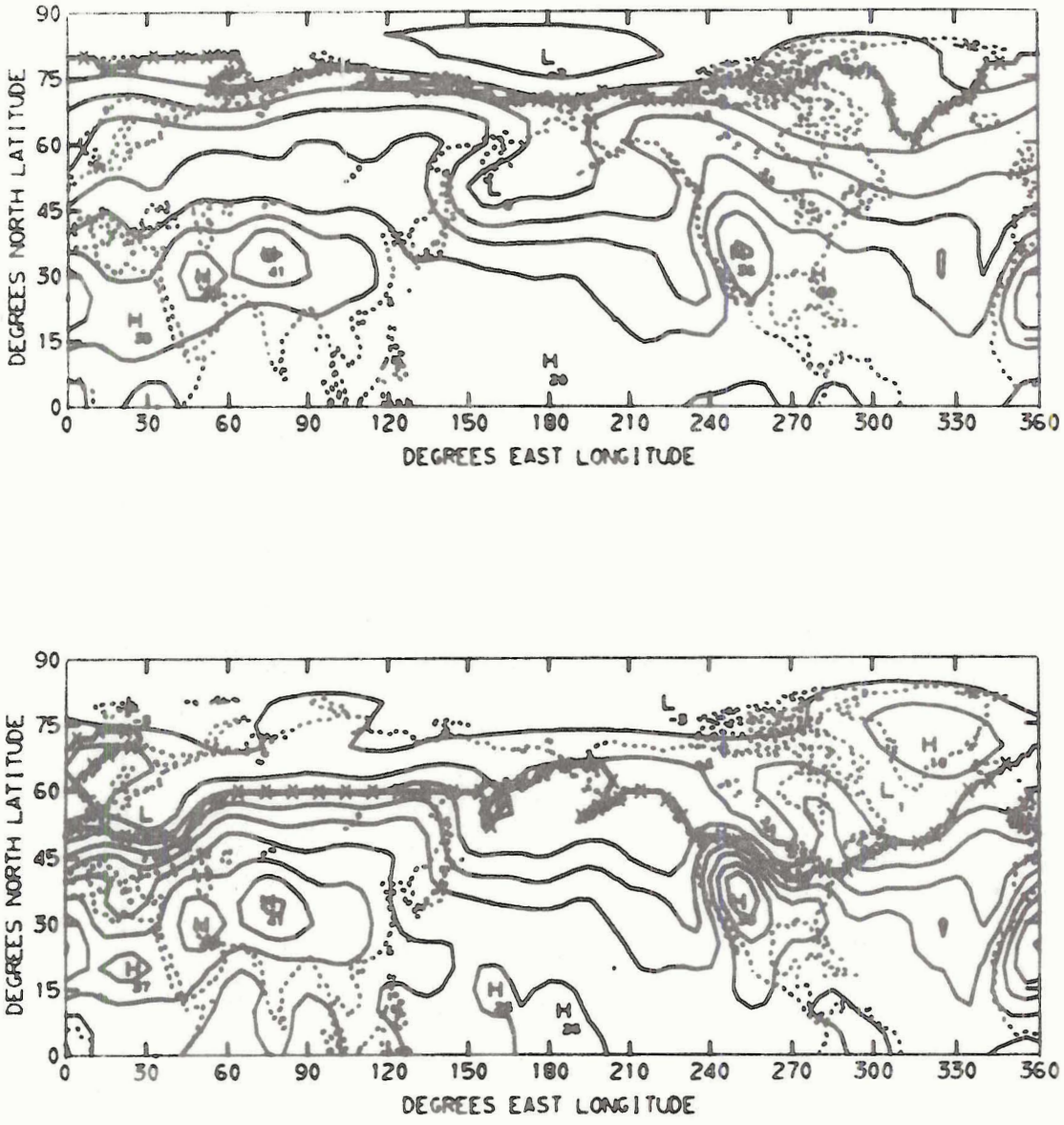

FIGURE 12. Initial 1000 mb temperature fields for Model P (above) and Model Q (below). Contour intervals are 5°C.

IV. RESULTS OF THE EXPERIMENTS

A. Comparison of the resulting solutions

Each of the two simulation models has been integrated forward in time for sixty days using mean July initial states and boundary conditions as outlined in the previous chapter. One technique which can be used to compare the time dependent characteristics of the two models is to examine the kinetic energy responses of the solutions. Since we have cast our model in the spectral domain the vector components of this quantity may be constructed immediately by the definition

$$K_\gamma \equiv \frac{1}{2} c_\gamma (\psi_\gamma \psi_\gamma^* + \Psi_\gamma \Psi_\gamma^*) \tag{101}$$

where K_γ represents the vertical mean kinetic energy in the $\Upsilon = n_\gamma + i\ell_\gamma$ component. Further, the kinetic energy contained in each planetary wave ℓ_γ without reference to its latitudinal dependence can be obtained through

$$K_\ell = \sum_{n_\gamma} K_\gamma(\ell) \quad . \tag{102}$$

An alternate but meaningful way of representing the total kinetic energy of the atmosphere is to separate it into its zonal (K_Z) and eddy (K_E) parts. These quantities are defined by

$$\left.\begin{aligned} K_Z &= K_\ell(\ell = 0) \\ K_E &= \sum_\ell K_\ell(\ell > 0) \end{aligned}\right\} \tag{103}$$

where then the total kinetic energy K is simply

$$K = \frac{1}{4}\int \nabla\psi \cdot \nabla\psi \, ds + \frac{1}{4}\int \nabla\Psi \cdot \nabla\Psi \, ds = K_Z + K_E \tag{104}$$

A second quantity which may be useful in comparing the model solutions is the mean relative zonal momentum, M_Z . By integrating the zonal wind field over the globe we can show in terms of the stream-functions of the two model layers that

$$M_Z = -\frac{1}{4} \sum_{\substack{n \\ (\ell=0)}} (\psi_n + \Psi_n) \int_{-1}^{1} (1 - \mu^2)^{\frac{1}{2}} \frac{dP_n}{d\mu} \, d\mu$$

$$= -\frac{1}{2} \sum_{\substack{n \\ (\ell=0)}} (\psi_n + \Psi_n) \, D_n \qquad (105)$$

where we have defined

$$D_n \equiv \frac{1}{2} \int_{-1}^{1} (1 - \mu^2)^{\frac{1}{2}} \frac{dP_n}{d\mu} \, d\mu \quad . \qquad (106)$$

Evaluation of D_n can either be obtained numerically or, as was done here, through an integration by parts utilizing the finite series expansion for the Legendre polynomial, P_n (see, for example, Jahnke and Emde, 1945).

With these tools in hand we can now begin to analyse the results of the model calculations. Fig. 13 contains curves depicting the total kinetic energy (K) computed at each time step from (104) along with its zonal (K_Z) and eddy (K_E) component parts (103). As can be seen from the total kinetic energy values (upper figure) the levels of dynamic activity of the two systems increase rapidly for the first ten days or so from their relatively smooth initial mean July climate states. By the end of this period the eddy waves (lower figure) have become substantially more active and evidence of a relative balance between the dissipative and kinetic energy generative terms in the dynamic solutions is beginning to appear. It would seem that by day fifteen

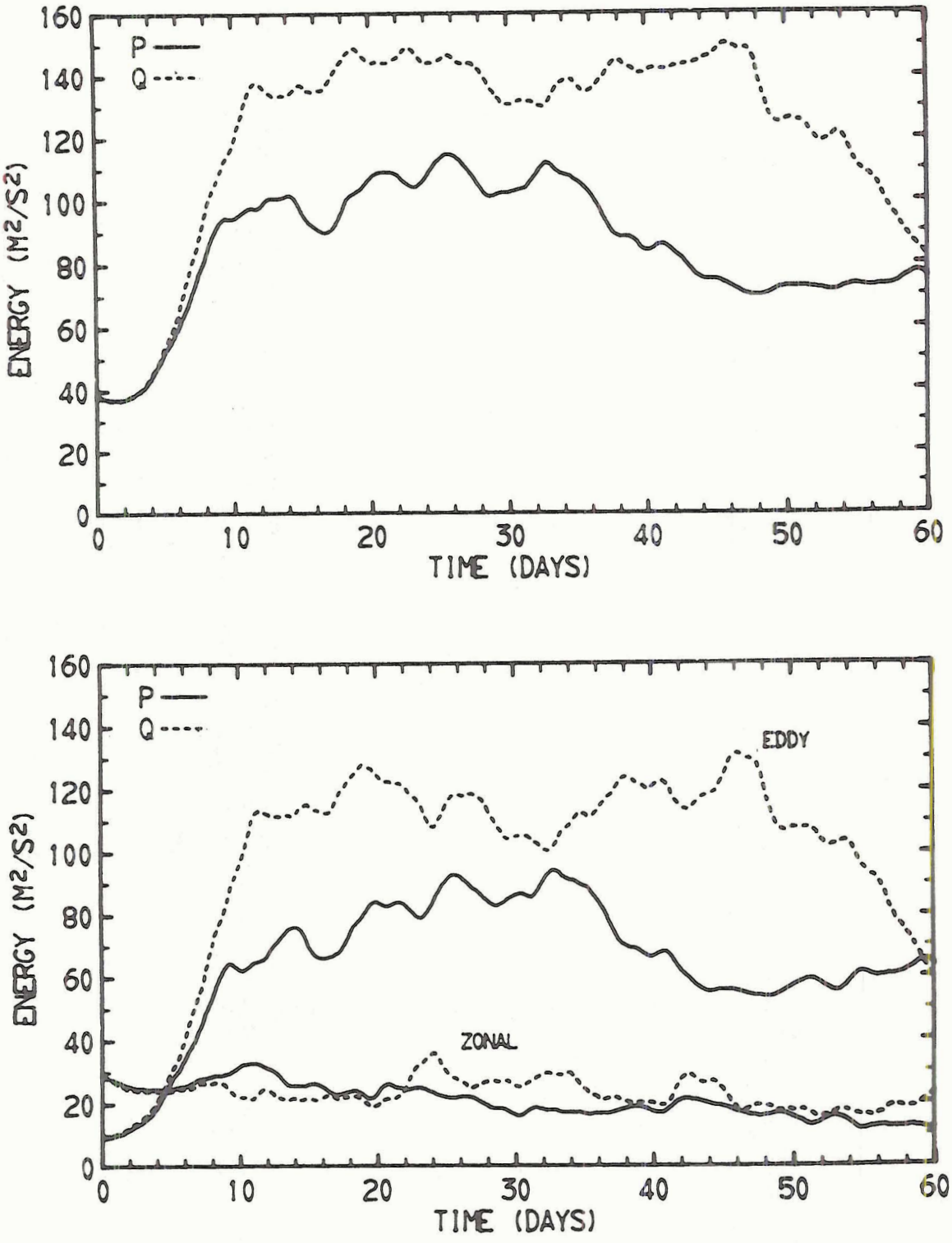

FIGURE 13. Kinetic energy quantities (per unit mass) as functions of time for Model P (solid lines) and Model Q (dashed lines). Upper figure depicts total kinetic energy (K). The lower figure contains plots for both zonal kinetic energy (K_Z) and eddy kinetic energy (K_E).

each model can be considered to have reached a state of quasi-equilibrium. As was expected, Model Q, representing Quaternary ice age conditions, reaches a substantially higher kinetic energy level over that of Model P. This, of course, can be attributed to the stronger north-south temperature gradients generated along the southern edges of the large continental glaciers and pack ice during the ice age. It must be noted that at day 48 the energy level of Model Q begins to drop rapidly and we have to admit the possibility of the occurrence of degenerate solutions as discussed in Chapter I. Model P does not show such a sharp decrease, although the kinetic energy does adjust somewhat downward between days 38 and 48, and we therefore have chosen the 30 day period between days 15 and 45 as the basis for the climates to be discussed later.

Turning now to consideration of the zonal (K_Z) and eddy (K_E) components of the total kinetic energy as shown in the lower part of Fig. 13, we see that nearly all of the difference between the kinetic energy levels of the two models can be attributed to action in the eddies. The zonal energy levels remain relatively constant throughout the calculations with little, if any, significant differences between Model P and Model Q. This feature was also noted in the computation of the mean relative zonal momentum (not shown) from (105).

In order to ascertain the relative distribution of eddy kinetic energy among the planetary waves (ℓ) contained within the limits of our model truncation ($1 \leq \ell \leq 16$), we have constructed a histogram for each model using (102). We describe the kinetic energy in these components as averages for the basic climate 30 day period (days 15-45) in Fig. 14. It is apparent that the kinetic energy levels in all of the eddy waves

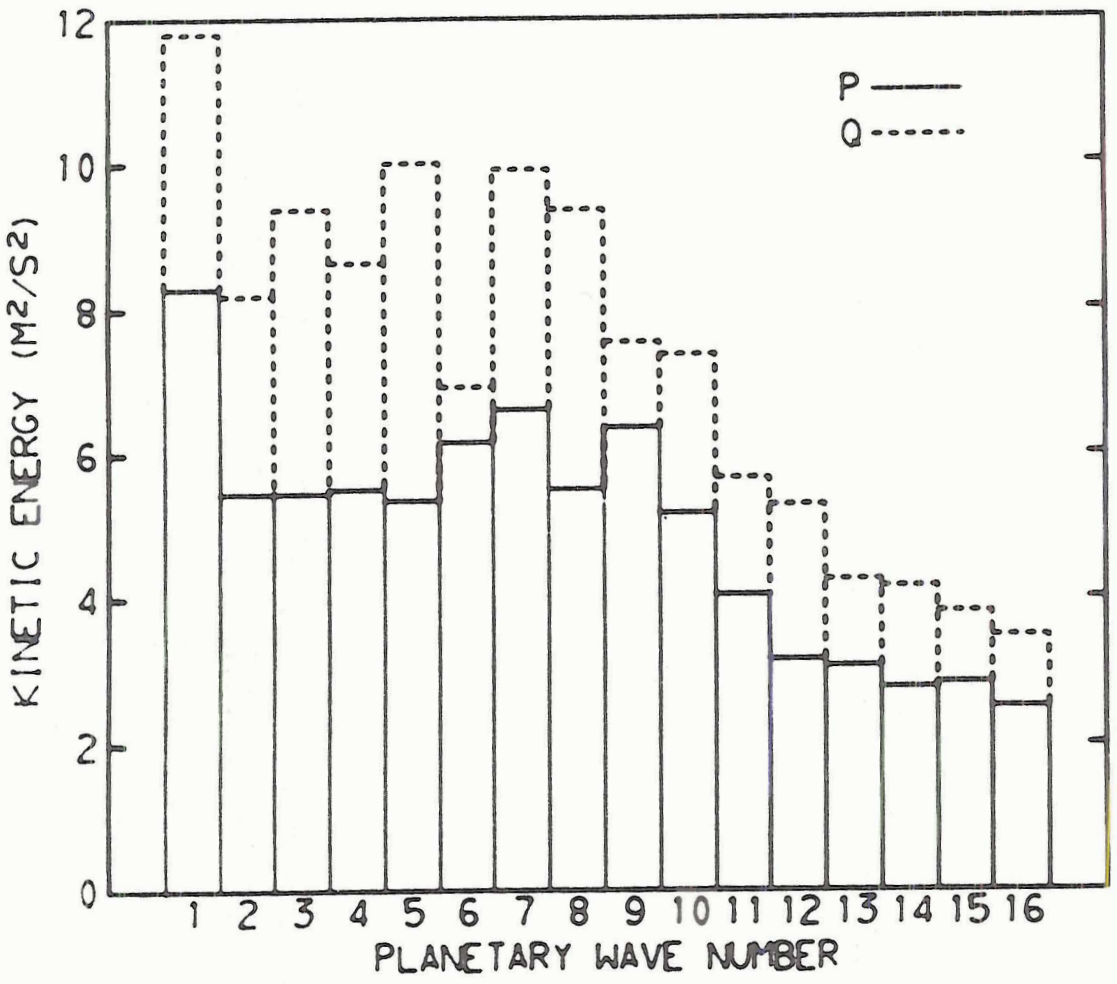

FIGURE 14. Thirty day mean (days 15 - 45) eddy kinetic energy distributions in planetary waves (ℓ) 1 - 16. Solid bars represent energy quantities for Model P. Dashed bars for Model Q.

of Model Q exceed those of Model P. However, the greatest differences appear in the very long planetary scale waves (1-5) and in the larger cyclone wave numbers 7 and 8. Because of the increase in orographic effects (Fig. 11) and the strong surface temperature gradients generated by the glaciers during the ice age of Model Q, a certain enhancement of the wave kinetic energy levels in the free atmosphere can be expected in order for the system to maintain its requirements for eddy transports of such quantities as momentum and heat. An explanation for the relative similarity observed in the kinetic energy levels of wave 6 is not readily apparent.

As mentioned above, the hemispheric average properties of the zonal flow field for each model remained quite stable throughout the time integrations. Furthermore, no substantial differences between the two models were noted. This does not imply, however, that the latitudinal distributions are necessarily similar. In order to compare these distributions we have drawn 500 mb (vertical mean) zonal wind profiles on Fig. 15 representing average values for the 30 day basic climate period (days 15-45) discussed above. The profile for Model P compares favorably with summer values at the 500 mb level presented by Lorenz (1967, Figs. 2, 4, 6, and 8) with easterlies in the polar and subtropical latitudes and westerlies elsewhere. However, the Model Q profile shows a marked departure from that of Model P over the belt from 40 to 70 degrees north latitude which, not coincidently, describes the maximum latitudinal extent of the large continental glaciers centered over Hudson Bay in North America and the northern Baltic in Europe (see Fig. 11). Thus, the presence of these glaciers acts to divert zonal momentum southward, converging near 40 degrees north latitude approximately along their southern boundaries.

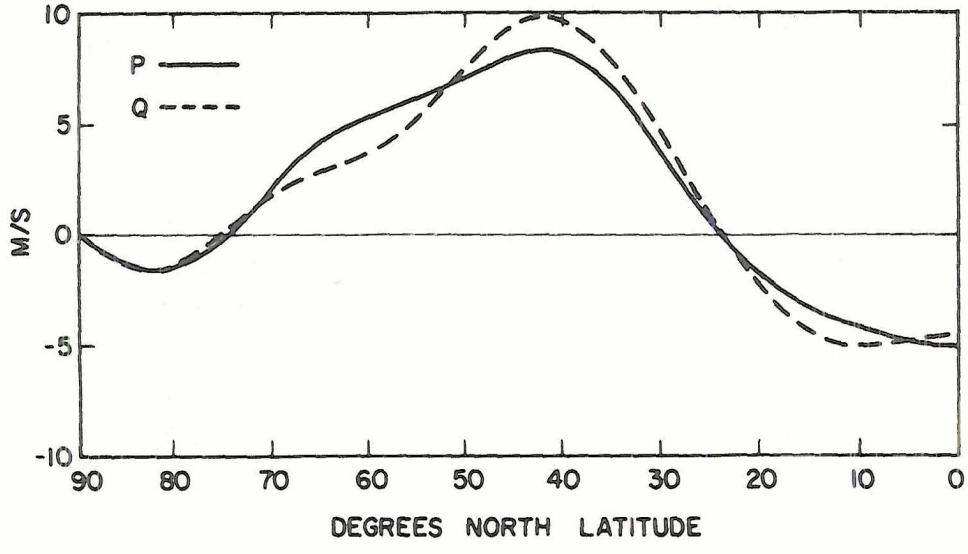

FIGURE 15. Latitudinal distribution of the vertical mean (500 mb) zonal wind for Model P (solid line) and Model Q (dashed line). Values represent average quantities for the 30 day basic climate period (days 15 - 45).

Another important feature of the general circulation of the atmosphere is the existence of large scale meridional circulation patterns. We have chosen to analyse this feature in terms of 30 day mean zonal profiles depicting vertical pressure velocities (ω) at the 500 mb and 1000 mb surfaces as shown in Fig. 16. The striking feature which can be seen at the 500 mb level (top figure) is the existence of a large direct (Hadley) circulation cell in the subtropical regions. Both models exhibit this property although the cell is somewhat more intense for Model Q. The strong convergence area located at about 15 degrees north latitude which drives this cell represents the large scale properties of the equatorial trough or Intertropical Convergence Zone (ITCZ) observed (in the mean) at this position under present day July conditions (see, for example, Riehl, 1965). The northern terminus of the cell lies over the belt of subtropical high pressure systems centered at 30 degrees north latitude and correlates well with currently observed mean July data as can be seen in Fig. 10, especially with reference to the 750 mb analyses. North of the subtropical Hadley cell extending to about 50 degrees both models exhibit a weaker indirect (Ferrel) meridional circulation. Farther to the north, but still imbedded within the mid-latitude westerly wind zone (Fig. 15), a much weaker and possibly quantitatively insignificant direct cell is observed which has to be maintained by surface friction (Flohn, 1969). Hence it is not surprising, because of the difference in the topography of Model Q in combination with a modified wind field in the area of this small direct cell, that some differences are noted in comparison with Model P. As mentioned above, however, the importance of this variation is possibly insignificant and will not be stressed here. Looking at the 1000 mb vertical

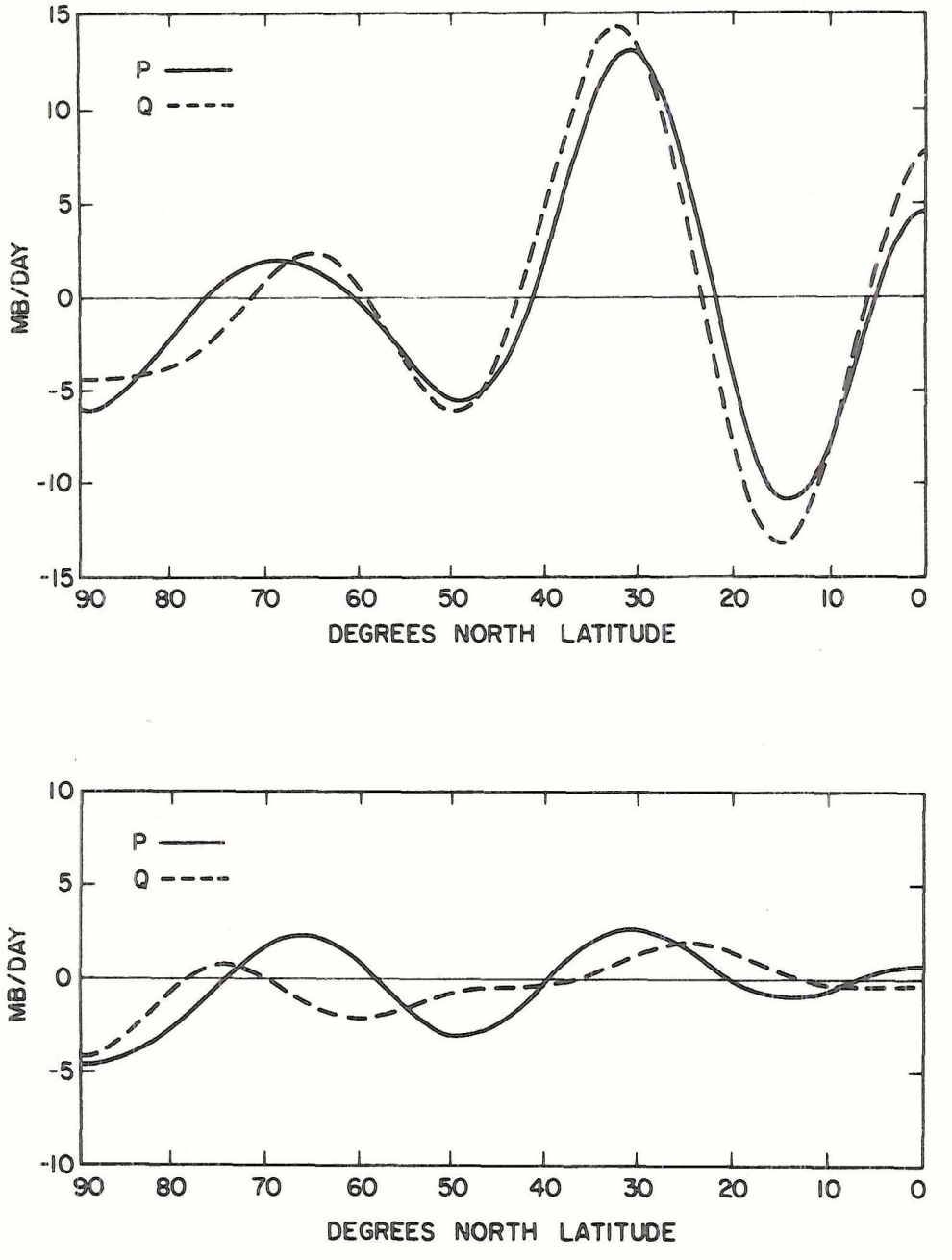

FIGURE 16. Vertical pressure velocity (ω) zonal profiles at the 500 mb (above) and 1000 mb (below) levels. Model P profiles are represented by solid lines; Model Q by dashed lines. Units are in mb/day. Data represents 30 day averages over the basic climate period (days 15 - 45).

pressure velocity curves of Fig. 16 (bottom figure) we note that the Model P values, while small, generally support the profile aloft. However, such support from the 1000 mb level for Model Q does not exist and probably is the main factor accounting for the small differences in the two 500 mb profiles. Since the 1000 mb vertical pressure velocities are completely determined through the action of the assumed surface nondivergent part of the wind field upon the orography (20), such differences in the 1000 mb vertical velocity profiles are not unexpected in view of the variations in these conditions.

A final discussion of prime importance to the generation of the model solutions concerns the diabatic heating which represents the model forcing. Figure 17 depicts zonal profiles of the 30 day climate averages for the total diabatic heating (heavy solid line) and the various component heating terms (for definitions of these quantities, see Chapter II, section F). All values are represented at level 2 (500 mb). It should be noted that the sensible heating curves include the effects of convective adjustment as outlined in Chapter II, section G. As is apparent from the two sets of curves, the diabatic heating quantities are relatively comparable except in the latitude belt containing areas of glaciation and pack ice during the Quaternary period. Here, as can be expected, the presence of the relatively cold underlying ice in Model Q served to inhibit the upward transports of sensible heat as well as latent heat release through condensation processes. Thus, as depicted in Fig. 17, we see that between 50 and 75 degrees north latitude, the total diabatic heating in Model Q is substantially reduced compared to that of Model P. This leads to a steeper north-south temperature gradient between the subtropics and the mid-latitudes

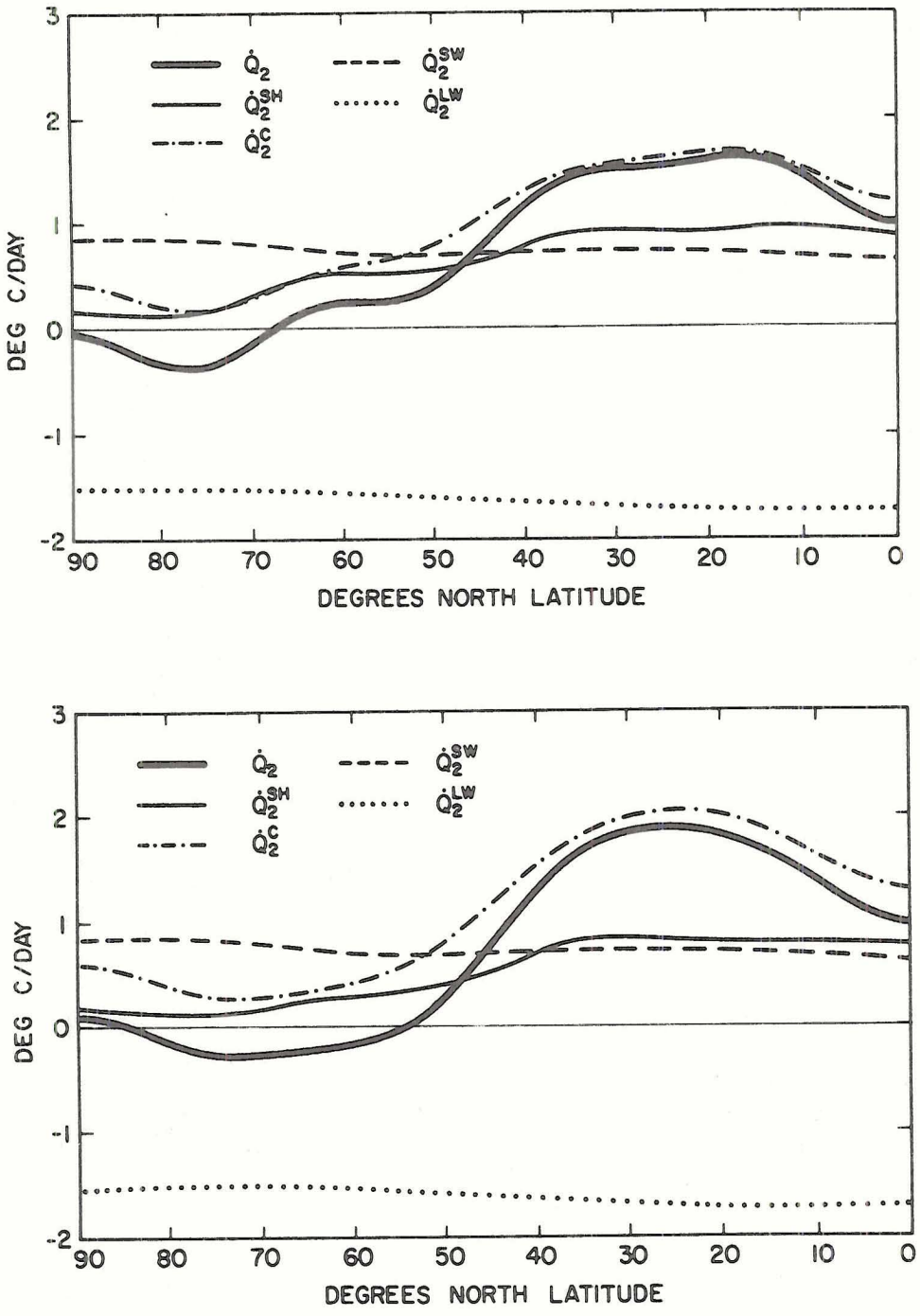

FIGURE 17. Diabatic heating terms averaged over the 30 day basic climate period at level 2 (500 mb) for Model P (above) and Model Q (below). For definitions of the individual quantities, see Chapter II, section F. The total diabatic heating is represented by the heavy solid line. Units are degrees C of temperature change per day.

during the ice age in the region of the indirect Ferrel cell (Fig. 16) usually associated with eddy transport processes. At least part of the increase in the level of eddy kinetic energy of Model Q as compared to Model P noted in Figs. 13 and 14 may be accounted for as a reaction to these gradients.

B. Climatological manifestations

In order to describe and compare the climatological general circulation patterns obtained from our model calculations, we have chosen to represent 30 day (days 15 - 45) average height contours along the 250 mb and 750 mb constant pressure surfaces. Selection of this representation was made because the heights are computed from the quasi-geostrophic balance condition (3) which provides the essential link between the dynamic and thermodynamic properties of our model. Thus, the major elements of the large scale manifestations of both the wind and temperature fields are contained in the analyses. Fig. 18 depicts the 250 mb height data from the climate solutions of both Model P and Model Q. The corresponding 750 mb analyses are contained in Fig. 19. In both figures Model P quantities are described in the top analyses while results from Model Q are shown below.

Although, as previously mentioned, differences between the results of the two calculations rather than their absolute values are to be stressed some discussion comparing the climatological data of Model P (upper parts of Figs. 18 and 19) with the present day observed July climate, represented by Fig. 10, is warranted. From these figures we see that while the details of the contour patterns of Model P differ somewhat from the observed data, many of the gross circulation features

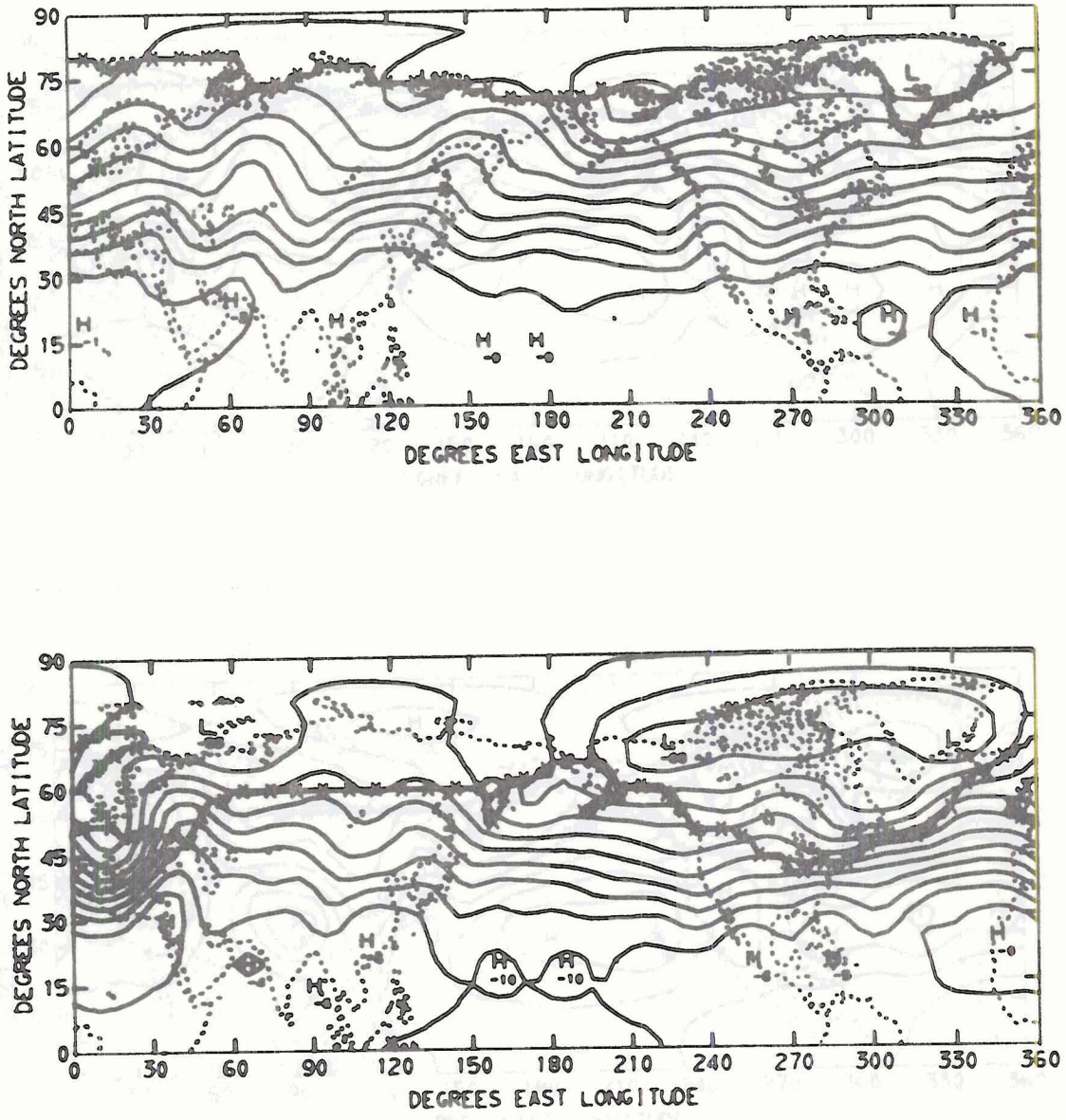

FIGURE 18. 250 mb height fields obtained from the 30 day climate solutions for Model P (above) and Model Q (below). Contour intervals are 6 dkm.

are comparable. For example, the essentially zonal flow patterns in the mid-latitudes contained in the observations are also apparent in Model P although slightly more diffuse in character. This feature is especially notable at the 250 mb level. At the 750 mb level we see that the subtropical high pressure belt stretching across the central Pacific and Atlantic Oceans at about 30 degrees north latitude has been reproduced by Model P. However, a major limitation in our model is its inability to represent the observed circulation pattern over south-central Asia. This can undoubtedly be attributed to the existence of the large high level (approximately 200 mb) heat source contained in the observed July data located over the Tibetian Plateau (see Fig. 5). We have not accounted for this source in our model because of the uncertainties as to the physical mechanisms which maintain it and some question therefore arises as to whether or not it was present during the Quaternary ice age.

We turn now to a comparison of the climate results as obtained from the two models (Figs. 18 and 19). Over eastern North America and across the North Atlantic we note a decided packing of the isohypses of Model Q, particularily along the southernmost and southeastern edges of the large continental ice sheet centered on Hudson Bay and in the region of the margin of Atlantic pack ice. Hence, the wind flow pattern during the Quaternary can be presumed to have had a strong preference for skirting the edges of ice in these areas. The existence of this converging of the wind field has previously been anticipated in the discussion of the zonal wind profiles contained in Fig. 15. It is interesting to note that Lamb and Woodroffe (1970, Fig. 7a) arrived at a somewhat similar representation for the Quaternary

ice age maximum over eastern North America and the North Atlantic using an entirely different approach. Their purely diagnostic study concentrated upon the establishing of surface temperatures from geological evidence of the limits of ice and snow regimes and the northern extents of different types of forests where approximate temperature values can be assigned from those associated with similar positions today. Ocean temperatures were approximated in a manner like that used in the present study (see Chapter III, section B). From these data vertical temperature lapse rates were devised according to the type of underlying surface and assumed air flow patterns with a strong reliance upon comparable situations in the world as it is today. The results are shown in the form of a probable monthly mean 1000-500 mb thickness chart and, as mentioned above, compare favorably with the Model Q analyses of Figs. 18 and 19 in eastern North America and over the north Atlantic along the ice edges. However, Lamb and Woodroffe were unable to account, to a large extent, for the dynamic effects of the glacial orography. Thus, for example, while they have placed the center of the circumpolar vortex over north central Canada, the results from Model Q indicate the probability of a slight high pressure ridge in this area due to the topography of the underlying glacier and consequently shifts the circumpolar vortex center to a position just south of Greenland. This feature is especially prominant at the 750 mb level (Fig. 19).

Probably the most striking difference between the two model climates is to be seen in Europe. Here the contour pattern of Model Q describes a large trough south of the Scandinavian glacier maximum coupled with a sharp ridge to the east over the eastern glacial downslopes. No

such features are observable in the Model P results. Since this trough/ridge system extends strongly through the depth of our model atmosphere and if it is to be believed representative of actual conditions which might have occurred during the Quaternary glacial maximum, we must look for some geological indications of its presence at the surface. Such an indication appears to be present in the wind data of Poser (1948) obtained from the bedding of sand dunes in central Europe during the later part of the Würm Ice Age. This data has been reinterpreted by Reiter (1963, Fig. 7.42) to include the effect of surface friction in order to obtain a more realistic picture of the surface pressure distribution. While this new pressure pattern is by no means conclusive, the indication is that a mean surface low pressure trough must have existed in the vicinity of southern Europe. In any event, assuming the surface wind data of Poser to be correct, the wind vectors show that westerly air currents entering the European continent along the northern coast of present day France turn abruptly southward in the vicinity of eastern Germany and western Poland much as would be expected from the 750 mb height contours of Model Q.

While the climatological solutions shown in Figs. 18 and 19 represent the standing patterns generated by Model P and Model Q, the presence of traveling waves representative of cyclone scale activity have been essentially eliminated. In order to obtain a quantitative picture of this cyclone activity for the two models and thus infer probable positions for the major storm tracks, we have constructed an activity index for the 30 day climate periods in question. The index values were obtained by computing absolute height differences at five degree grid intervals for each 6 hour period between days

15 and 45. Average quantities for each grid point over the 30 day time period were then obtained and analysed as shown in Fig. 20 for the 250 mb level and Fig. 21 for 750 mb. As in previous figures, data for Model P is presented in the top part of each figure with Model Q values below. Contour intervals are 10m/6 hr. It is apparent from the figures that the transient activity in Model P is considerably less than that of Model Q across the northern Atlantic and in the regions of south central to eastern Europe. These differences are noted at both levels of our two models. Thus it would appear that for these regions the combination of cyclone scale activity along with strong support from the height gradients observed for Model Q in the standing wave patterns (Figs. 18 and 19) would have a profound effect upon the climates of the Quaternary ice age.

Although we have limited our analysis to differences between the two model solutions, the temptation to infer a probable climatic general circulation for the Quaternary ice age is overwhelming. If we assume that the physical and mathematical limitations inherent in our model exhibit similar properties in the calculations for both Model P and Model Q, then we can perhaps deduce the change in climate which has occurred over the past 18,000 years since the last Quaternary ice age maximum to a fairly high degree of reliability by subtracting the 30 day average Model Q results from those of Model P. This, of course, is predicated on the assumption that the forcing and surface boundary conditions used for both models are essentially correct. In this manner 250 mb and 750 mb height change fields representing changes in climate since the Quaternary period were constructed and then subtracted from the observed present day mean July height data shown in Fig. 10. The

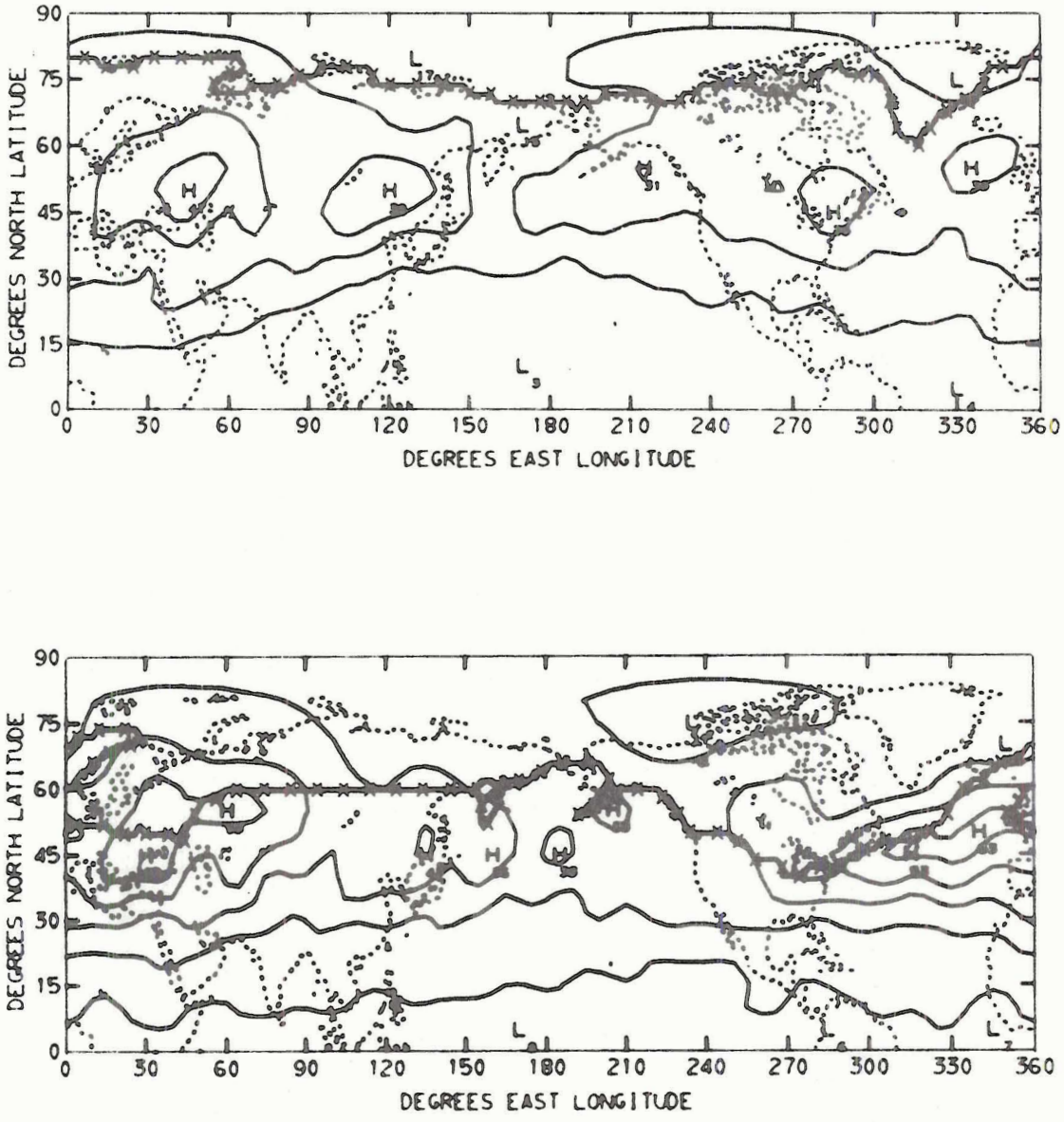

FIGURE 20. 250 mb absolute height changes per 6 hours averaged over the 30 day basic climate period for Model P (above) and Model Q (below). Contour intervals are 10m/6 hr.

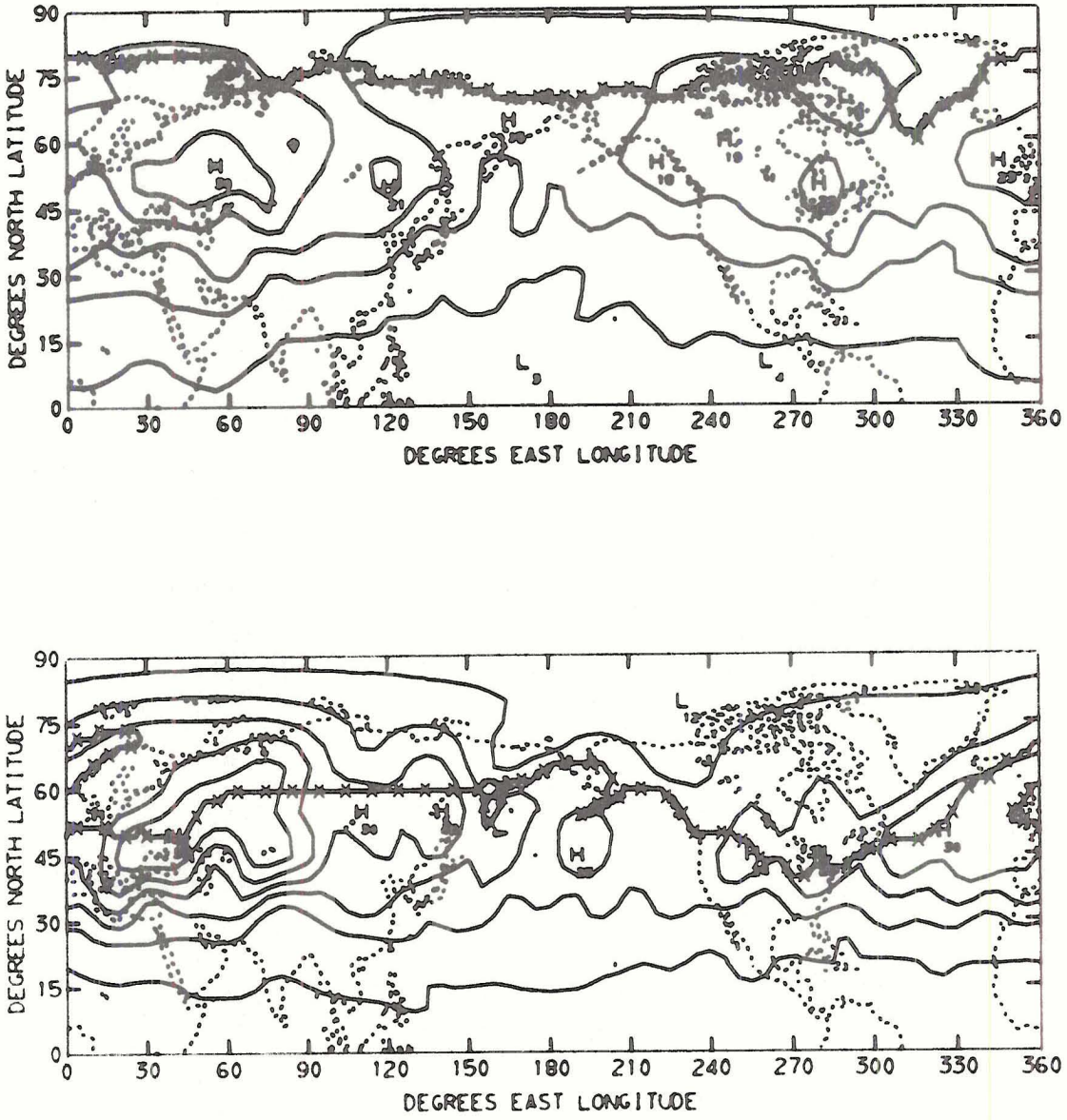

FIGURE 21. 750 mb absolute height changes per 6 hours averaged over the 30 day basic climate period for Model P (above) and Model Q (below). Contour intervals are 5m/6 hr.

resulting probable Quaternary general circulation height fields for both the 250 mb (top) and 750 mb (bottom) levels are shown in Fig. 22. Whether these analyses are more representative of actual ice age conditions than the Model Q climate solutions shown in Figs. 18 and 19 is strictly a matter of conjecture. However, since Fig. 22 was constructed using the differences between the climate solutions for Model P and Model Q, all discussions above concerning these differences remain valid. Thus, in comparing the July climate as it might have been during Quaternary glaciation as obtained in the present study with that of the same month today, the reader is free to choose either a combination of Figs. 22 and 10 or Figs. 18 and 19.

It is not difficult to imagine, using either Fig. 22 or the Model Q climate solutions from Figs. 18 and 19, some of the effects of the Quaternary ice age climate, as derived in the present study, upon the glacial pattern of Europe and Asia. As can be seen from Figs. 20 and 21 a large number of cyclone scale waves under the influence of the strong steering currents over the north Atlantic were driven upon the Scandinavian ice shield laden with moisture picked up from the ocean. Supported by orographic influences and stalled by the hugh blocking high over central Russia, abundant precipitation could then be obtained to maintain the Scandinavian glacier. On the other hand, this same blocking high pressure ridge, coupled with the severe continentality of Siberian Asia, served to deny the requisite moisture for glaciation in Siberia. In North America, however, maintenance of continental glaciation centered on Hudson Bay is not so easily explained from the results shown. The small pressure ridge indicated over the huge North American ice shield could only serve to diffuse the relative small number of travelling

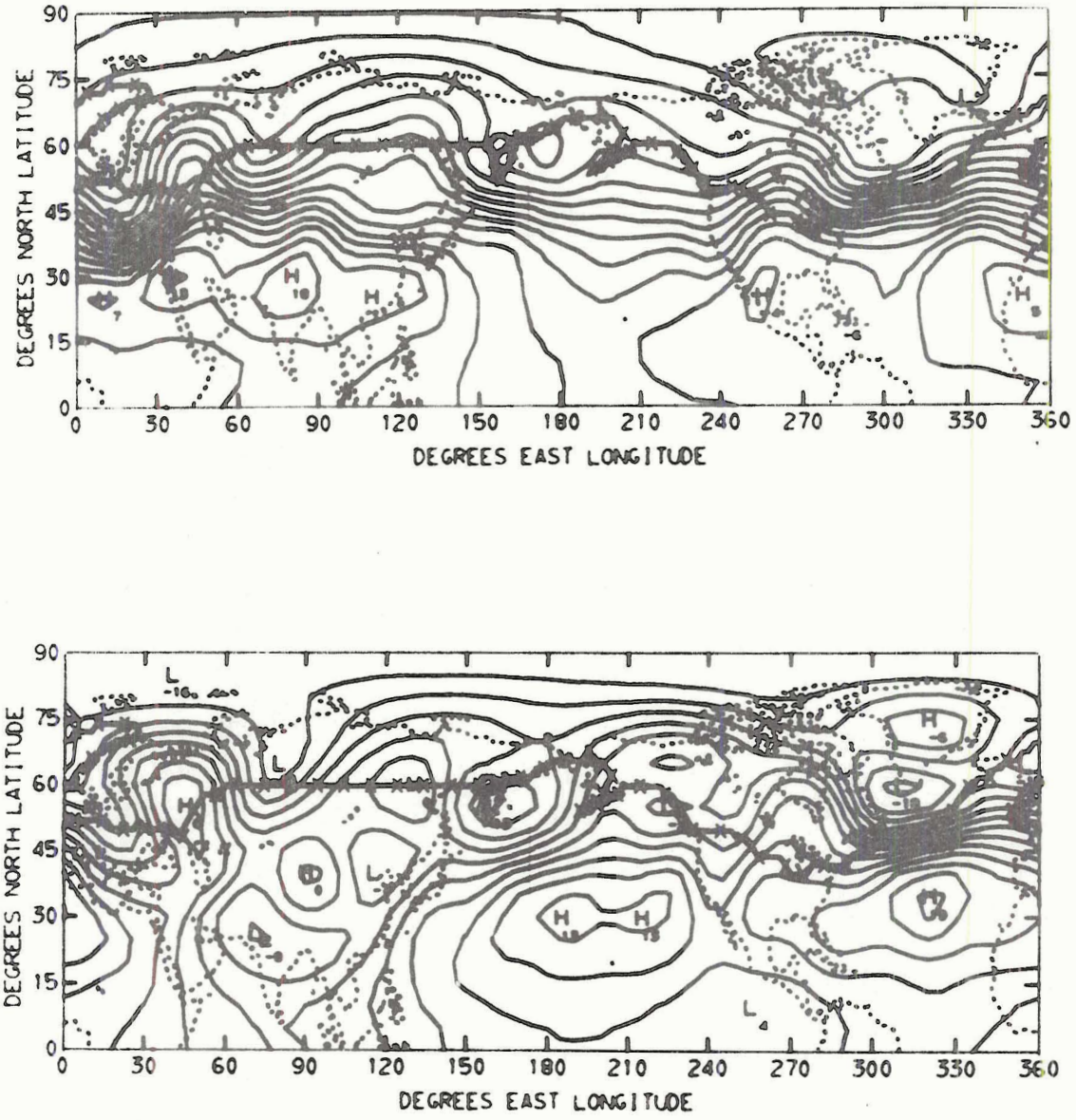

FIGURE 22. Probable Quaternary ice age height contours representing mean July conditions (see text for explanation). 250 mb analysis (above) uses 6 dkm contour intervals while the 750 mb analysis (below) is drawn with 3 dkm contour intervals.

waves (Figs. 20 and 21) carrying Pacific moisture onto the continent, although maintenance of the glacier no doubt benefited somewhat from orographic lifting. However, it is felt here that much of the available moisture may have already been squeezed out by the Rocky Mountain cordillera prior to its arrival over the glacier area. It may have been possible that the winter time circulation was able to supply enough moisture to maintain the glacier. The possiblity also arises that this large glacier had already attained its maximum size long before the period of our study and was on the decline 18,000 years ago. If we assume this second possibility to have been the case then the orographic effects of the North American ice shield would gradually be reduced thus allowing the center of the circumpolar vortex to shift westward to a position over northern Canada as shown by Lamb and Woodroffe (1970, Fig. 7a). A reduction in the intensity of the flow field across the North Atlantic can then be assumed and, consequently, support for the maintenance of the Scandinavian glacial field would decrease. While this discussion concerning maintenance of the two great northern hemisphere ice sheets is completely speculative, its purpose is to raise the possibility that these glaciers may not have generated atmospheric conditions of mutual support and that a time lag in the occurrence of their respective maximums may have been present.

V. SUMMARY AND CONCLUSIONS

In an effort to simulate the climate of an ice age, a two-level, quasi-geostrophic general circulation model for the northern hemisphere was developed suitable for long time period integrations (60 days). The model incorporates horizontal diffusion and vertical shearing stresses along with a diabatic heating function which includes the effects of radiation, horizontal and vertical heat transfer and condensation heating. Orographic influences as well as land-sea-ice distributions of heating are represented at the lower boundary. The model was cast in the "spectral" domain and all time integrations carried out using a centered difference (leapfrog) scheme.

In order to obtain a bench mark for comparison, the model was first integrated forward in time for a total of sixty days under conditions simulating a current mean July situation (Model P). Initial free atmospheric and boundary value data were obtained from conventional sources. A second integration of similar duration was then performed to simulate the climatology during the last great ice age maximum (Wisconsin/Würm) of the Quaternary period (Model Q), some 18,000 years ago. For this calculation the same initial free atmospheric state as used for Model P was assumed. However, surface boundary values had to be established from a variety of paleogeologic sources. Statistical climate values were then calculated for each model over the 30 day period from day 15 through day 45.

The results of the calculations showed that the kinetic energy levels computed for the ice age period were about 40% larger than those obtained under present day conditions. However, little difference was noted in the zonal kinetic energy levels as nearly all of the

increased dynamic activity of Model Q was confined to the eddies. An increase in the north-south temperature gradients of Model Q as compared to Model P was observed in the region of the mid-latitude eddy transport regime. This was attributed to the approximately .2C per day lower diabatic heating of the model atmosphere over the glaciated areas in Model Q (see Fig. 17).

The climate solutions of the two models as represented by 250 mb and 750 mb height fields (Figs. 18 and 19) contoured over the northern hemisphere showed a deviation between the two models in the mid-latitudes, principally in the regions of heavy Quaternary glaciation and Atlantic pack ice. For example, the latitudinal belt from about 40 to 75 degrees north latitude and from central North America eastward across the northern Atlantic and into western Siberia exhibited a marked climatic influence generated by the presence of the ice fields of the Quateranry model. In North America this was evident by the appearance of a small orographically induced high pressure ridge over the Hudson Bay glacial maximum while the center of the circumpolar vortex was located off the southern tip of Greenland. Strong height gradients occurred along the southern edge of the North Atlantic pack ice and, in Europe, a large low pressure trough could be found south of the Scandinavian glacial maximum with a strong blocking high to the east.

Of course the results of any experiment utilizing a numerical model to simulate climate conditions must be interpreted according to the limitations of the model used. Major uncertainties arise from the use of parameterized quantities in place of physical concepts and through inadequate specification of boundary and initial values. In this regard the present model is no exception. A principle limitation here concerns the specification of the model forcing through the diabatic heating functions. For

REFERENCES

Baer, F., 1964: Integration with the spectral vorticity equation. J. Atmos. Sci., 21, 260-276.

Baer, F., and F. N. Alyea, 1971: Effects of spectral truncation on general circulation and long-range prediction. J. Atmos. Sci., 28 457-480.

Baer, F. and G. W. Platzman, 1961: A procedure for numerical integration of the spectral vorticity equation. J. Meteor., 18, 393-401.

Baer, F. and T. J. Simons, 1970: Computational stability and time truncation of coupled solutions. Mon. Wea. Rev., 98, 665-679.

Charney, J. G., 1959: On the theory of the general circulation of the atmosphere. The Atmosphere and the Sea in Motion, New York, The Rockefeller Institute Press, 178-193.

Cox, A., 1968: Polar wandering, continental drift, and the onset of Quaternary glaciation. Meteorological Monographs--Causes of Climatic Change, Vol. 8, No. 30. Boston, The American Meteorological Society, 112-125.

Crutcher, H. L. and J. M. Meserve, 1970: Selected Level Heights, Temperatures and Dew Points for the Northern Hemisphere. U. S. Government Printing Office, Washington D. C., 10 pp. plus charts.

Davis, P. A., 1963: An analysis of the atmospheric heat budget. J. Atmos. Sci., 20, 5-22.

Deardorff, James. W., 1966: The counter-gradient heat flux in the lower atmosphere and in the laboratory. J. Atmos. Sci., 23, 503-506.

Elsaesser, H. W., 1966a: Evaluation of spectral versus grid methods of hemispheric numerical weather prediction. J. Appl. Meteor., 5, 246-262.

Elsaesser, H. W., 1966b: Expansion of hemispheric meteorological data in antisymmetric surface spherical harmonic (Laplace) series. J. Appl. Meteor., 5, 263-276.

Emiliani, C., 1955: Pleistocene temperatures. Jour. of Geology, 63, 538-578.

Emiliani, C., 1958: Ancient temperatures. Scientific American, Feb., 11 pp.

Emiliani, C., 1966: Isotopic paleotemperatures. Science, 154, 851-857.

Emiliani, C., 1970: Pleistocene paleotemperatures. Science, 168, 822-825.

Fletcher, J. O., 1965: The heat budget of the artic basin and its relation to climate. A report prepared for U. S. Air Force project RAND (R-444-PR), The Rand Corporation, Santa Monica, Calif., pp. 70-75.

Flint, R. F., 1957: Glacial and Pleistocene Geology. Wiley, New York, 553 pp.

Flohn, H., 1969: Climate and Weather. World University Library, McGraw-Hill, New York, 253 pp.

Gray, William M., 1968: Global view of the origin of tropical disturbances and storms. Mon. Wea. Rev., 96, 669-700.

Gutenberg, B., 1954: Postglacial uplift in the Great Lakes region. Arch. für Meteorol. Geophysik u. Bioklimatol., ser. A, Meteorol. u. Geophysik., 7, 243-251.

Jahnke, E. and F. Emde, 1945: Tables of Functions. Dover, New York, 306 pp. plus tables.

Kasahara, A., and W. M. Washington, 1967: NCAR glocal general circulation model of the atmosphere. Mon. Wea. Rev., 95, 389-402.

Kasahara, A. and W. M. Washington, 1971: General circulation experiments with a six-layer NCAR model, including orography, cloudiness and surface temperature calculations. J. Atmos. Sci., 28, 657-701.

Kikuchi, Y., 1969: Numerical simulation of the blocking process. J. Meteor. Soc. Japan, 47, 29-54.

Lamb, H. H., 1961: Fundamentals of climate. In Descriptive Paleoclimatology, Ed. A. E. M. Nairn, New York, Interscience Publishers, 8-44.

Lamb, H. H. and A. Woodroffe, 1970: Atmospheric circulation during the last ice age. Quaternary Res., 1, 29-58.

Leith, C. E., 1965: Numerical simulation of the earth's atmosphere. Methods in Computation Physics, Vol. 4, Application in Hydrodynamics. New York, Academic Press, 1-28.

London, J., 1957: A study of the atmospheric heat balance. Final report on contract AF 19(122)-165 (AFCRC-TR-57-287), Dept. of Meteorology and Oceanography, New York University, 99 pp.

London, J. and T. Sasamori, 1971: Radiative energy budget of the atmosphere. Space Research XI, Vol. 1, Berlin, Akademic-Verlag, 639-649.

Lorenz, E. N., 1960: Energy and numerical weather prediction. Tellus, 12, 364-373.

Lorenz, E. N., 1964: The problem of deducing the climate from the governing equations. Tellus, 16, 1-11.

Lorenz, E. N., 1967: The Nature and Theory of the General Circulation of the Atmosphere. World Meteorological Organization, 161 pp.

Lorenz, E. N., 1968: Climatic Determinism. Meteorological Monographs--Causes of Climatic Change, Vol. 8, No. 30, Boston, The American Meteorological Society, 1-3.

MacCracken, M. C., 1968: Ice age theory analysis by computer model simulation. Ph.D. dissertation, University of California, Davis, 193 pp.

Machenhauer, B. and E. Rasmussen, 1972: On the integration of the spectral hydrodynamical equations by a transform method. Report No. 3, Institut for Teoretisk Meteorologi, KØBENHAVNS Universitet, 44 pp.

Manabe, S., J. Smagorinsky and R. F. Strickler, 1965: Simulated climatology of a general circulation model with a hydrologic cycle. Mon. Wea. Rev., 93, 769-798.

Merilees, P. E., 1968: The equations of motion in spectral form. J. Atmos. Sci., 25, 736-743.

Mintz, Y., 1964: Very long-term global integration of the primitive equations of atmospheric motion. Proc. WMO/IUGG Symposium on Res. and Dev. Aspects of Long-Range Forecasting (U.C.L.A. Dept. of Meteorology Contribution No.111), 37 pp.

Mintz, Y., 1968: Very long-term global integration of the primitive equations of atmospheric motion: an experiment in climate simulation. Meteorological Monographs--Causes of Climatic Change, Vol. 8, No. 30. Boston, The American Meteorological Society, 20-36.

Orszag, Steven A., 1970: Accuracy of numerical simulation of incompressible flows. NCAR Manuscript No. 70-73, National Center for Atmospheric Research, Boulder, Colorado, 43 pp. plus 28 figures.

Paterson, W. S. B., 1969: The Physics of Glaciers. Pergamon, New York, 250 pp.

Phillips, N. A., 1956: The general circulation of the atmosphere: A numerical experiment. Quart. J. Roy. Meteor. Soc., 82, 123-164.

Platzman, G. W., 1960: The spectral form of the vorticity equation. J. Meteor., 17, 635-644.

Poser, H., 1948: Boden und Klimaverhältnisse in Mittel- und Westeuropa während der Wurm-Eiszeit. Erdke., 2.

Reiter, E. R., 1963: Jet-stream Meteorology. University of Chicago Press, Chicago, 515 pp.

Riehl, H., 1965: Introduction to the Atmosphere. McGraw-Hill, New York, 365 pp.

Riehl, H. and J. S. Malkus, 1958: On the heat balance in the equatorial trough zone. Geophysica, 6, 503-538.

Robert, A. J., 1966: The integration of a low order spectral form of the primitive meteorological equations. J. Meteor. Soc. Japan, 44, 237-245.

Rosholt, J. N., C. Emiliani, J. Geiss, F. F. Koczy, and P. J. Wangersky, 1962: Pa^{231}/Th^{230} dating and O^{18}/O^{16} temperature analysis of core A254-BR-C. J. Geophy. Res., 67, 2907-2911.

Sasamori, T., 1968: The radiative cooling calculation for application to general circulation experiments. J. Appl. Meteor., 7, 721-729.

Schwarzbach, M., 1963: Climates of the Past. D. Van Nostrand Co., Ltd., New York, 328 pp.

Sellers, W. D., 1965: Physical Climatology. University of Chicago Press, 272 pp.

Simpson, G. C., 1959: World temperatures during the Pleistocene. Quart. J. Roy. Meteor. Soc., 85, 332-349.

Smagorinsky, J., 1963: General circulation experiments with the primitive equations. Mon. Wea. Rev., 91, 99-164.

Smagorinsky, J., S. Manabe and J. L. Holloway, Jr., 1965: Numerical results from a nine-level general circulation model. Mon. Wea. Rev., 93, 727-768.

Urey, H. C., 1947: The thermodynamic properties of isotopic substances. Jour. Chem. Soc., 1947, 562-581.

Vonder Haar, T. H., 1968: Variations of the earth's radiation budget. Meteorological Satellite Instrumentation and Data Processing. Final scientific report (1958-1968), Dept. of Meteorology, The University of Wisconsin, Madison, 31-107.

Vonder Haar, T. H. and K. J. Hanson, 1969: Absorption of solar radiation in tropical regions. J. Atmos. Sci., 26, 652-655.

Washington, W. M. and A. Kasahara, 1970: A January simulation experiment with the two-layer version of the NCAR global circulation model. Mon. Wea. Rev., 98, 559-580.

Young, David, 1962: The numerical solution of elliptic and parabolic partial differential equations. Survey of Numerical Analysis, New York, McGraw-Hill Book Co., Inc., 380-438.

APPENDIX A

MODEL CONSTANTS

1. Dynamic constants

$A = 2/3$

$A_{MH} = 10^5 \text{ m}^2 \text{ s}^{-1}$

$A_{MV} = 5 \times 10^{-7} \text{ s}^{-1}$

$A_{MVS} = 4 \times 10^{-6} \text{ s}^{-1}$

$g = 9.8 \text{ m s}^{-2}$

2. Thermodynamic constants

$C_p = 0.240 \text{ cal g}^{-1} \text{ K}^{-1}$

$R = 6.8557 \times 10^{-2} \text{ cal g}^{-1} \text{ K}^{-1}$

$\kappa = R/C_p = 0.2857$

$\rho_s = 1.2 \times 10^3 \text{ g m}^{-3}$

Surface albedoes

$\alpha_s\big)_{\text{land}} = 0.15$

$\alpha_s\big)_{\text{ice}} = 0.60$

σ (Stefan's constant) $= 5.673 \times 10^{-5} \text{ ergs cm}^{-2} \text{ s}^{-1} \text{ K}^{-4}$

$e_o = 6.11 \text{ mb}$

$L_{\ell v} = 2500 \text{ joules g}^{-1}$

$R_v = .461 \text{ joules g}^{-1} \text{ K}^{-1}$

$T_s = 277.31 \text{ K}$

$T_o = 273.16 \text{ K}$

$A_{TH} = A_{MH} = 10^5 \text{ m}^2 \text{ s}^{-1}$

$A_{TV} = A_{MV} = 5 \times 10^{-7} \text{ s}^{-1}$

$A_{TVS} = A_{MVS} = 4 \times 10^{-6}\ s^{-1}$

$\gamma_{CG} = 10^{-5}\ K\ cm^{-1}$

$\gamma_{CGS} = 5 \times 10^{-5}\ K\ cm^{-1}$

$B = 1$ (land)

$a_T = -781.49\ kg\ s^{-3}$

$b_T = 4.0768\ kg\ s^{-3}\ K^{-1}$

APPENDIX B

COMPUTATION OF THE NET LW RADIATION FLUXES

If we assume that above the 250 mb level the path length of each absorbing gas changes very little then from Sasamori (1968) we can write for the net downward and upward LW radiation fluxes

$$F\downarrow(p) = \begin{cases} 0 \text{ for } p < 250 \text{ mb} \\ 4\sigma \int_{T(p_{250})}^{T(p)} \bar{\bar{A}}_o \{u(T') - u[T(p)]\} T'^3 \, dT' + \\ + \sigma T^4(p_{250}) \, \bar{\bar{A}} \{u[T(p_{125})] - u[T(p)], T(p_{250})\} \\ \text{for } p \geq 250 \text{ mb} \end{cases} \tag{B-1}$$

and

$$F\uparrow(p) = \sigma T^4(p_{1000}) + \begin{cases} 4\sigma \int_{T(p_{1000})}^{T(p)} \bar{\bar{A}}_o \{u[T(p)] - u(T')\} T'^3 \, dT' \\ \text{for } p \geq 250 \text{ mb} \\ 4\sigma \int_{T(p_{1000})}^{T(p_{250})} \bar{\bar{A}}_o \{u[T(p_{250})] - u(T')\} T'^3 \, dT' - \\ - \sigma T^4(p_{250}) \, \bar{\bar{A}} \{u[T(p)] - u[T(p_{125})], T(p_{250})\} \\ \text{for } p < 250 \text{ mb} \end{cases} \tag{B-2}$$

where u represents the path length of the absorbing gas. The values of u for carbon dioxide and water vapor are given by equations (39) and (44). Empirical formulas for the absorption functions $\bar{A}_o(u)$ and $\bar{\bar{A}}(u, T)$ are presented by Sasamori and we will in general adopt his values. For water vapor we take

$$\left.\begin{aligned} \bar{A}_o(u_w) &= 0.240 \log_{10} (u_w + 0.005) + 0.622 \\ \bar{\bar{A}}(u_w, T) &= 8.34T^{(0.335 \log_{10} u_w - 0.44)} \times \\ &\quad \times u_w^{(-0.03455 \log_{10} u_w - 0.705)} \end{aligned}\right\} \quad . \qquad \text{(B-3)}$$

The empirical formulas for carbon dioxide are given as

$$\bar{A}_o(u_c) = \begin{cases} 0.0675 \ (u_c + 0.01022)^{0.421} - 0.00982 \\ \qquad \text{for } u_c \leq 1 \text{ cm} \\ 0.0546 \log_{10} u_c + 0.0581 \\ \qquad \text{for } u_c > 1 \text{ cm} \end{cases} \qquad \text{(B-4)}$$

and

$$\bar{\bar{A}}(u_c) = \begin{cases} 0.0825 \ u_c^{0.456} \quad \text{for } u_c \leq 0.5 \text{ cm} \\ 0.0461 \log_{10} u_c + 0.074 \\ \qquad \text{for } u_c > 0.5 \text{ cm} \end{cases} \quad . \qquad \text{(B-5)}$$

In order to evaluate the net LW flux passing through the required levels of 0 mb, 500 mb, and 1000 mb we will perform the integrations indicated in (B-1) and (B-2) through a number of layers assuming a constant value in each layer for the absorbtion function $\bar{A}_o(u)$. For this purpose we will use the absorption path length at the center of the layer. From (35) we know that the net flux is given by

$$F_N(p) = F\uparrow(p) - F\downarrow(p) \tag{B-6}$$

and thus we have, approximately,

$$\left.\begin{aligned}
F_N(p_0) &= \sigma T_{1000}^4 + \sigma(T_{750}^4 - T_{1000}^4)\,\bar{A}_o(u_{250} - u_{875}) \\
&\quad + \sigma(T_{500}^4 - T_{750}^4)\,\bar{A}_o\,(u_{250} - u_{625}) \\
&\quad + \sigma(T_{250}^4 - T_{500}^4)\,\bar{A}_o\,(u_{250} - u_{375}) \\
&\quad - \sigma T_{250}^4\,\bar{\bar{A}}\,[u_o - u_{125},\ T(p_{250})] \\
F_N(p_{500}) &= \sigma T_{1000}^4 + \sigma(T_{750}^4 - T_{1000}^4)\,\bar{A}_o(u_{500} - u_{875}) \\
&\quad + \sigma(T_{500}^4 - T_{750}^4)\,\bar{A}_o\,(u_{500} - u_{625}) \\
&\quad - \sigma(T_{500}^4 - T_{250}^4)\,\bar{A}_o\,(u_{375} - u_{500}) \\
&\quad - \sigma T_{250}^4\,\bar{\bar{A}}\,[u_{125} - u_{500},\ T(p_{250})] \\
F_N(p_{1000}) &= \sigma T_{1000}^4 - \sigma(T_{500}^4 - T_{250}^4)\,\bar{A}_o(u_{375} - u_{1000}) \\
&\quad - \sigma(T_{750}^4 - T_{500}^4)\,\bar{A}_o(u_{625} - u_{1000}) \\
&\quad - \sigma(T_{1000}^4 - T_{750}^4)\,\bar{A}_o(u_{875} - u_{1000}) \\
&\quad - \sigma T_{250}^4\,\bar{\bar{A}}\,[u_{125} - u_{1000},\ T(p_{250})]
\end{aligned}\right\} \tag{B-7}$$

The temperature factors in (B-7) are linearized using the relationship

$$\sigma T^4 = a_T + b_T T \tag{B-8}$$

where a_T and b_T have been established through a least squares fit over the temperature range from 210K to 310K. Letting σ (Stefan's

constant) equal 5.673×10^{-8} kg s^{-3} K^{-4} we get

$$a_T \tilde{=} -781.49 \text{ kg } s^{-3}$$

and

$$b_T \tilde{=} 4.0768 \text{ kg } s^{-3} K^{-1} \quad .$$

Now, from (45) we know that the rates of diabatic heating due to LW radiation and absorption at levels 1 and 3 are given by

$$\left.\begin{aligned} \dot{Q}_1^{LW} &= \frac{g}{p_2}[F_N(p_{500}) - F_N(p_0)] \\ \dot{Q}_3^{LW} &= \frac{g}{p_2}[F_N(p_{1000}) - F_N(p_{500})] \end{aligned}\right\} . \qquad \text{(B-9)}$$

Then using (B-8) to linearize (B-7) inserting the resulting relationships into (B-9), and writing in terms of potential temperatures we have

$$\left.\begin{aligned} \dot{Q}_1^{LW} &= A_0^{LW} + A_1^{LW}\theta_1 + A_3^{LW}\theta_3 + A_4^{LW}\theta_4 \\ \dot{Q}_3^{LW} &= B_0^{LW} + B_1^{LW}\theta_1 + B_3^{LW}\theta_3 + B_4^{LW}\theta_4 \end{aligned}\right\} \qquad \text{(B-10)}$$

where

$$\left.\begin{aligned} A_0^{LW} &= \frac{a_T\, g}{p_{500}}\ [\bar{\bar{A}}(u_o - u_{125}, T_{250}) - \bar{\bar{A}}(u_{125} - u_{500}, T_{250})] \\ A_1^{LW} &= \frac{b_T\, g}{p_{500}}\ \{\tfrac{1}{2}\left(\frac{p_{500}}{p_{1000}}\right)^{\kappa}[\bar{A}_o(u_{500} - u_{625}) - \bar{A}_o(u_{250} - u_{625})] \\ &\quad + \left[\left(\frac{p_{250}}{p_{1000}}\right)^{\kappa} - \tfrac{1}{2}\left(\frac{p_{500}}{p_{1000}}\right)^{\kappa}\right][\bar{A}_o(u_{375} - u_{500}) - \bar{A}_o(u_{250} - u_{375})] \\ &\quad + \left(\frac{p_{250}}{p_{1000}}\right)^{\kappa}[\bar{\bar{A}}(u_o - u_{125}, T_{250}) - \bar{\bar{A}}(u_{125} - u_{500}), T_{250}]\} \\ A_3^{LW} &= \frac{b_T\, g}{p_{500}}\ \{\left(\frac{p_{750}}{p_{1000}}\right)^{\kappa}[\bar{A}_o(u_{500} - u_{875}) - \bar{A}_o(u_{250} - u_{875})] \end{aligned}\right\}$$

In order to simplify computations involving the surface LW radiation flux term $F_4^{LW}\theta_4$ in (B-13), we write F_4^{LW} in the form

$$F_4^{LW} = F_4^{LWC} + F_4^{LWW} \tag{B-17}$$

where we will show that F_4^{LWC} is constant. To do this we consider the definition of F_4^{LW} in (B-14) along with (B-16). As an example let $\Delta u = u_{875} - u_{1000}$ such that we can represent F_4^{LW} as

$$F_4^{LW} = b_T[1 - \bar{A}_o(\Delta u_c) - \bar{A}_o(\Delta u_w)] \tag{B-18}$$

where then we let

$$\left.\begin{aligned} F_4^{LWC} &= b_T[1 - \bar{A}_o(\Delta u_c)] \\ F_4^{LWW} &= -b_T\bar{A}_o(\Delta u_w) \end{aligned}\right\} \quad . \tag{B-19}$$

However, since we have assumed for our model calculations that the mixing ratio of carbon dioxide in the atmosphere is constant (Chapter II, section F) we see that F_4^{LWW} in (B-19) and (B-17) is indeed a constant and only F_4^{LWW} is time and space dependent. Thus, we will use (B-17) along with definitions (B-19) for all future representations involving surface energy fluxes.

APPENDIX C

NONDIMENSIONALIZATION OF THE MODEL PARAMETERS

In order to nondimensionalize the model parameters we make use of the earth's mean radius (a), the earth's rotation rate (Ω), the specific heat of air at constant pressure (C_p) and the pressure depth of each of the model layers (p_2 = 500 mb). Letting primed (') quantities represent nondimensional values we can write for streamfunctions

$$\psi = a^2\Omega\psi' \tag{C-1}$$

and for potential temperatures

$$\theta = \frac{a^2\Omega^2}{C_p}\theta' \quad . \tag{C-2}$$

Time derivatives become

$$\frac{\partial}{\partial t} = \Omega \frac{\partial}{\partial t'} \quad . \tag{C-3}$$

All other quantities are treated in a similar manner. For example we define some representative parameters

$$\left.\begin{aligned} X_2 &= p_2\Omega a^2 X'_2 \\ \omega_1 &= p_2\Omega\omega'_1 \\ \dot{Q}_1 &= a^2\Omega^3\dot{Q}'_1 \\ L_1 &= \Omega L'_1 \\ L_3 &= \Omega L_3 \\ N_3 &= \frac{a^2\Omega^3}{C_p} N'_3 \end{aligned}\right\} \quad . \tag{C-4}$$

Also, we can define the nondimensional parameters A_s and B_s as

$$\left.\begin{aligned} A_s &= \frac{C_p}{a\Omega^2} A \frac{g}{R} \frac{p_4}{p_2} \\ B_s &= \frac{aAg\rho_s}{p_2} \end{aligned}\right\} \quad . \qquad \text{(C-5)}$$

APPENDIX D

TRANSFORMATION OF THE MODEL EQUATIONS TO SPECTRAL FORM

The process of spectral transformation has been described in detail elsewhere (see, for example, Baer and Platzman, 1961 and Merilees, 1968) and will only be given cursory treatment here. The general procedure is to substitute the expansions of the variables (77) into the equations and to perform all indicated differential operations. The equations are then multiplied by the complex conjugate of a given spherical harmonic and the result is then integrated over the unit sphere. Because of the orthogonality condition (78) most linear terms will yield a single expansion coefficient. However, certain special linear terms produce more than one of these coefficients. An example of this type of linear term is presented below. Nonlinear terms will transform into an infinite sum of the product of two coefficients modified by a wave vector dependent constant. These constants or "interaction coefficients" are computed in advance of the numerical calculation and held in tabular form.

For the purposes of our model calculations we have defined all nonlinear interactions as functions of two basic interaction coefficient sets. These are

$$\left.\begin{aligned} K_{\gamma,\beta,\alpha} &= \frac{1}{2}\int_{-1}^{1}\left(\ell_\beta P_\beta \frac{dP_\alpha}{d\mu} - \ell_\alpha P_\alpha \frac{dP_\beta}{d\mu}\right)P_\gamma\, d\mu \\ J_{\gamma,\beta,\alpha} &= \frac{1}{2}\int_{-1}^{1} P_\alpha P_\beta P_\gamma\, d\mu \end{aligned}\right\} \qquad (D\text{-}1)$$

where $\ell_\gamma = \ell_\alpha + \ell_\beta$ with the coefficients being zero otherwise. Certain other redundancy and symmetry properties associated with the interaction coefficients in (D-1) have been discussed by Baer and Platzman (1961) and Merilees (1968) and will not be treated here.

As examples of all of the types of nonlinear terms in the model equations which must be reduced to spectral form let us consider arbitrary variables A and B which can be expanded in the forms

$$\left.\begin{aligned} A &= \Sigma_\gamma A_\gamma Y_\gamma(\lambda, \mu) \\ B &= \Sigma_\gamma B_\gamma Y_\gamma(\lambda, \mu) \end{aligned}\right\} \qquad \text{(D-2)}$$

and thus it can be shown using $C_\alpha = n_\alpha(n_\alpha + 1)$ as in (79) that

$$\left.\begin{aligned} \frac{1}{4\pi}\int_S J(A,\nabla^2 A)Y_\gamma^* \, ds &= i\Sigma\Sigma_{\alpha\beta} A_\alpha A_\beta (C_\beta - C_\alpha) K_{\gamma,\beta,\alpha} \\ \frac{1}{4\pi}\int_S J(A, B)Y_\gamma^* \, ds &= -i\Sigma\Sigma_{\alpha\beta} A_\alpha B_\beta K_{\gamma,\beta,\alpha} \\ \frac{1}{4\pi}\int_S (\nabla \cdot A\nabla B)Y_\gamma^* \, ds &= \Sigma\Sigma_{\alpha\beta} [A_\alpha B_\beta (C_\alpha - C_\beta - C_\gamma) - \\ &\qquad - A_\beta B_\alpha (C_\alpha - C_\beta + C_\gamma)] J_{\gamma,\beta,\alpha} \\ \frac{1}{4\pi}\int_S (A\nabla^2 B)Y_\gamma^* \, ds &= -\Sigma\Sigma_{\alpha\beta} (A_\alpha B_\beta C_\beta + A_\beta B_\alpha C_\alpha) J_{\gamma,\beta,\alpha} \end{aligned}\right\} \qquad \text{(D-3)}$$

where the vector indicies α, β and γ all range over the same values.

A type of linear term, as mentioned above, which requires special attention is that of the form $2\nabla \cdot \mu\nabla A$. For this term we have

$$\frac{1}{4\pi}\int_S (2\nabla \cdot \mu\nabla A)Y_\gamma^* \, ds = C_\gamma (D_\gamma A_{\gamma-1} - E_\gamma A_{\gamma+1}) \qquad \text{(D-4)}$$

where

$$\left.\begin{aligned} D_\gamma &= \frac{2(1 - n_\gamma^2)}{C_\gamma}\left[\frac{(n_\gamma + \ell_\gamma)(n_\gamma - \ell_\gamma)}{(2n_\gamma + 1)(2n_\gamma - 1)}\right]^{\frac{1}{2}} \\ E_\gamma &= \frac{2n_\gamma(n_\gamma + 2)}{C_\gamma}\left[\frac{(n_\gamma + \ell_\gamma + 1)(n_\gamma - \ell_\gamma + 1)}{(2n_\gamma + 1)(2n_\gamma + 3)}\right]^{\frac{1}{2}} \end{aligned}\right\} \quad .(D\text{-}5)$$

With the aid of relationship (D-1), (D-3), (D-4), and (D-5) along with (77), (78), and (79) we can now evaluate all of the terms of the model equations in spectral form. The results of these transformations are shown in Tables D1, D2, and D3. It must be noted here that the integrals embedded within the relationships for $N_\gamma^{(3)}$ and $N_\gamma^{(4)}$ in Table D2 are to evaluated using the transform method as outlined by Machenhauer and Rasmussen (1972).

Table D2. Spectral form of the thermodynamic equations of (74).

Spectral representation	Defining relations
$\frac{1}{4\pi}\int_S \frac{\partial\theta_1}{\partial t} Y_\gamma^* \, ds = \frac{d\theta_\gamma}{dt}$	———
$\frac{1}{4\pi}\int_S \frac{\partial\theta_3}{\partial t} Y_\gamma^* \, ds = \frac{d\theta_\gamma}{dt}$	———
$\frac{1}{4\pi}\int_S (L_3\theta_1) Y_\gamma^* \, ds = L_\gamma^{(3)}\theta_\gamma$	$L_\gamma^{(3)} = (A_1^{LW})_\gamma + (A_1^{SHV})_\gamma - (A_1^{SHH})_\gamma C_\gamma$
$\frac{1}{4\pi}\int_S (L_4\theta_3) Y_\gamma^* \, ds = L_\gamma^{(4)}\theta_\gamma$	$L_\gamma^{(4)} = (B_3^{LW})_\gamma + (B_3^{SHV})_\gamma - (B_3^{SHH})_\gamma C_\gamma$
$\frac{1}{4\pi}\int_S (M_3\theta_3) Y_\gamma^* \, ds = M_\gamma^{(3)}\theta_\gamma$	$M_\gamma^{(3)} = (A_3^{LW})_\gamma + (A_3^{SHV})_\gamma$
$\frac{1}{4\pi}\int_S (M_4\theta_1) Y_\gamma^* \, ds = M_\gamma^{(4)}\theta_\gamma$	$M_\gamma^{(4)} = (B_1^{LW})_\gamma + (B_1^{SHV})_\gamma$
$\frac{1}{4\pi}\int_S [-J(\psi_1,\theta_1)] Y_\gamma^* \, ds = A_\gamma^{(3)}$	$A_\gamma^{(3)} = i\sum_\alpha\sum_\beta \psi_\alpha \theta_\beta K_{\gamma,\beta,\alpha}$
$\frac{1}{4\pi}\int_S [-J(\psi_3,\theta_3)] Y_\gamma^* \, ds = A_\gamma^{(4)}$	$A_\gamma^{(4)} = i\sum_\alpha\sum_\beta \Psi_\alpha \Theta_\beta K_{\gamma,\beta,\alpha}$
$\frac{1}{4\pi}\int_S (\nabla\cdot\theta_1\nabla X_2) Y_\gamma^* \, ds = A_\gamma^{(5)}$	$A_\gamma^{(5)} = \sum_\alpha\sum_\beta [\theta_\alpha X_\beta (C_\alpha - C_\beta - C_\gamma) - \theta_\beta X_\alpha (C_\alpha - C_\beta + C_\gamma)] J_{\gamma,\beta,\alpha}$
$\frac{1}{4\pi}\int_S (-\nabla\cdot\theta_3\nabla X_2) Y_\gamma^* \, ds = A_\gamma^{(6)}$	$A_\gamma^{(6)} = -\sum_\alpha\sum_\beta [\Theta_\alpha X_\beta (C_\alpha - C_\beta - C_\gamma) - \Theta_\beta X_\alpha (C_\alpha - C_\beta + C_\gamma)] J_{\gamma,\beta,\alpha}$

(Table D2 cont.)

Spectral representation	Defining relations
$\frac{1}{4\pi}\int_s (\nabla \cdot \theta_3 \nabla X_4) Y_\gamma^* \, ds = A_\gamma^{(7)}$	$A_\gamma^{(7)} = \sum_{\alpha\beta}\sum [\theta_\alpha X_\beta (C_\alpha - C_\beta - C_\gamma) - \theta_\beta X_\alpha (C_\alpha - C_\beta + C_\gamma)] J_{\gamma,\beta,\alpha}$
$\frac{1}{4\pi}\int_s A_s J(\psi_3, h_s) Y_\gamma^* \, ds = A_\gamma^{(8)}$	$A_\gamma^{(8)} = -iA_s \sum_{\alpha\beta}\sum \Psi_\alpha h_\beta K_{\gamma,\beta,\alpha}$
$\frac{1}{4\pi}\int_s (\theta_2 \nabla^2 X_2) \, Y_\gamma^* \, ds = A_\gamma^{(9)}$	$A_\gamma^{(9)} = -\sum_{\alpha\beta}\sum (\bar{\theta}_\alpha X_\beta C_\beta + \bar{\theta}_\beta X_\alpha C_\alpha) J_{\gamma,\beta,\alpha}$
$\frac{1}{4\pi}\int_s N_3(\theta_4, X_2) Y_\gamma^* \, ds = N_\gamma^{(3)}$	$N_\gamma^{(3)} = (\dot{Q}_1^{SW})_\gamma + (A_0^{LW})_\gamma + \sum_{\alpha\beta}\sum (A_4^{LW})_\alpha T_\beta J_{\gamma,\beta,\alpha} - \frac{3}{2}\varepsilon L_{\ell v} \times \left(\frac{p_1}{p_4}\right)^2 \frac{1}{4\pi}\int_s q_4 f(\nabla^2 X_2) Y_\gamma^* \, ds$
$\frac{1}{4\pi}\int_s N_4(\theta_4, X_2, X_4) Y_\gamma^* \, ds = N_\gamma^{(4)}$	$N_\gamma^{(4)} = (\dot{Q}_3^{SW})_\gamma + (B_0^{LW})_\gamma + \sum_{\alpha\beta}\sum [(B_4^{LW})_\alpha + (B_4^{SHV})_\alpha] T_\beta J_{\gamma,\beta,\alpha} - \frac{3}{2}\varepsilon L_{\ell v} \times \left(\frac{p_3}{p_4}\right)^2 \frac{1}{4\pi}\int_s q_4 f(\nabla^2 X_4 + \nabla^2 X_2) \times Y_\gamma^* \, ds$

Table D3. Spectral form of the diagnostic relationships, (76).

Spectral representation	Defining relations
$-\frac{1}{4\pi C_\gamma}\int_s (B\nabla^2\theta_2)\, Y_\gamma^*\, ds = B\bar{\theta}_\gamma$	see Eq. (C-5)
$-\frac{1}{4\pi C_\gamma}\int_s [-2\nabla\cdot\mu\nabla(\psi_1 - \psi_3)]Y_\gamma^*\, ds =$	
$= D_\gamma(\psi_{\gamma-1} - \Psi_{\gamma-1}) - E_\gamma(\psi_{\gamma+1} -$	
$- \Psi_{\gamma+1})$	see Eq. (D-5)
$-\frac{1}{4\pi C_\gamma}\int_s (\nabla^2 X_4)\, Y_\gamma^*\, ds = \chi_\gamma$	———
$-\frac{1}{4\pi C_\gamma}\int_s [-B_s J(\psi_3, h_s)]Y_\gamma^*\, ds =$	
$\frac{B_s}{A_s} C_\gamma A_\gamma^{(8)}$	see Table D2
$\frac{1}{4\pi}\int_s F_4^{SH}\theta_4 Y_\gamma^*\, ds = F_4^{SH} T_\gamma$	see Eq. (60)
$\frac{1}{4\pi}\int_s F_4^{LWC}\theta_4 Y_\gamma^*\, ds = F_4^{LWC} T_\gamma$	see Eqs. (B-14) and (B-17)
$\frac{1}{4\pi}\int_s F_4^{LWW}\theta_4 Y_\gamma^*\, ds = W_\gamma^{(1)}(\theta_4)$	$W_\gamma^{(1)}(\theta_4) = \sum\sum_{\alpha\beta}(F_4^{LWW})_\alpha T_\beta J_{\gamma,\beta,\alpha}$ [see Eqs. (B-14) and (B-17)]

(Table D3 cont.)

Spectral representation	Defining relations
$\frac{1}{4\pi}\int_S (F_0^{LW} - F_A^{SW})\, Y_\gamma^*\, ds = (F_0^{LW})_\gamma -$	
$- (F_A^{SW})_\gamma$	see Eqs. (B-14), (32), and (33)
$\frac{1}{4\pi}\int_S F_1^{LW}\theta_1\, Y_\gamma^*\, ds = W_\gamma^{(2)}$	$W_\gamma^{(2)} = \sum_\alpha\sum_\beta (F_1^{LW})_\alpha \theta_\beta J_{\gamma,\beta,\alpha}$
$\frac{1}{4\pi}\int_S F_3^{LW}\theta_3\, Y_\gamma^*\, ds = W_\gamma^{(3)}$	$W_\gamma^{(3)} = \sum_\alpha\sum_\beta (F_3^{LW})_\alpha \theta_\beta J_{\gamma,\beta,\alpha}$
$\frac{1}{4\pi}\int_S F_3^{SH}\theta_3\, Y_\gamma^*\, ds = F_3^{SH}\theta_\gamma$	see Eq. (60)

APPENDIX E

DEVELOPMENT AND NUMERICAL SOLUTION OF THE X EQUATION

The centered difference form of the time differentiated thermal wind relationship (89) can be written as

$$\frac{B}{2}\left[\overline{\theta}_\gamma(t+\Delta t) - \overline{\theta}_\gamma(t-\Delta t)\right] = D_\gamma\left[\tau_{\gamma-1}^{(t+\Delta t)} - \tau_{\gamma-1}^{(t-\Delta t)}\right] - E_\gamma\left[\tau_{\gamma+1}^{(t+\Delta t)} - \tau_{\gamma+1}^{(t-\Delta t)}\right] . \quad \text{(E-1)}$$

Substitution from (88) along with a rearrangement of terms allows us to convert (E-1) to the form

$$f_\gamma^{(1)} X_{\gamma-2} + f_\gamma^{(2)'} X_\gamma + f_\gamma^{(3)} X_{\gamma+2} + g'_\gamma(X) = R_\gamma \quad \text{(E-2)}$$

where we have defined

$$\left.\begin{aligned}
f_\gamma^{(1)} &\equiv 2\Delta t\ e^{P_{\gamma-1}^{(S)}\Delta t}\ D_\gamma D_{\gamma-1} \\
f_\gamma^{(2)'} &\equiv -2\Delta t\left(e^{P_{\gamma-1}^{(S)}\Delta t}\ D_\gamma E_{\gamma-1} + e^{P_{\gamma+1}^{(S)}\Delta t}\ E_\gamma D_{\gamma+1}\right) \\
f_\gamma^{(3)} &\equiv 2\Delta t\ e^{P_{\gamma+1}^{(S)}\Delta t}\ E_\gamma E_{\gamma+1} \\
g'(X) &\equiv B\Delta t\ e^{H_\gamma^{(M)}\Delta t}\ G_\gamma(X) \\
R_\gamma &\equiv D_\gamma\left[\left(e^{2P_{\gamma-1}^{(S)}\Delta t} - 1\right)\tau_{\gamma-1}^{(t-\Delta t)} + 2\Delta t\ e^{P_{\gamma-1}^{(S)}\Delta t}\ N_{\gamma-1}^{(S)}\right] - \\
&\quad -E_\gamma\left[\left(e^{2P_{\gamma+1}^{(S)}\Delta t} - 1\right)\tau_{\gamma+1}^{(t-\Delta t)} + 2\Delta t\ e^{P_{\gamma+1}^{(S)}\Delta t}\ N_{\gamma+1}^{(S)}\right] - \\
&\quad -\frac{B}{2}\left[\left(e^{2H_\gamma^{(M)}\Delta t} - 1\right)\overline{\theta}_\gamma(t-\Delta t) + 2\Delta t\ e^{H_\gamma^{(M)}\Delta t}\ S_\gamma^{(M)}\right]
\end{aligned}\right\} . \quad \text{(E-3)}$$

According to the model truncation as outlined in the main text and drawn schematically in Fig. 3 we must consider (E-2) over the set of

vector indices for $|\ell_{max}| \leq 16$ and $N \leq 8$. Thus, from (83) we see that there will be a total of eight real (zonal, $\ell_\gamma = 0$) and 128 complex vectors (conjugates are completely specified in terms of the complex values). This means of course, that (E-2) represents a set of 264 real equations with 264 unknown quantities. In matrix notation we can write (E-2) in the form

$$(F' + G')X = R \tag{E-4}$$

where we see that F' is tridiagonal (all elements except those along the three main diagonals are zero) of order 264. G' is of order 264 × 264 while X and R are column matrices with length 264.

We seek a solution for X in (E-4) for each time step in our numerical integration. However, in order to speed up this calculation we wish to avoid the large 264 × 264 matrix inversion that would normally be indicated. Instead, we propose to make use of certain physical and mathematical properties known to exist within F' and G' to simplify our calculation. In order to do this we first must investigate the detailed form of G' . Using definitions (E-3), (86), and (D-3) along with Table D2 we can write for the element $g'_\gamma(X)$ of G'

$$\begin{aligned} g'_\gamma(X) &= \frac{B\Delta t e^{H_\gamma^{(M)}\Delta t}}{2} \sum_\alpha\sum_\beta [(\theta_\alpha - \Theta_\alpha)X_\beta(C_\alpha - C_\beta - C_\gamma) - \\ &\quad - (\theta_\beta - \Theta_\beta)X_\alpha(C_\alpha - C_\beta + C_\gamma)]J_{\gamma,\beta,\alpha} \\ &= B\Delta t e^{H_\gamma^{(M)}\Delta t} [\sum_\alpha\sum_\beta \sigma_\alpha X_\beta(C_\alpha - C_\beta - C_\gamma)J_{\gamma,\beta,\alpha} - \\ &\quad - \sum_\alpha\sum_\beta \sigma_\beta X_\alpha(C_\alpha - C_\beta + C_\gamma)J_{\gamma,\beta,\alpha}] \end{aligned} \tag{E-5}$$

where now the indices α , β , and γ range only over the vector indices as contained within the truncation limits outlined above except that we need not concern ourselves with the set of conjugate vectors, γ^*. We see through use of (84) in (E-5) that each element $g'_\gamma(X)$ is not only a function of the vertically integrated velocity potential X but also dependent upon the shear temperature (static stability) represented by σ . Because the large scale mean stability in the atmosphere dominates large scale perturbation quantities we can make use of this physical property to simplify (E-4). Further, it can be shown that the terms in $g'_\gamma(X)$ involving the mean stability are of the same order of magnitude as the tridiagnonal factors $f_\gamma^{(1)}$, $f_\gamma^{(2)'}$, and $f_\gamma^{(3)}$.

In order to take advantage of this property we will evaluate (E-5) in terms of the global mean shear temperature σ_o^o (i.e., $\sigma_\alpha = \sigma_\beta = \sigma_{o+io}$) which then can be shown to take on the values

$$g'_\gamma(\sigma_o^o, X) = -2\Delta t e^{H_\gamma^{(M)}\Delta t} C_\gamma \sigma_o^o X_\gamma \quad . \tag{E-6}$$

Clearly (E-6) shows that all the elements of (E-5) in G' involving the mean stability of the atmosphere lie along the main diagonal and thus we will include these elements with $f_\gamma^{(2)'}$ such that we can now write the matrix equation (E-4) as

$$FX = R - GX \tag{E-7}$$

or in index form following (E-2)

$$f_\gamma^{(1)} X_{\gamma-2} + f_\gamma^{(2)} X_\gamma + f_\gamma^{(3)} X_{\gamma+2} = R_\gamma - g_\gamma(X) \tag{E-8}$$

where now

$$\left.\begin{aligned} f_\gamma^{(2)} &= f_\gamma^{(2)'} - 2\Delta t e^{H_\gamma^{(M)}\Delta t} C_\gamma \sigma_o^o X_\gamma \\ g_\gamma(X) &= g'_\gamma(X) + 2\Delta t e^{H_\gamma^{(M)}\Delta t} C_\gamma \sigma_o^o X_\gamma \end{aligned}\right\} \quad . \tag{E-9}$$

From (E-8) we see that F is tridiagonal and GX is a column matrix containing elements of comparitively small magnitudes. We will consider GX as a small correction term and solve the system (E-7) as tridiagonal using a succession of iterations until an adequate convergence is obtained.

Close scrutiny into the details of (E-7) shows that except for the correction term GX the matrix equations can be uncoupled between the planetary waves ℓ_γ ($\gamma = n_\alpha + i\ell_\gamma$). Thus, we can solve the tridiagonal system separately for each planetary wave which results in one matrix set of order eight (for the zonal equations) and sixteen sets of order sixteen. However, there exists a very simple algorithm for solving these equations (for example, see Young, 1962) involving only a small fraction of the number of arithmetic operations required with a general matrix. This represents a significant savings in computational time.

The general computational procedure is to obtain a reasonable "first guess" X matrix (we will use zero for the initial field at the beginning of the model time integration and subsequently the X field obtained during the previous time step) and then R - GX is evaluated from known quantities. The tridiagonal algorithm is then applied to obtain a partial solution, X' , for the X field. However, in order to insure as rapid a convergence as possible an overrelaxation procedure is introduced where we adjust the X' values. Using the n^{th} iteration as an example, $X^{(n)}$ is estimated from

$$X^{(n)} = X^{(n-1)} + \Lambda \left(X^{(n)'} - X^{(n-1)}\right) \qquad \text{(E-10)}$$

where the overrelaxation constant Λ is determined through a numerical testing process. This entire procedure is then repeated until a satisfactory convergence for the X matrix is attained. We have found that using the value $\Lambda = 1.4$ each element in X will converge to at least four significant figures within three of four iterations.